NUREG/CR-3689 Vol. II
ANL-83-85 Vol. II

NUREG/CR-3689 Vol. II
ANL-83-85 Vol. II

MATERIALS SCIENCE AND TECHNOLOGY DIVISION LIGHT-WATER-REACTOR SAFETY RESEARCH PROGRAM: QUARTERLY PROGRESS REPORT

April – June 1983

ARGONNE NATIONAL LABORATORY, ARGONNE, ILLINOIS
Operated by THE UNIVERSITY OF CHICAGO

Prepared for the Office of Nuclear Regulatory Research
U. S. NUCLEAR REGULATORY COMMISSION
under Interagency Agreement DOE 40-550-75

Available from

GPO Sales Program
Division of Technical Information and Document Control
U. S. Nuclear Regulatory Commission
Washington, D.C. 20555

and

National Technical Information Service
Springfield, Virginia 22161

NUREG/CR-3689 Vol. II
ANL-83-85 Vol. II

(Distribution Codes:
R3 and R5)

ARGONNE NATIONAL LABORATORY
9700 South Cass Avenue
Argonne, Illinois 60439

MATERIALS SCIENCE AND TECHNOLOGY DIVISION LIGHT-WATER-REACTOR SAFETY RESEARCH PROGRAM: QUARTERLY PROGRESS REPORT April—June 1983

Date Published: June 1984

Previous reports in this series

ANL-82-41 Vol. I	January—March 1982
ANL-82-41 Vol. II	April—June 1982
ANL-82-41 Vol. III	July—September 1982
ANL-82-41 Vol. IV	October—December 1982
ANL-83-85 Vol. I	January—March 1983

Prepared for the Division of Engineering Technology
Office of Nuclear Regulatory Research
U. S. Nuclear Regulatory Commission
Washington, D. C. 20555
Under Interagency Agreement DOE 40-550-75

NRC FIN Nos. A2016, A2017, A2212, A2243

MATERIALS SCIENCE AND TECHNOLOGY DIVISION
LIGHT-WATER-REACTOR SAFETY
RESEARCH PROGRAM:
QUARTERLY PROGRESS REPORT

April-June 1983

ABSTRACT

This progress report summarizes the Argonne National Laboratory work performed during April, May, and June 1983 on water reactor safety problems. The research and development areas covered are Environmentally Assisted Cracking in Light Water Reactors, Transient Fuel Response and Fission Product Release, Clad Properties for Code Verification, and Long-Term Embrittlement of Cast Duplex Stainless Steels in LWR Systems.

NRC Fin No.	FIN Title
A2016	Transient Fuel Response and Fission Product Release
A2017	Clad Properties for Code Verification
A2212	Environmentally Assisted Cracking in Light Water Reactors
A2243	Long-Term Embrittlement of Cast Duplex Stainless Steels in LWR Systems

TABLE OF CONTENTS

TABLE OF CONTENTS (Contd.)

MATERIALS SCIENCE AND TECHNOLOGY DIVISION
LIGHT-WATER-REACTOR SAFETY
RESEARCH PROGRAM:
QUARTERLY PROGRESS REPORT

April-June 1983

EXECUTIVE SUMMARY

I. ENVIRONMENTALLY ASSISTED CRACKING IN LIGHT-WATER REACTORS[a]

Acoustic background data have been acquired during hot functional testing at the Watts Bar reactor in Tennessee. These data, along with other measurements at the Hatch-1 reactor, information obtained from the literature, and measurements on leaks through IGSCC, permit estimates of the sensitivity of acoustic leak detection systems in the field. The results suggest that at a distance of 3 m, leaks as small as 38 cm^3/min (0.01 gal/min) may be detectable in areas of low background noise, whereas only leaks on the order of 7600 cm^3/min (2 gal/min) may be detectable in areas of very high background noise, e.g., near the reactor pumps.

Two types of specimens are being used to investigate the effect of plastic strain on the subsequent sensitization behavior of Type 304 stainless steel: (1) laboratory specimens with controlled plastic strains produced by tensile loading and (2) specimens from weldments that have received mitigation treatments such as IHSI (induction heating stress improvement), HSW (heat sink welding), and LPHSW (last pass heat sink welding). The specimens deformed by tensile loading showed more sensitization than the undeformed specimens even after short-term, relatively high-temperature aging treatments. More significant differences are expected to occur during aging at lower temperatures.

Crack growth rate data are currently available for only a limited range of loading histories. Tests are in progress to extend the data to a wider

[a]RSR FIN Budget No. A2212; RSR Contact: J. Muscara.

range of loading ratios and frequencies. In addition, these tests are being used to assess the applicability of estimates of crack-tip strain rates obtained by use of linear elastic fracture mechanics. The tests indicate that small load variations have a relatively small effect on the crack growth rate. However, the current crack tip estimates do not correlate the data well, and more analytical work is needed to obtain adequate estimates.

TGSCC was observed in Type 316NG stainless steel in slow-strain-rate tests in an impurity environment containing 0.1 ppm sulfate, which is within the BWR water chemistry guidelines suggested by Reg. Guide 1.56. Sensitized stainless steels in this environment crack intergranularly; the transgranular crack growth rates in the Nuclear Grade material are significantly lower than the intergranular growth rates in the sensitized material. The cracks appear to initiate at fairly low plastic strains, so that they cannot simply be dismissed as an artifact of the slow-strain-rate test. However, additional work is needed to better identify the level of plastic strain required to produce cracking.

Additional information has been obtained on the interaction of dissolved oxygen, hydrogen, and sulfate (as sulfuric acid) on the SCC susceptibility of sensitized Type 304 stainless steel from slow-strain-rate tests in 289°C water. At high sulfate levels (10 ppm), intergranular cracking was observed even at very low oxygen levels (<5 ppb). Similarly, at high dissolved-oxygen levels (0.2 ppm), cracking occurs even in very high-purity water. However, for impurity levels consistent with the Reg. Guide 1.56 limits, lowering the dissolved oxygen levels does reduce susceptibility to IGSCC, and the results suggest that hydrogen additions would reduce susceptibility even if no other improvements in water chemistry were undertaken.

II. TRANSIENT FUEL RESPONSE AND FISSION PRODUCT RELEASE[b]

Rates of release of fission gas and volatile fission products from LWR fuel rods have been analyzed in order to compare the results presented in NUREG-0772 with the FASTGRASS code predictions. A series of experiments with highly irradiated fuel conducted in steam as well as dry air in the temperature range of 500 to 1600°C provided the data base for fission product release.

Xenon and iodine release rates predicted with FASTGRASS for HBU-, HT-, and HI- series tests are in good agreement with the NUREG-0772 curve. Release rates for noble gases and iodine are practically the same.

Cesium release rates, as predicted by FASTGRASS, tend to be higher than those reported in NUREG-0772 and thus are much higher than release rates for xenon and iodine. The diffusion coefficient used for cesium in FASTGRASS is several orders of magnitude higher than the diffusion coefficient for xenon. Thus, the rate at which cesium is predicted to be released from the fuel is higher than for iodine and xenon. The diffusion coefficient for cesium is based on the experimental results of Oi and Takagi. If it is assumed that atomic cesium diffuses at about the same rate as xenon and iodine, the FASTGRASS-predicted release rate constants for cesium will be in reasonable agreement (i.e., similar to the xenon and iodine results) with the NUREG-0772 results. (At temperatures greater than ~1200 K, the NUREG-0772 curves for iodine, xenon, and cesium release rate constants are identical.)

[b]RSR FIN Budget No. A2016; RSR Contact: G.P. Marino.

III. CLAD PROPERTIES FOR CODE VERIFICATION[c]

Zircaloy fuel cladding is susceptible to local breach-type failures during power transients in LWRs because of stresses imposed by differential thermal expansion of the fuel and cladding. In this program, the effect of stress state, strain rate, and temperature on the deformation characteristics of irradiated Zircaloy fuel cladding is being investigated to provide mechanical-property information and a failure criterion for the cladding under loading conditions conducive to pellet-cladding interaction (PCI). The information will be used in the development of codes to analyze PCI in fuel rods from power ramp experiments in test reactors, and to evaluate the susceptibility of extended-burnup fuel elements and new fuel element designs in commercial reactors to PCI failures during power transients.

SEM examination of the fracture surface morphologies of the irradiated Big Rock Point (BWR) and H. B. Robinson (PWR) fuel cladding was completed in the previous reporting period. Several fractures in high-burnup H. B. Robinson fuel cladding tubes, produced at 292-325°C by the expanding-mandrel technique, were examined by SEM and optical microscopy during the current reporting period. A ductile fracture produced at 292°C and a brittle-type fracture produced at 325°C were identified. The brittle-type fracture was characterized by "x-marks" at the outer surface, numerous small cracks at the inner surface, negligible wall thinning in the fracture region, and pseudocleavage at the fracture surfaces. All the through-wall cracks produced in the expanding-mandrel tests were found to have initiated at the inner surface and propagated toward the outer surface.

Continued efforts in the TEM-HVEM examination of the brittle-type PCI-like failure produced in Big Rock Point fuel cladding by internal gas pressurization at 325°C resulted in a direct observation of individual dislocations decorated by Zr_3O precipitates. This provides further evidence that brittle-type failures are associated with segregation of oxygen (present in the cladding material either as an alloying element or as a by-product of in-reactor corrosion) to dislocations and radiation-induced defects, which

---

[c]RSR FIN Budget No. A2017; RSR Contact: H. H. Scott.

leads to the formation of a Zr_3O phase, an immobilization of dislocations, and eventually to a minimal plastic deformation in the material.

Also described are additional results from gas pressurization and mandrel-loading experiments performed at 325°C on segments of Maine Yankee and H. B. Robinson Zircaloy-4 fuel cladding.

IV. LONG-TERM EMBRITTLEMENT OF CAST DUPLEX STAINLESS STEELS IN LWR SYSTEMS[d]

Investigations of the aging behavior of cast duplex stainless steels show substantial reductions in room-temperature impact strength after 10,000 to 70,000 h of exposure to temperatures as low as 300°C. Data on J_{IC} fracture toughness also indicate significant reduction of impact strength as a result of low-temperature aging, although the results do not always show good correlations with trends indicated by the Charpy data. At temperatures below 500°C, embrittlement of the duplex stainless steels has been attributed to the precipitation of the α' phase in the ferrite matrix. The kinetics of embrittlement are expressed by an Arrhenius relation and the activation energy is determined by examining the degree of embrittlement produced by different time/temperature histories. A satisfactory understanding of the aging process is required to ensure that the activation energy obtained from the laboratory tests is representative of the actual process so that valid predictions of long-term embrittlement at reactor operating temperatures can be made. The available information on the microstructure of aged cast stainless steels is not sufficient for correlating the microstructure with the mechanical properties or for determining the mechanism of low-temperature embrittlement.

A program was initiated to (1) characterize and correlate the microstructure of aged material with loss of fracture toughness, (2) determine the validity of laboratory-induced embrittlement data for predicting the toughness at reactor operating temperatures, (3) characterize the loss of toughness in terms of fracture mechanics parameters, and (4) provide additional data on the effects of compositional and metallurgical variables on the kinetics and degree of embrittlement.

---

[d]RSR FIN Budget No. A2243; RSR Contact: J. Muscara.

Various experimental and commercial heats of ASTM A351 and A451 grades of CF-8, CF-8M, and CF-3 cast stainless steel were procured in different product forms and section thicknesses. Charpy-impact and 1-T compact-tension specimen blanks have been obtained from the various cast materials. The specimen blanks will be aged at 450, 400, 350, 320, and 290°C for various lengths of time. The cast material is being characterized to determine the chemical composition, ferrite content, hardness, and grain structure.

The initial experimental effort is focused on microstructural evaluation of aged specimens of CF-8 and CF-8M cast stainless steels. Aging of the cast material for 1000 h at 475°C produced the mottled structure of α' and a FCC phase similar to $M_{23}C_6$. Examination of CF-8 cast stainless steel that was aged for 70,000 h at 400°C did not reveal the mottled images of the α' precipitate. Instead, the $M_{23}C_6$-like precipitate was present both on and away from dislocations. Another type of precipitate was observed in the material after aging for 10,000 h at 400°C.

I. ENVIRONMENTALLY ASSISTED CRACKING IN LIGHT WATER REACTORS

Principal Investigators:
W. J. Shack, T. F. Kassner, D. S. Kupperman, T. N. Claytor,
J. Y. Park, P. S. Maiya, W. E. Ruther,
and F. A. Nichols

The objective of this program is to develop an independent capability for prediction, detection, and control of intergranular stress corrosion cracking (IGSCC) in light-water reactor (LWR) systems. The program is primarily directed at IGSCC problems in existing plants, but also includes the development of recommendations for plants under construction and future plants. The scope includes the following: (1) development of the means to evaluate acoustic leak detection systems objectively and quantitatively; (2) evaluation of the influence of metallurgical variables, stress, and the environment on IGSCC susceptibility, including the influence of plant operations on these variables; and (3) examination of practical limits for these variables to effectively control IGSCC in LWR systems. The initial experimental work concentrates primarily on problems related to pipe cracking in LWR systems. However, ongoing research work on other environmentally assisted cracking problems involving pressure vessels, nozzles, and turbines will be monitored and assessed, and where unanswered technical questions are identified, experimental programs to obtain the necessary information will be developed to the extent that available resources permit.

The effort is divided into six subtasks: (A) Leak Detection and Nondestructive Evaluation; (B) Analysis of Sensitization; (C) Crack Growth Rate Studies; (D) Evaluation of Nonenvironmental Corrective Actions; (E) Evaluation of Environmental Corrective Actions; and (F) Mechanistic Studies. These subtasks reflect major technical concerns associated with IGSCC in LWR systems, namely: leak and crack detection, the role of materials susceptibility, the role of stress in crack initiation and propagation, and the role of the environment. The program seeks to evaluate potential solutions to IGSCC problems in LWRs, both by direct experimentation (including full-scale welded pipe tests) and through the development of a better basic understanding of the various phenomena.

A. Leak Detection and Nondestructive Evaluation (D. S. Kupperman, T. N. Claytor, and R. N. Lanham)

1. Introduction

a. Leak Detection

Early detection of leaks in nuclear reactors is necessary in order to identify deteriorating or failed components and minimize the release of radioactive materials. Before a nuclear power facility can be placed into operation, the NRC requires that operational leak-detection systems of various kinds be installed. Some allowance is made for leakage from packing, shaft seals, etc., and the flow from these "identified leaks" is monitored during plant operation. Thus, even with the system operating normally, there may be some accumulation of water in the sumps, with a concomitant increase in the level of radioactivity. However, the levels of radioactivity and leakage are expected to be reasonably constant with time.

No currently available single leak-detection method combines optimal leakage detection sensitivity, leak-locating ability, and leakage measurement accuracy. For example, although quantitative leakage determination is possible with condensate flow monitors, sump monitors, and primary coolant inventory balance, these methods are not adequate for locating leaks and are not necessarily sensitive enough to meet code requirements. Acoustic methods represent the most promising area for improvement in leak detection. They have the best chance of success when specific welds are monitored, and the least when a few probes are used to monitor many welds. However, the ability to locate leaks and quantify leak rates by use of acoustic techniques is not well established, especially since virtually no data are available on acoustic signals from field-induced IGSCC.

b. Nondestructive Evaluation

For safety-related as well as practical reasons, it is desirable to detect any cracks in the primary and secondary coolant boundaries of LWRs even before leakage occurs, and to fix them within a reasonable length of time. This is in accord with the NRC "defense-in-depth" philosophy, which requires the consideration of all possible efforts that might prevent a nuclear accident. In recent years, numerous cracks have been discovered in coolant systems of LWRs. Although the main problems have been in BWR primary coolant lines, cracking has occurred in PWR feedwater piping and low-temperature, low-pressure lines near the spent-fuel storage pool. Unfortunately, many of these cracks were missed during ultrasonic in-service inspection (ISI) and detected only because of leakage, and this has created doubts concerning the capability of ultrasonic ISI to detect cracks. The present ultrasonic testing procedures for ferritic weldments (ASME Code Sections V and XI) do not appear to be adequate for the detection and evaluation of IGSCC in austenitic stainless steel (SS) piping. Indeed, the detection of IGSCC before the cracks have grown large enough to cause a leak, and the detection, location, and sizing of leaks once they occur, are very difficult technical goals to achieve. IGSCC that can be detected by conventional ultrasonic testing under laboratory conditions may be missed during a field examination by even the most skillful operator.

c. Objectives

The objectives of this subtask are to (1) develop an independent capability to assess the effectiveness of current and proposed techniques for acoustic leak detection (ALD) in reactor coolant systems, (2) develop a strategy for hardware realization, and (3) examine potential improvements in ultrasonic methods for detection of IGSCC and inspection of cast SS. The program will establish whether meaningful quantitative data on leak rates and locations can be obtained from acoustic signatures of leaks due to cracks (IGSCC and fatigue) in low- and high-pressure lines, and whether these can be distinguished from other types of leaks. It will also establish calibration procedures for acoustic data acquisition and show whether advanced signal processing can be employed to enhance the adequacy of ALD schemes.

2. Technical Progress

a. Leak Detection

(1) Effect of System Pressure

In the previous report,[1] the acoustic output from IGSCC #1 was determined as a function of crack opening. During the current reporting period, IGSCC #1 was pressure tested to determine the effect on acoustic output of an increased leak rate through the crack opening without a change in crack geometry. (It should be noted that since the temperature remains constant as the pressure increases, the quality of the fluid changes, and this may complicate the interpretation of the results.) The results of the pressure test (6.8-12.6 MPa or 992-1830 psi) at a constant temperature (257°C or 494°F) and load (0 psi) are shown in Fig. 1.1. At 300-400 kHz, the

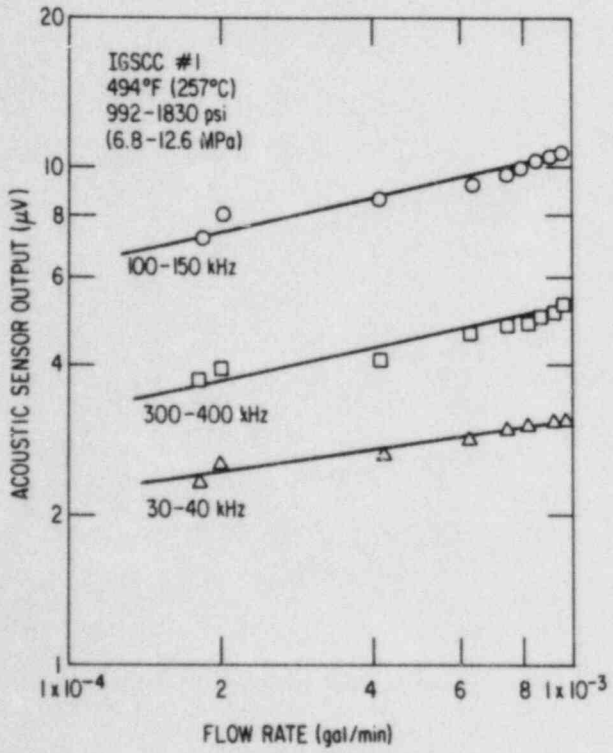

Fig. 1.1

Acoustic Sensor Output vs Leak Rate, Where Leak Rate is Increased by Increasing the System Pressure Over the Range from 6.8 to 12.6 MPa. Conversion factor: 1 gal = 3800 cm^3.

acoustic signal V_m shows the following leak rate dependence:

$$V_m = 22.4\ F^{0.21} \qquad (1 \times 10^{-4} < F < 1 \times 10^{-3}\ \text{gal/min}),$$

where V_m is in μV. This dependence is different from that obtained when the leak rate was varied by stressing the crack to open it.[1] This result (combined with other data from Refs. 1-3) indicates that acoustic output is a relatively weak function of leak rate and is influenced to some degree by crack geometry.

(2) Acoustic Background Data from Watts Bar

Acoustic background data have been acquired (with the cooperation of Battelle Pacific Northwest Laboratory) during a hot functional test of the TVA's Watts Bar Nuclear Reactor in Tennessee. An acoustic emission transducer (AET 375 S/N 6002) was mounted on the accumulator safety injection pipe (on the cold leg of loop 2) of the Watts Bar-1 reactor. The transducer was attached to the uninsulated 10-in. stainless steel pipe with a 25.4-cm (10-in.)-long waveguide-probe assembly. An acoustic emission preamp with a gain of 40 dB was used to amplify the signal from the transducer and drive a 50-Ω cable. The cable terminated in the control room where another amplifier and other signal-recording equipment were located. Prior to the installation of the transducer at Watts Bar, the transducer-waveguide assembly was calibrated in the laboratory against a standard broadband transducer (NBS IQI 501). Results at five frequencies are shown in Table 1.1.

TABLE 1.1. Comparison of Acoustic Output from NBS and AET 375 Transducers

Frequency, kHz	Output, dB		Difference, dB
	NBS	AET 375	
90	-131.0	-144.0	- 6.0
150	-142.5	-159.0	-16.5
255	-151.0	-160.5	- 9.5
320	-152.5	-160.0	- 7.5
375	-154.5	-154.0	+ 0.5

The most important result from this calibration was that at 375 kHz, the NBS transducer and the AET 375 have almost the same sensitivity. This is useful because it implies that there is a simple relationship between the noise signals measured in the lab with the NBS transducer and those measured at Watts Bar with the AET 375 transducer. After the transducer was installed at Watts Bar, its sensitivity was tested by the pencil lead breaking technique [see subsection (3) below]. The resultant signal was 1.4 dB greater than that produced by the NBS transducer in an identical test in the laboratory.

Background noise was monitored at Watts Bar-1 before, during, and after a hot flow test. Before and after the test, the water temperature and pressure were near ambient conditions (24-35°C or 75-95°F; 2-5 x 10^5 Pa or 30-75 psi); during the hot flow test, the water temperature and pressure reached reactor operating conditions (292°C or 557°F; 15.4 MPa or 2235 psi). In general, the reactor noise level was greatest with all four reactor coolant pumps on and with the water at low temperature and pressure. Table 1.2 summarizes the noise levels measured at 200-400 kHz (primarily near 375 kHz) for various reactor conditions; the data show that in general, the noise background decreased with increasing system pressure. This has also been observed in other tests of reactor background noise.[4] The decrease in noise at higher pressure is probably related to decreased cavitation in the pumps. Still, the noise at full operating power was 28 dB above that measured in the quiescent state. Since the transducer was very close to the pump, the values for noise background reported here are near the maximum values that will be found on the primary piping. This is also a much higher noise level than that measured at the Georgia Power Company's Hatch-1 reactor.[1]

(3) Calibration Procedures

Three calibration procedures are being considered for checking transducer-waveguide systems after field installation. Two of these, the pencil lead breaking and gas jet techniques, were examined during the current reporting period. The third technique, electronic pulsing, will be examined later.

TABLE 1.2. Acoustic Noise Level (Transducer Output) in the 200-400 kHz Frequency Band

Reactor Pump Status	Water Temperature, °C (°F)	Water Pressure, 10^5 Pa (psi)	Transducer Output, μV	Comments
All pumps off	23 (75)	1.4 (20)	3.4	After installation
All pumps off	43 (110)	20.1 (300)	2.8	After installation
RCP-2 on	43 (110)	20.1 (300)	620	During hot flow test
All pumps on	177 (350)	27.6 (400)	390	During hot flow test
All pumps on	232 (450)	82.7 (1200)	83	During hot flow test
All pumps on	292 (558)	154.0 (2235)	92	During hot flow test
All pumps off	34 (95)	5.1 (74)	38	After hot flow test
All pumps off	34 (94)	2.0 (29)	32	After hot flow test

A Pentel mechanical pencil with a 0.5-mm-diam lead was used to test the lead br g technique. The procedure consists of extending the lead 5 mm beyond the end of the pencil body and pressing it against the pipe at an angle of 30° to the pipe until it breaks. (If this technique is demonstrated to be useful, fixtures will be fabricated to standardize the procedure.) An AET 375 transducer on a waveguide was used to detect the lead breaking at a distance of 20 cm. The excellent reproducibility of the captured acoustic transient signal is evident from Fig. 1.2, which shows the digitized and stored transient pulses from 4 successive breaks. This technique may be useful as a convenient, rapid check of ALD systems after installation. The method would not be applicable, however, for remote in-situ calibration; the gas jet technique or electronic pulsing would be suitable for the latter purpose.

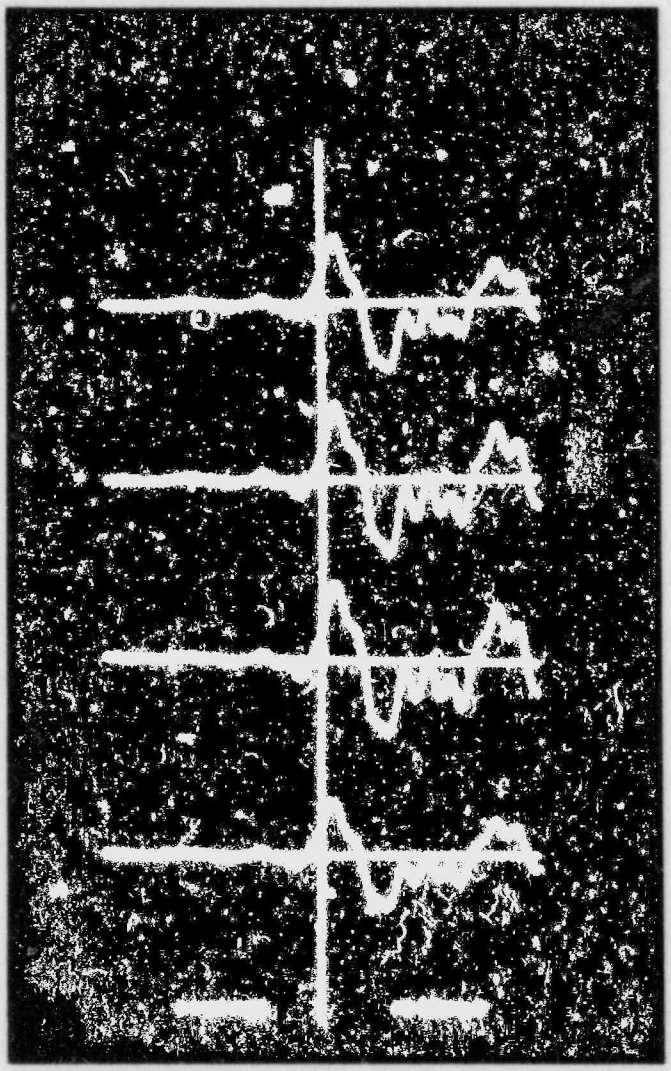

Fig. 1.2

Transients from 4 Successive Pencil Lead Breaking Tests, with Lead Broken Against 10-in. Schedule 80 Piping at a Point 20 cm Away from AET 375 Transducer with Waveguide. Sample rate is 50 ns; width of entire trace is 50 μs.

For evaluation of the gas jet technique, a Swagelok fitting with a 1.5-mm-diam exit hole was used to direct a stream of nitrogen gas normal to the pipe surface from a distance of 6 mm. An rms signal (50 kHz to 1 MHz) 4 times greater than the electronic background noise was detected at 1 m from the source. In this case, the NBS broadband transducer was used to obtain frequency spectrum information. The acoustic spectrum from the gas jet shows greater frequency dependence, with relatively more signal at lower frequencies, than the spectrum from an IGSCC leak. Furthermore, most of the detected acoustic signal from the gas jet is in the form of surface waves; this is not the case for IGSCC leaks. It has also been determined that the acoustic signal is relatively insensitive to the position of the nozzle if

the end of the nozzle is held about 1 cm from the pipe surface. This calibration technique has the advantage of providing a reproducible, continuous acoustic signal somewhat representative of an actual leak; in principle, it could be used for remote calibration. The disadvantages are the inconvenience associated with setting up the system and the problems associated with the presence of insulation.

In the third calibration technique under consideration, an electronic pulse (or continuous wave) is sent to a transducer on a waveguide, which then generates an acoustic pulse in the pipe. With this technique, transducers used for calibration would not be used for receiving acoustic leak signals. A method to distinguish anomalous behavior of receivers from anomalous behavior of pulsers would have to be established. The advantage is in the simplicity of setting up a remote capability for continuous in-situ monitoring of an ALD system. The disadvantages are the need for additional transducers on the pipe and possible problems with coupling of waveguides to the pipe.

(4) Sensitivity of Acoustic Leak Detection Systems

The data acquired in this program to date allow us to estimate the sensitivity of an ALD system in a field environment. Figure 1.3 shows the acoustic signal intensity (in a 300-400 kHz window) vs distance along a 10-in. Schedule 80 pipe for 38, 380, and 7600-cm^3/min (0.01, 0.1, and 2-gal/min) leak rates. The data for the two higher leak rates (shaded bands) were determined by extrapolating low-leak-rate data from the two IGSCCs that were studied. The width of each band represents the difference in the extrapolations from the two leaks. The lower limit of each band is obtained by assuming a $(\text{leak rate})^{0.32}$ dependence for the acoustic signal; this is close to the $(\text{leak rate})^{0.28}$ dependence obtained at Battelle Columbus (BCL) with graphite-wool-grown IGSCC in 12-in. pipes. (The BCL data cover four orders of magnitude in leak rate.[5]) For the 300-400 kHz bandwidth, an insertion loss of 5 dB is assumed for the first meter of separation between leak and sensor; thereafter, an attenuation of 2 dB/m is assumed. Also shown in Fig. 1.3 are upper and lower estimates for background noise data. The upper line is derived from the Watts Bar hot functional test. The lower level is a

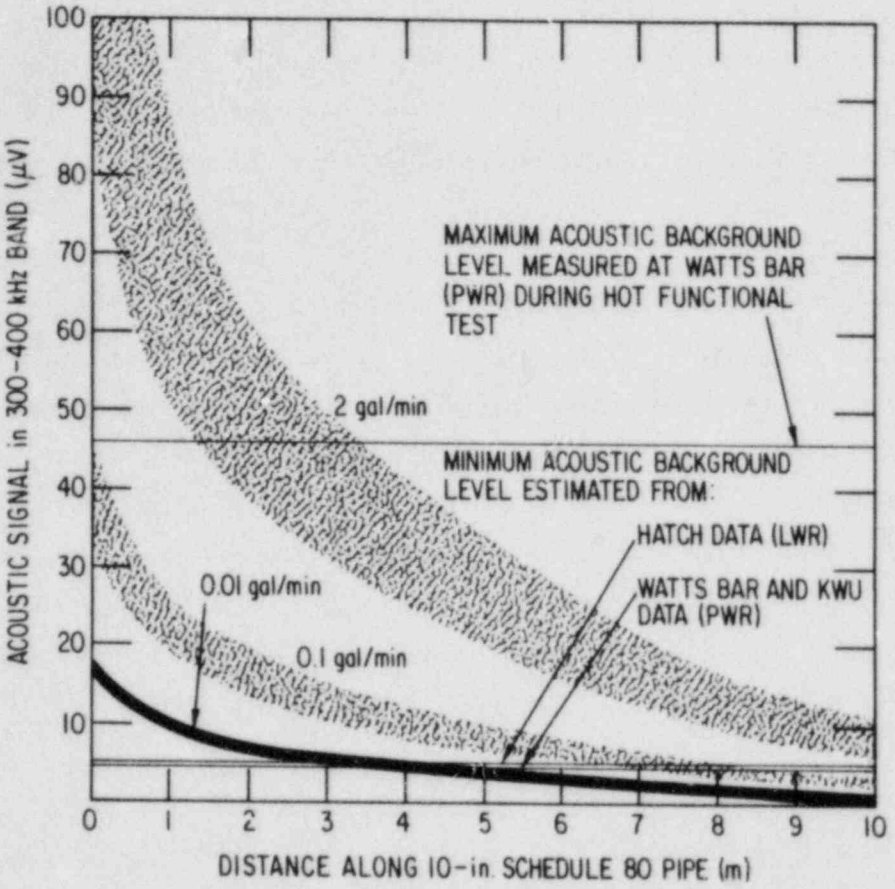

Fig. 1.3. Estimated Acoustic Signal at Various Distances from an IGSCC Leak. Acoustic background data acquired from the Watts Bar (PWR) hot functional test, and levels estimated from Hatch (BWR) acoustic monitoring data, are also shown. Conversion factor: 1 gal = 3800 cm^3.

combination of (1) inferred acoustic background noise from the Hatch installation and (2) data from KWU personnel[6] which indicate that background noise varied by a factor of 10 in different locations in a PWR they monitored. These results suggest that at a distance of 3 m (10 ft), leaks as small as 38 cm^3/min (0.01 gal/min) may be detectable in areas of low background noise, whereas only leaks on the order of 7600 cm^3 (2 gal/min) may be detectable in areas of very high background noise. Leaks as small as 380 cm^3/min (0.1 gal/min) may be detectable at the source, even with very high acoustic background levels.

(5) Studies on Moisture-sensitive Tape

A system to test the sensitivity of moisture-sensitive tape (an alternative technique for leak detection) was constructed in the laboratory. It consists of a 10-in. Schedule 80 pipe section, ∿1 m (3 ft) in length, heated to 260°C (500°F) and covered with reflective insulation. A small (∿6-mm or 1/4-in.) hole was drilled in the insulation, in accordance with installation instructions for the moisture-sensitive tape, so water could drip onto the tape. The tape was mounted on the bottom of the pipe and the open end of a 3.2-mm (1/8-in.)-OD copper steam line was positioned at the top of the pipe directly over the tape to simulate a leak for the initial tests. Physically, the "leak" was 33 cm (13 in.) away from the tape. This configuration simulates the leakage monitoring arrangement for welds in an actual plant, where, according to the supplier, 7-10 cm (3-4 in.) of tape on a stainless steel carrier strap would be placed under each weld to be monitored, with a tube to direct the water to the tape. Up to 700 welds can be monitored with presently available systems.

Two types of moisture-sensitive tape were supplied with the instrumentation. "Sensor B" tape is very sensitive to water. "Sensor A" is a newer type of tape which is less susceptible to false alarms caused by external sources of water. At a temperature of 243°C (470°F) and with a water/steam leak rate of 190 cm^3/min (0.05 gal/min), sensor B responded to the leak within 8.6 minutes. Sensor A, under nearly identical conditions (227°C or 440°F, same leak rate), responded after 28.5 minutes. Sensor B took about 5 minutes to return to normal resistance when dried with a heat gun after the test. Sensor A was not completely dry after 20 minutes with the heat gun. It would probably have to be baked in an oven at ∿100°C for several hours to return to its initial state of resistance. Evaluation of moisture-sensitive tape and comparison with acoustic monitoring are continuing.

b. Nondestructive Evaluation

(1) Ultrasonic Identification of IGSCC in a Manifold End Cap Weld

Cracks were detected on both sides of a manifold end cap weld in the Georgia Power Company's Hatch-2 reactor by ultrasonic ISI techniques. A section of the end cap, including the weld and part of the connecting pipe, was sent to Argonne National Laboratory (ANL) for ultrasonic examination. ANL personnel examined the specimen with a Sonic Mark I pulser-receiver, KB-Aerotech dual 1.5-MHz, 45° shear-wave probe, and Ultragel couplant. A 3.2-mm-diam side-drilled hole was used as a reference reflector. The amplitudes of echo signals obtained from both sides of the weld were generally greater than 10% of DAC values, and showed a variation of ∿10 dB. The echoes from the cap side had greater amplitudes than those from the pipe side. Subsequent destructive analysis revealed a crack on the cap side only. The largest echo signal observed at ANL was from this region, but it was only a few dB larger than other cap-side signals that were produced by geometrical reflectors. At each of two cap-side probe positions, two separate signals with different transit times were detected. In such a case, the two signals could be interpreted as arising from a crack and from the weld root, respectively. However, the destructive analysis revealed that no cracks were present at one of those positions. Both signals at that position were attributable to geometrical reflectors; one arose from the weld root, the other from lack of fusion.

Considerable overcalling of cracks is evident in this example. The overcalling appears to be due to the presence of an undercut on the cap side of the weld and a weld root oriented in such a way that relatively strong signals reflected from the root were detected with the transducer on the pipe side.

(2) Crack Depth Sizing

It is generally believed that IGSCC depths cannot be accurately estimated from the amplitude of the ultrasonic echo signal. This

is because the amplitude is affected by the extreme tightness of the crack, presence of corrosion products between crack surfaces, branching of the crack, and irregular crack faces. As expected, data on echo signal amplitude vs circumferential position showed no correlation with the crack depth measured during destructive analysis of the manifold end cap weld.

Another commonly used method for crack depth sizing is the probe motion (also called dynamic echo or amplitude drop) technique. In this technique, the transducer is moved across the defect and the echo amplitude is plotted as a function of transducer position. The size (depth) of the reflector is related to the distance moved by the transducer between the two "drop points" at which the signal amplitude is 20 dB (or 6 dB) below its maximum value. This technique can provide useful data for reflectors with surfaces normal to the ultrasonic beam, with very rough surfaces, or with irregular geometries. However, in situations where the pipe inner surface was inaccessible, or where angle beam waves were used, attempts to measure IGSCC depths have been unsuccessful: Shallow crack depths were overestimated and deep ones were underestimated. The ANL data are consistent with previous experience; data from the 20-dB drop points, obtained with a 1/4-in., 2.25-MHz, 45° shear wave probe, were independent of depth. Furthermore, the same response was obtained when a geometrical reflector or the end of the pipe was examined. The same conclusion can be drawn from data obtained with 6-dB drop points; that is, no correlation was found between the results of the commonly used probe motion technique and the actual crack depth of an IGSCC specimen.

B. Analysis of Sensitization (J. Y. Park)

1. Introduction

The microstructural changes resulting from thermal exposure, which produce susceptibility to intergranular corrosion, are collectively known as sensitization. It is one of the major causative factors in the IGSCC of austenitic stainless steels in LWR environments. Under normal isothermal heat treatments, sensitization of austenitic stainless steels such as Types 304 and 316 occurs in the temperature range of about 500 to 850°C. However, Type 304 SS may be sensitized at temperatures below this range if carbide nuclei are present at grain boundaries. This low-temperature sensitization (LTS) phenomenon in Type 304 SS has been demonstrated in laboratory experiments in the temperature range from 350 to 500°C. Extrapolations of this behavior to plant operating temperatures (288°C) yield estimated times ranging from 10 to 1000 years for significant LTS to occur. These wide variations have been attributed to differences in the amounts of strain, dislocation densities, and/or impurity element contents of the materials, but with the current level of understanding, the susceptibility to LTS of arbitrary heats of material cannot be assessed.

It is also not clear that the susceptibility to IGSCC produced by long, relatively low-temperature thermal aging can be adequately assessed by conventional measures of the degree of sensitization (DOS), such as the electrochemical potentiokinetic reactivation (EPR) technique or ASTM A262 Practices A through E. These tests have been developed and qualified primarily on the basis of the IGSCC susceptibility produced by high-temperature furnace sensitization or welding.

The objectives of this subtask are to establish the importance of LTS of materials under long-term reactor operating conditions, and to evaluate the effect of thermomechanical history on the correlation of IGSCC susceptibility with tests such as the EPR technique and ASTM A262 Practices A through E.

2. Technical Progress

It is generally understood that plastic deformation increases sensitization kinetics by introducing short-circuit diffusion paths in material and also possibly by enhancing carbide nucleation. The effect of plastic deformation on the sensitization behavior of Type 304 SS (Heat No. 10285) was investigated. Specimens were solution heat treated at 1050°C for 0.5 h and aged at 700°C for 10 min to nucleate carbide precipitates. The specimens were then deformed at 0-10% plastic strain and aged at temperatures in the range of 288-600°C. EPR values were measured after the latter aging step. The results for the specimens with 0 and 5.3% plastic strain after aging at 500, 550, and 600°C are summarized in Table 1.3. The deformed specimens showed larger EPR values than the undeformed specimens. The largest absolute increase in EPR value associated with deformation was observed for the heat treatment (600°C/24 h) that produced the highest degree of sensitization (DOS) in the absence of deformation. The effects of aging conditions, amount of plastic strain, and heat-to-heat variation are now being investigated.

TABLE 1.3. Effect of Plastic Strain on Sensitization

Post-Strain Aging[a]	EPR, C/cm^2	
	ε_p = 0%	ε_p = 5.3%
500°C/100 h	3	5
550°C/24 h	6	8
600°C/24 h	16	21

[a]Specimens were heat treated (1050°C/0.5 h + 700°C/10 min) prior to plastic strain.

Low-temperature aging of the specimens from 4-inch-diameter Type 304 SS (Heat No. 53319) pipe weldments with four different remedy treatments (IHSI, HSW, LPHSW, and CRC) is continuing. Since the weldments were

sensitized to a significantly high level during welding, as reported earlier, they may not fully reveal the effect of further LTS. Another heat of Type 304 SS (Heat No. 82103) with 0.05 wt.% carbon was examined as a possible alternative material. EPR values were measured after a solution heat treatment (1050°C/1 h) and aging at 550-750°C for 0.08-24 h. The solution heat treatment caused extensive and uneven grain growth, and the aging resulted in excessively high EPR values (e.g., 66 C/cm^2 after a 700°C/1 h aging). Therefore, this heat was not chosen for further investigation.

Studies on the effect of thermomechanical history on the correlation of IGSCC susceptibility with various DOS measurements are continuing. CERT tests were performed on Type 304 SS (Heat No. 10285) in a high-purity water environment with 8 ppm dissolved oxygen at 289°C and a nominal strain rate of 2×10^{-6} s^{-1}. Low-temperature aging at 450°C for 1000 h resulted in an EPR value of 2 C/cm^2, and caused IGSCC (intergranular failure with 17% uniform elongation), as shown in Fig. 1.4. As reported previously,[7] aging at 500°C for 24 h did not cause IGSCC.

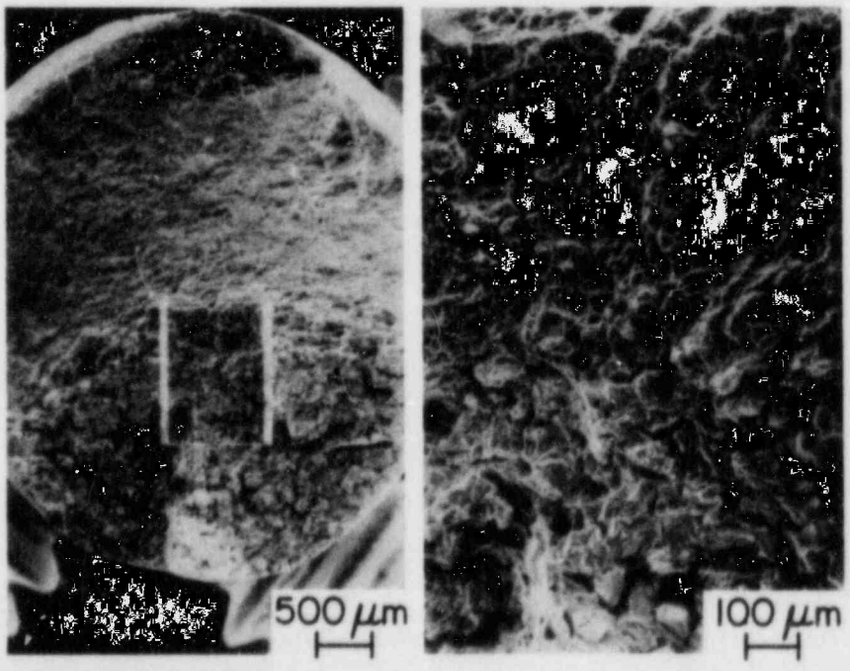

Fig. 1.4. Fracture Surface of Type 304 SS CERT Specimen Tested at 289°C and $\dot{\varepsilon} = 2 \times 10^{-6}$ s^{-1} after Aging at 450°C for 1000 h.

Additional data are needed to determine the correlation between EPR value and IGSCC susceptibility. CERT tests and EPR measurements are under way for additional aging conditions. Results for a Type 304 SS (Heat No. 10285) specimen confirmed the capability of the EPR technique to detect grain boundary chromium depletion: The specimen was sensitized to an EPR value of 34 C/cm^2 by a 750°C/24 h treatment, but prolonged aging (for 240 h) at the same temperature substantially decreased the EPR value to 4 C/cm^2. During the long-term aging, healing of the chromium depletion occurred.

In May 1983, the ASTM G1 main committee and the G1-08 subcommittee voted on the proposed ASTM standard for EPR measurement. A few negative votes were cast. Discussions are in progress to resolve the issue.

C. Crack Growth Rate Studies (J. Y. Park and W. J. Shack)

1. Introduction

The early instances of IGSCC in operating BWRs generally occurred in small pipes, and the response to the detection of IGSCC was generally to repair or replace the cracked piping immediately. It is now clear that for reactors with standard Type 304 SS piping material, cracking can occur anywhere in the recirculation system, including the main recirculation line. Because of the severe economic consequences of long forced outages for repair or replacement, the utilities will consider other approaches for dealing with cracked pipe. The possibilities include continued operation and monitoring for any subsequent growth for an indefinite period, continued operation and monitoring until a repair can be scheduled to minimize outage, and immediate repair and replacement.

Understanding crack growth behavior is, of course, important for other reasons besides assessing the safety implications of flawed piping. A better understanding would permit a more rational extrapolation of laboratory test results to the prediction of behavior in operating plants. Current work on the measurement of crack growth rates seeks to characterize these rates in terms of the linear elastic fracture mechanics (LEFM) stress intensity as well as the level of sensitization and the amount of oxygen present in the coolant. The work in this subtask is aimed at a systematic evaluation of the validity of the use of LEFM to predict IGSCC growth. The capability of data obtained under one type of loading history to predict crack growth under a different loading history will be investigated. The effect of flaw geometry on crack propagation rates will also be considered.

2. Technical Progress

Crack growth rate tests have continued for Type 304 SS (Heat No. 10285) 1TCT specimens C-09, -11, and -17 in water with 8 ppm oxygen at 289°C and 8.3 MPa (1200 psi). The current series of tests will establish (at a fixed K) the effect of load ratio R and frequency f on the growth rate, and whether these effects can be understood in terms of the crack-tip

strain rate. The specimens had been furnace heat treated for 700°C/10 min, with a subsequent additional treatment of 450°C/146 h, 450°C/250 h, or 500°C/24 h. The EPR values of companion test coupons were 8, 4, and 15 C/cm^2 for SPC C-09, -11, and -17, respectively. Growth rates have been reported previously[8] for the following conditions: maximum stress intensities (K_{max}) ranging from 19 to 34 $MPa \cdot m^{\frac{1}{2}}$; R = 0.5, 0.6, 0.7, 0.8, 0.94, and 1; and f = 0, 2×10^{-3}, and 1×10^{-1} Hz. During the current reporting period, additional tests were carried out at K_{max} = 30-32 $MPa \cdot m^{\frac{1}{2}}$; R = 0.5 and 0.8; and f = 1×10^{-3} and 2×10^{-3} Hz. Sawtooth waveforms with an unloading time of 5 sec were used for the cyclic-loading tests. The crack length was continuously monitored by the compliance method with an in-situ clip gage. Figure 1.5 shows crack length vs test time for the three specimens. Interruptions or changes in the test conditions (R, f, or K value) occurred at times I through XVIII. After each interruption, a retardation of crack propagation was apparent; the duration was on the order of 10^2 h. Average crack propagation rates were obtained by least-squares linear regression analysis for each test condition, and the results for specimens C-11 and C-17, along with those reported previously,[8] are summarized in Table 1.4. The crack lengths for specimens C-09 and C-17 appeared to decrease beyond interruption IX (Fig. 1.5); this suggested that the clip gages had begun to malfunction. Therefore, average crack propagation rates were not calculated for specimen C-09, or for specimen C-17 beyond interruption IX.

Ford[9] has proposed that the crack growth rate is proportional to the square root of the crack-tip strain rate, i.e.,

$$\dot{a}_{IGSCC} = A \, \dot{\varepsilon}_T^{\,n} \, . \qquad (1.1)$$

As discussed in Section I.D below, this relation is consistent with data obtained from CERT tests at different strain rates. Analysis of the fracture mechanics crack growth tests requires an expression for the crack-tip strain rate. Under constant applied loads, the crack-tip strain rate is determined by the time-dependent plastic deformation, i.e., creep, near the crack tip. For cyclic applied loads of sufficiently high frequency (and sufficiently low R values), the strains are imposed by the external loading mechanism.

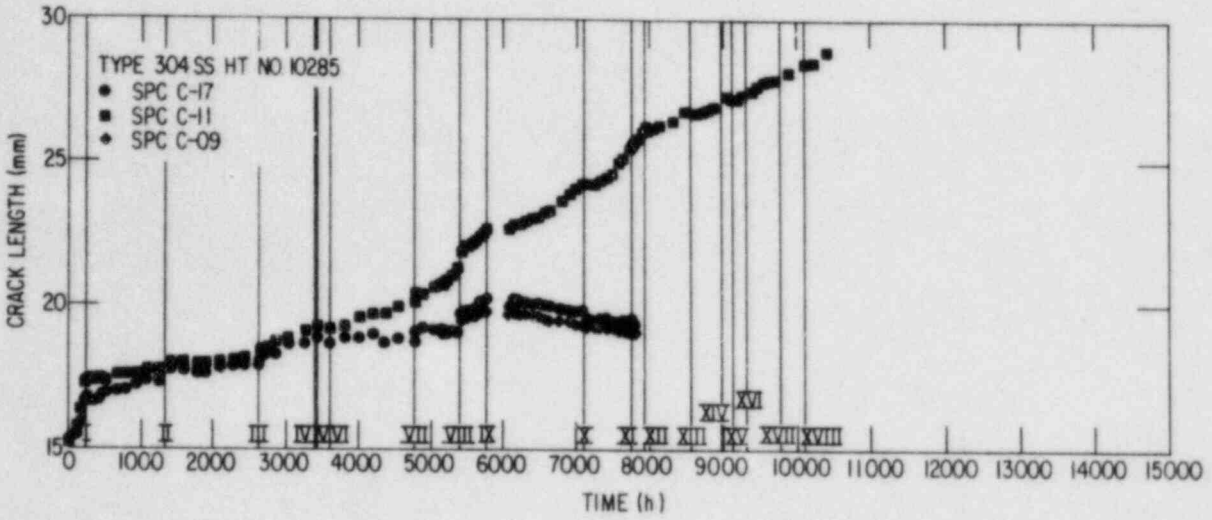

Fig. 1.5. Plots of Crack Length vs Time for Heat No. 10285 Specimens.

TABLE 1.4. Crack Propagation Rates in Type 304 SS Specimens (Heat No. 10285) Sensitized to Two Different Levels and Tested in 289°C Water with 8 ppm O_2

f, Hz	R	$\dot{\varepsilon}_T$, s^{-1}(a)	K_{max}, MPa·$m^{1/2}$	å, m/s
		SPC C-11 (EPR = 4 C/cm^2)		
0	1	-	33-34	1.2×10^{-10}
1×10^{-3}	0.5	1.4×10^{-4}	31-32	2.6×10^{-10}
2×10^{-3}	0.5	2.7×10^{-4}	30-31	8.9×10^{-10}
2×10^{-3}	0.5	2.7×10^{-4}	30-33	3.4×10^{-9}
2×10^{-3}	0.6	1.7×10^{-4}	32-33	6.6×10^{-10}
2×10^{-3}	0.7	9.3×10^{-5}	30-31	3.4×10^{-10}
2×10^{-3}	0.7	9.3×10^{-5}	32-33	5.9×10^{-10}
2×10^{-3}	0.8	4.1×10^{-5}	29-32	7.4×10^{-10}
2×10^{-3}	0.8	4.1×10^{-5}	30-31	4.4×10^{-10}
1×10^{-1}	0.94	1.8×10^{-4}	30-31	3.1×10^{-10}
1×10^{-1}	0.94	1.8×10^{-4}	31-32	1.9×10^{-10}
		SPC C-17 (EPR = 15 C/cm^2)		
0	1	-	32-33	2.2×10^{-10}
2×10^{-3}	0.5	2.7×10^{-4}	30-32	2.8×10^{-9}
2×10^{-3}	0.6	1.7×10^{-4}	28-29	5.6×10^{-10}
1×10^{-1}	0.94	1.8×10^{-4}	30	2.1×10^{-10}

[a] $\dot{\varepsilon}_T = -1/T \ln [1 - (1 - R)^2/2]$.

Estimates of the crack-tip strain rates in this case can be obtained from LEFM. Scott and Truswell[10] have suggested a relation of the form

$$\dot{\varepsilon}_T = - 1/T \ln [1 - (1 - R)^2/2], \qquad (1.2)$$

where T is the rise time for the tensile portion of the load cycle. Related expressions for crack-tip strains in fatigue have been proposed by Rice[11] and others. Equation (1.2), since it neglects constant-load creep, predicts $\dot{\varepsilon}_T = 0$ for the constant-load case. It also predicts that the crack-tip strain rate is independent of the value K and hence, together with Eq. (1), predicts that the crack growth rate is independent of K. This prediction is contradicted by many experimental observations. Estimates of the crack-tip strain rate obtained from Eq. (1.2) are included in Table 1.4. For the tests in which both R and f were varied, the data differ by an order of magnitude from predictions based on Eqs. (1.1) and (1.2) and no significant correlation can be established, as shown in Fig. 1.6. Tests are currently in progress to explore additional R values and frequencies, and alternative formulations for the crack-tip strain rates are being explored.

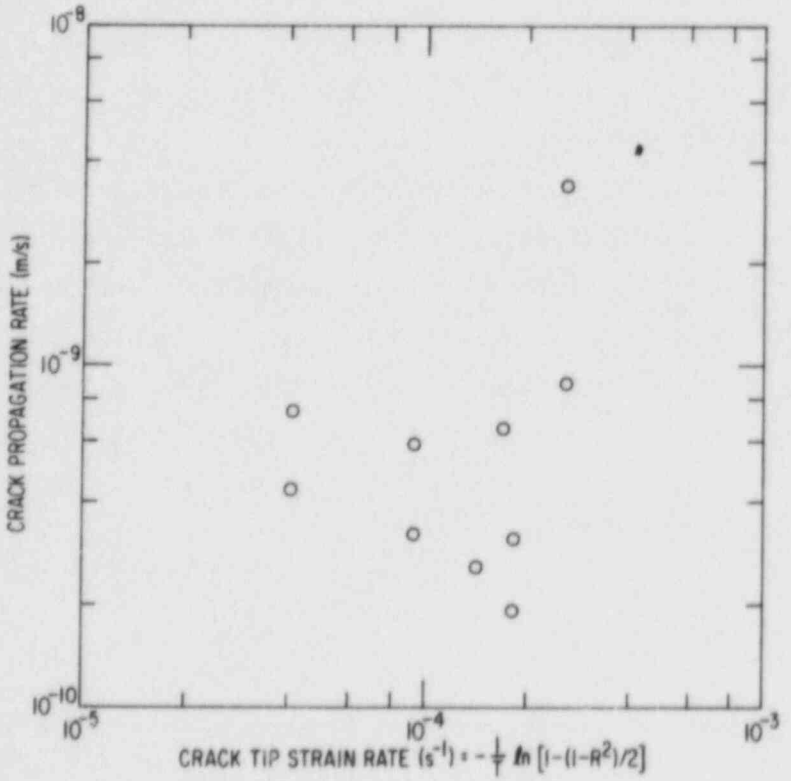

Fig. 1.6. Crack Propagation Rate vs Crack-Tip Strain Rate for Type 304 SS (Heat No. 10285).

D. Evaluation of Nonenvironmental Corrective Actions (P. S. Maiya and W. J. Shack)

1. Introduction

The fundamental premises of the current efforts to prevent IGSCC in BWR piping are (1) that IGSCC involves a complex interaction among susceptibility of a material to damaging conditions over time (sensitization), the stresses acting on the material, and the nature of the environment, and (2) that suitable alteration or variation of these parameters can prevent IGSCC in materials of interest. Nonenvironmental corrective actions involve mitigation of either the material's susceptibility to sensitizing conditions or the state of stress on the inside surface of the weldment. Such actions include the use of fabrication or treatment techniques that improve the IGSCC resistance of susceptible materials (e.g., Type 304 SS) and the identification of alternative materials that are inherently more resistant to IGSCC.

The objective of the current work is an independent assessment of the proposed remedies developed by the utilities and the vendors. Additional testing and research will be done to eliminate gaps in the existing data base on alternative materials and fabrication methods, and to develop a better understanding of the relation between the existing laboratory results and satisfactory in-reactor operating performance. Current efforts in this task include additional screening tests for alternative materials, environmental pipe tests under alternate loading conditions, and the study of stress redistribution near weldments to determine the effect of in-service loading conditions on techniques for reducing residual stress loads.

2. Technical Progress

a. Impurity and Strain Rate Effects

The slow-strain-rate experiments to determine the relative susceptibility of Types 316NG, 316, and 304 SS in impurity (e.g., Cl^- and

SO_4^{2-} at levels consistent with Regulatory Guide 1.56 limits) environments are continuing. Recently, two CERT tests were performed in a nominal BWR-type aqueous environment with 0.2 ppm dissolved O_2 and 0.1 ppm SO_4^{2-}: (1) a 316NG/308L weldment with an additional heat treatment (500°C/24 h) was tested at a strain rate of $\dot{\varepsilon} = 4 \times 10^{-8}$ s^{-1}; (2) a 316NG SS specimen (SA + 650°C/24 h) was tested at $\dot{\varepsilon} \simeq 1 \times 10^{-7}$ s^{-1}. Both materials exhibited susceptibility to transgranular stress corrosion cracking (TGSCC). In test (1), which was completed without interruption, the fracture occurred in the base metal at a distance of ∿1.3 cm from the weld/base-metal interface (i.e., outside the HAZ); this contrasts with results obtained for conventional Types 316/308L and 304/308L SS weldments, in which IGSCC fracture occurred in the HAZ. Test (2) was interrupted three times because of malfunctions of the feedwater pump, and the 316NG SS specimen failed at a strain (ε_f) of ∿20.0%. However, a repeat of the test, which is now in progress, has an accumulated strain of ∿35.0%. Figure 1.7 compares the average crack growth rates $\dot{a}_{av}$ in tests (1) and (2) with some limited data obtained from sensitized (EPR = 17 C/cm^2) conventional Type 316 SS, tested under similar conditions but at higher strain rates. The comparison suggests that the transgranular crack growth rate in the nuclear-grade material in a BWR-type environment is approximately an order of magnitude lower than the intergranular crack growth rate in the conventional Type 316 SS (EPR = 17 C/cm^2). In addition, the limited experimental results (indicated by symbols) appear to be consistent with the predictions of a model (solid line with slope of 1/3) discussed in previous reports.[12-14] Further work is in progress to establish more definitively the relative SCC susceptibility of the two materials in BWR-type environments.

The relative SCC susceptibility of Types 316NG and 316 SS in the present tests is similar to that observed in a more aggressive environment representative of off-normal conditions (water with 8 ppm dissolved O_2 and 0.5 ppm Cl^-), as shown in Fig. 1.8, although the absolute values of $\dot{a}_{av}$ for the two materials are affected by the environment. A comparison of Figs. 1.7 and 1.8 shows that the average crack growth rates in the aggressive environment are approximately 5 times higher than those determined in the BWR-type environment.

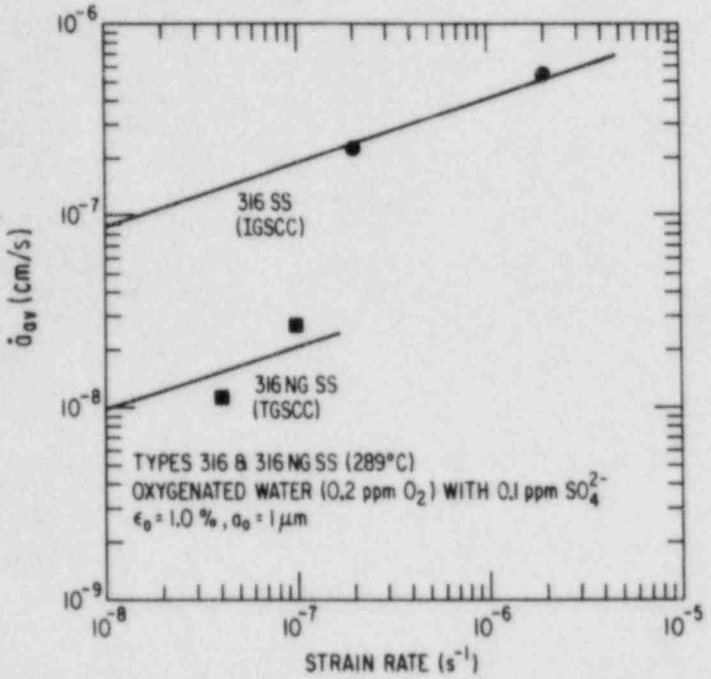

Fig. 1.7. Relative SCC Susceptibility of Types 316NG and 316 SS as a Function of Strain Rate in a Normal BWR-Type Environment. Solid lines show predictions of the phenomenological model discussed in Refs. 12-14.

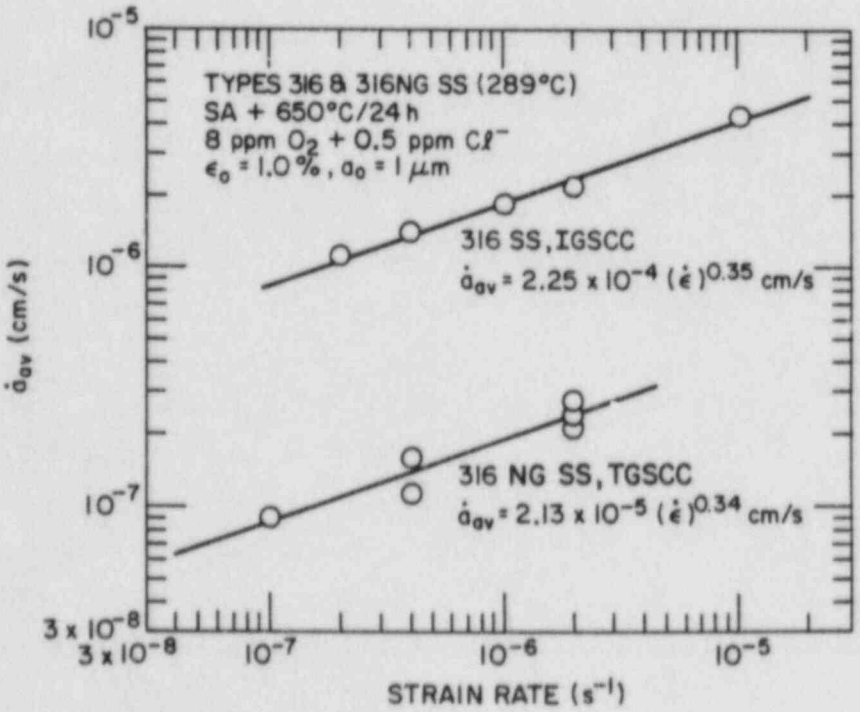

Fig. 1.8. Relative SCC Susceptibility of Types 316NG and 316 SS as a Function of Strain Rate in an Off-Normal BWR-Type Environment.

The relative SCC susceptibility of Types 316NG and 316 SS can also be illustrated by using other parameters such as maximum stress. For example, Fig. 1.9 shows a normalized plot of σ_{max} (SCC)/σ_{max} (no SCC) versus $\dot{\varepsilon}$. The quantity σ_{max} (SCC) represents the maximum stress in the strain rate regime where SCC (IGSCC or TGSCC) occurs and σ_{max} (no SCC) is the maximum stress observed for the material under conditions where failure is ductile in nature with no evidence of SCC. The latter stress is expected to be independent of $\dot{\varepsilon}$ at 289°C. Figure 1.9 shows that in an aggressive environment (8 ppm O_2 + 0.5 ppm Cl^-), the decrease in σ_{max} for Type 316NG SS begins at $\dot{\varepsilon} \lesssim 10^{-7}$ s^{-1}, whereas the decrease for Type 316 SS starts at a value of $\dot{\varepsilon}$ at least two orders of magnitude higher; this reflects the increased resistance to SCC of Type 316NG SS compared to sensitized Type 316 SS. The IGSCC susceptibility data for Type 316 SS shown in Fig. 1.9 suggest that σ_{max} (SCC) becomes constant and virtually independent of $\dot{\varepsilon}$. This constant stress may be related to the "threshold stress" required in a constant-load test to propagate an intergranular crack in 316 SS in the impurity environment. For transgranular cracking in 316NG, the strain rate at which σ_{max} (SCC) becomes constant is expected to be at least one or two orders of magnitude lower than that for intergranular cracking in 316 SS.

In a previous report[12] we discussed the development of a model which is consistent with the observed and postulated crack growth behavior and with a fracture criterion; it relates the IGSCC susceptibility parameters to the strain rate (in the regime of practical interest where the severity of cracking increases with a decrease in strain rate) in terms of a power law. In particular, the following correlations were obtained:

$$\dot{a}_{av} = A(AC/J_c)^{1/3}\dot{\varepsilon}^{1/3}, \tag{1.3}$$

$$t_f = (J_c/AC)^{2/3}\dot{\varepsilon}^{-2/3}, \tag{1.4}$$

$$\varepsilon_f = (J_c/AC)^{2/3}\dot{\varepsilon}^{1/3}, \text{ and} \tag{1.5}$$

$$a_f = A(J_c/AC)^{1/3}\dot{\varepsilon}^{-1/3}, \tag{1.6}$$

where t_f is the time to failure; a_f is the maximum crack length at failure; A is a constant related to the crack growth behavior which is independent of

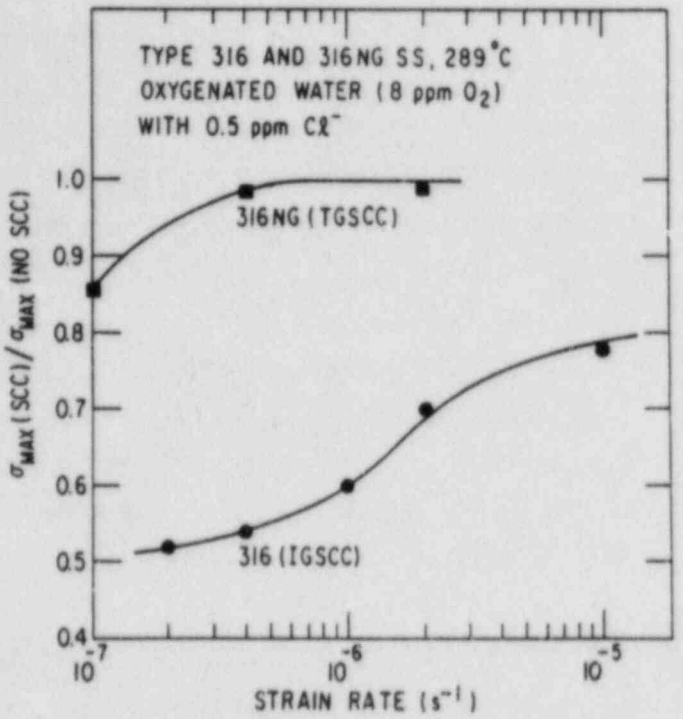

Fig. 1.9. Variation of Normalized Maximum Stress with Strain Rate for Types 316 and 316NG SS.

$\dot{\varepsilon}$ but is a function of the microstructural state of the material (for example, degree of sensitization) and the environment; and J_c/C is a constant that depends on the material and geometry but is assumed to be independent of $\dot{\varepsilon}$. Good agreement was obtained between the results of the analysis and CERT tests performed on Type 316 SS (EPR = 17 C/cm^2) in water with 8 ppm O_2 and 0.5 ppm Cl^-. Comparison of model predictions with published results[15-17] suggests that, as expected, the analysis is equally applicable to Type 304 SS in oxygenated water (0.2 and 8 ppm O_2) at 289°C. We have now obtained some further results to demonstrate the general applicability of the analytical results to Types 304 and 316 SS in a variety of environments. Figure 1.10 shows the failure time as a function of strain rate for Type 316 SS (EPR = 17 C/cm^2) in water with 8 ppm O_2 and 0.5 ppm Cl^-, for Type 304 SS (EPR = 24 C/cm^2) in high-purity water with 0.2 ppm O_2, and for Type 304 SS in water with 0.2 ppm dissolved O_2 and 0.1 ppm SO_4^{2-}. The results suggest that regardless of the different microstructural states of the material and different environmental conditions used, the failure time and the (nominal) strain rate are related by a power law with the same

strain-rate exponent of ∿-0.7. The experimentally observed slopes in Fig. 1.10 are in satisfactory agreement with that predicted by the model [see Eq. (1.7)]. Thus, the analysis of the strain rate effects on IGSCC susceptibility embodied in Eqs. (1.3)-(1.7) is applicable to a range of water chemistries for conventional piping materials sensitized to different degrees and may provide a method of extrapolation to strain rates characteristic of an operating BWR.

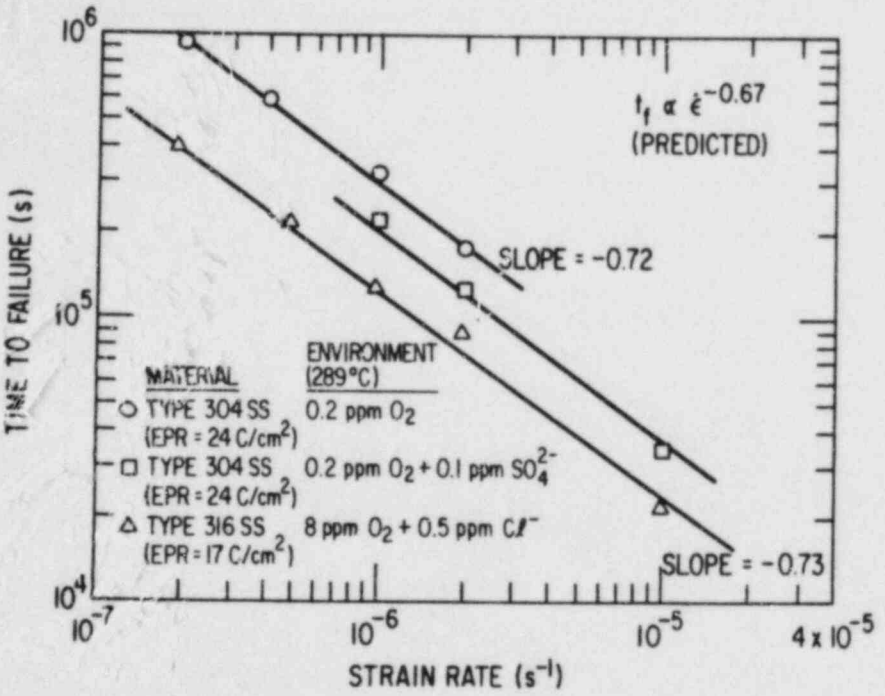

Fig. 1.10. Time to Failure versus Strain Rate for Types 304 and 316 SS in Different BWR-related Environments.

As discussed earlier,[12,18] we also developed a method for computing an average crack-tip strain rate by use of a J-integral approach. Specifically, the average crack-tip strain rate can be calculated from the CERT parameters as follows:

$$\bar{\dot{\epsilon}}_T = \frac{1}{t_f - t_o}\left(\ln \frac{\epsilon_f}{\epsilon_o} + \ln \frac{\epsilon_f}{a_o}\right) \qquad (1.7)$$

where t_o, ϵ_o, and a_o are the time, strain, and crack length at the initiation of the crack, respectively, and the subscript f refers to values at failure.

A comparison of log-log plots of $\dot{a}_{av}$ versus $\bar{\dot{\epsilon}}_T$ for Type 316 SS in a chloride environment over a wide range of (nominal) strain rates from 10^{-5} to 2×10^{-7} s^{-1} (see Fig. 1.11) shows that the average crack growth rate is proportional to the square root of the average crack-tip strain rate. Furthermore, the results are fairly insensitive to the choice of different crack initiation parameters. The observed dependence of average crack growth rate on crack-tip strain rate is in good agreement with that deduced from a slip- dissolution model proposed by Ford.[15,16]

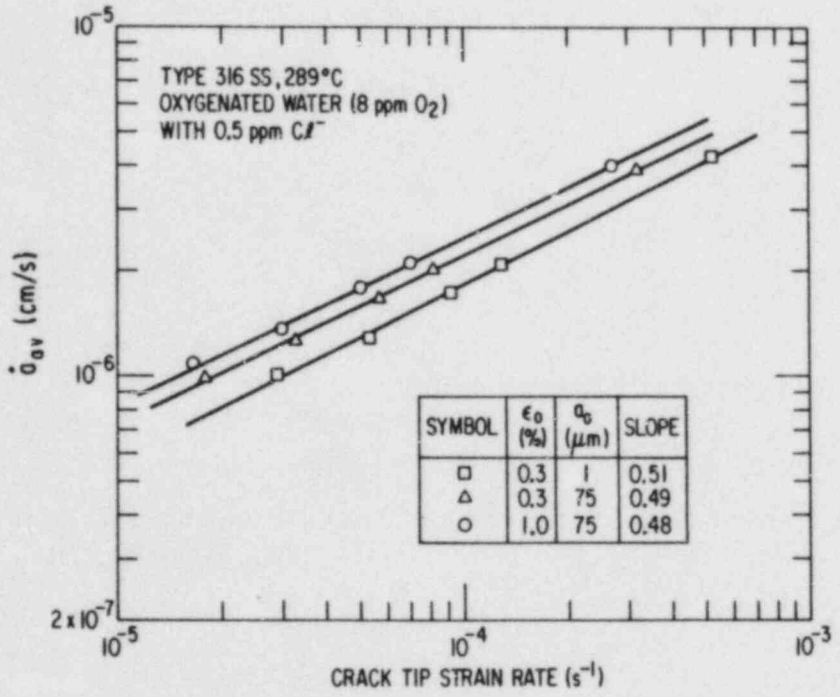

Fig. 1.11. Relationship between Average Intergranular Crack Growth Rate ($\dot{a}_{av}$) and Crack-Tip Strain Rate ($\bar{\dot{\epsilon}}_T$) for Different Values of Crack Initiation Parameters. Average crack-tip strain rate was calculated from Eq. (1.7).

b. Stress/Strain/Strain-Rate Relations for Sensitized Materials

Stress-relaxation experiments are being performed to determine the stress/strain/strain-rate relations for Types 316 and 304 SS in three material conditions (i.e., as-received, solution annealed, and sensitized at

temperatures of 28-300°C). These constitutive relations are important in determining the strain rates associated with different loading histories. We have completed measurements at 28°C and the results are being analyzed. Plans are currently under way to modify the system to allow measurements at high temperature (e.g., 289°C). Analyses of data and the form of constitutive relations are similar in the temperature range from 28-300°C because of the similarity in the shape of stress-relaxation plots (viz., log-log plots of stress versus non-elastic strain rate). From the data obtained for the sensitized Type 316 SS (SA + 650°C/50 h, EPR > 17 C/cm^2), it was found[18] that a state variable approach[19] described the data fairly well. Recently, the experimental stress-relaxation results obtained at 28°C for Type 304 SS (SA + 650°C/24 h, EPR $\simeq$ 39 C/cm^2) with initial stresses of 1.0 σ_y, 1.1 σ_y, 1.2 σ_y, 1.3 σ_y, 1.4 σ_y and 1.5 σ_y (where σ_y = 233 MPa or 33.8 ksi) have been analyzed to obtain stress/strain-rate data for different strains over a range of strain rates from 10^{-4} to 10^{-10} s^{-1}. As shown in Fig. 1.12, the log-log plots of stress versus non-elastic strain rate exhibit the characteristic upwardly concave shape. These and other data will be analyzed by using the constitutive equations in a manner similar to that described earlier. Also, a comparison of the strain rate response of the Types 304 and 316 SS sensitized to different degrees for several plastic strains (or imposed stresses) would establish the dependence of material parameters (which appear in the constitutive equations) on the microstructural state of the conventional piping materials and would thus contribute to a better understanding of the effects of loading histories on IGSCC susceptibility.

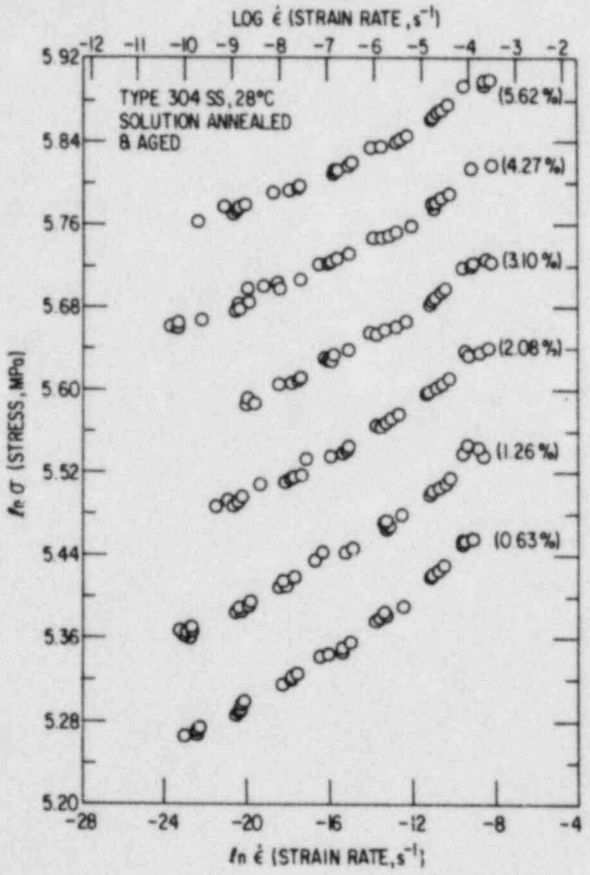

Fig. 1.12. Stress Relaxation Plots of Stress versus Non-elastic Strain Rate for Type 304 SS (SA + 650°C/24 h, EPR $\tilde{-}$ 39 C/cm^2). The initial non-elastic strains produced by the initial stresses of 1.0-1.5 σ_y (where σ_y ≈ 233 MPa) are indicated.

E. Evaluation of Environmental Corrective Actions (W. E. Ruther, W. K. Soppet, and T. F. Kassner)

1. Introduction

The potential effectiveness of proposed actions to solve or mitigate the problem of IGSCC in BWR piping and safe ends through modifications of the water chemistry is being evaluated. Although the reactor coolant environment has a profound influence on the performance and reliability of nuclear power-plant components, the synergistic effects of oxygen (produced by radiolytic decomposition of the water) and impurities (e.g., H_2SO_4 from decomposition of ion exchange resins during periodic intrusions into the primary system) on the IGSCC susceptibility and crack growth properties of sensitized Type 304 SS have not been investigated adequately. Also, it is not clear whether the potential benefits associated with small additions of hydrogen to the coolant can be realized in the presence of impurities within the normal operating limts of pH (5.6 to 8.6 at 25°C) and specific conductance ($\leq$1 μS/cm at 25°C) of the reactor coolant water.

During this reporting period, additional results have been obtained from CERT tests on a reference heat of Type 304 SS with two levels of sensitization, in 289°C water containing 0, 1, and 10 ppm sulfate (as H_2SO_4) with $\lesssim$0.005 and 2.0 ppm dissolved oxygen and hydrogen, respectively. The extent to which the SCC susceptibility is reflected in the crack growth behavior of the steel under low-frequency, moderate-stress-intensity, and high-R loading is also being evaluated in high-purity water with 8 ppm oxygen, and in water containing 0.1 ppm sulfate and 0.2 ppm oxygen at 289°C. Results of high-temperature pH measurements of dilute H_2SO_4, NaOH and H_2SO_4/Na_2SO_4 solutions by means of a solid-electrolyte sensor are also reported.

2. Technical Progress

a. Results of CERT Experiments on Sensitized Type 304 SS

Additional results pertaining to the influence of dissolved oxygen, hydrogen, and sulfate (as H_2SO_4) on the SCC susceptibility of

sensitized Type 304 SS have been obtained from CERT experiments in 289°C water. The specimens were sensitized to EPR values of 2 and 20 C/cm^2 during heat treatments at 700°C for 0.25 h plus 500°C for 24 h and 700°C for 12 h, respectively. The results, which were not included in the previous report,[20] were obtained in water containing 0, 1, and 10 ppm sulfate (as H_2SO_4) with $\lesssim$0.005 and 2.0 ppm dissolved oxygen and hydrogen, respectively. The very low dissolved oxygen concentration was obtained by deaeration plus addition of hydrazine to the feedwater. Measurements of dissolved oxygen by means of commercial on-line instruments (Beckman Model 7002 and Leeds and Northrup Model 7931) were found to be unreliable in the presence of dissolved hydrogen in the water (negative readings were obtained in several instances). Conductometric (thallium column) and colorimetric (CHEMmetrics ampules) measurements confirmed that the oxygen levels were essentially zero. Gas chromatographic analysis of water samples indicated that the dissolved-hydrogen concentration was in good agreement with the concentration calculated from the hydrogen overpressure on the feedwater tank.

Results of the CERT experiments on specimens with both levels of sensitization at 289°C and a strain rate of 1 x 10^{-6} s^{-1} are summarized in Table 1.5. The time to failure and maximum stress in water containing ~0.005, 0.03 and 0.2 ppm dissolved oxygen with 0.5 or 2.0 ppm hydrogen are shown for the lightly (EPR = 2 C/cm^2) and moderately (EPR = 20 C/cm^2) sensitized steels in Figs. 1.13 and 1.14, respectively. The curves indicate a further increase in the resistance to SCC as the dissolved oxygen concentration decreases from ~0.03 to $\lesssim$0.005 ppm in simulated BWR-quality water. Also, the intergranular or granulated fracture morphology was observed only at the highest sulfate concentration (10 ppm) in water containing ~0.005 ppm oxygen and 2.0 ppm hydrogen. The degree of sensitization of the steel does not appear to be a significant factor in the SCC susceptibility, particularly at low dissolved oxygen concentrations ($\lesssim$0.03 ppm).

During the CERT experiments, the electrochemical potentials of Type 304 SS and a platinum electrode were monitored as a function of time. The potentials were measured at 289°C relative to an external 0.1M KCl/AgCl/Ag reference electrode[21] and the values were converted to the standard hydrogen electrode (SHE) at 289°C. Typical potential versus time curves are shown in

TABLE 1.5. Results of CERT Tests on Sensitized Type 304 SS Specimens[a] (Heat No. 30956) in Water with Different Oxygen, Hydrogen, and Sulfate (H_2SO_4) Concentrations at 289°C and $\dot{\varepsilon} = 1 \times 10^{-6}$ s^{-1}

Test No.	EPR, C/cm^2	Feedwater Chemistry					Failure Time, h	Maximum Stress, MPa	Total Elong., %	Reduction in Area, %	Fracture Morphology[b]
		Oxygen, ppm	Hydrogen, ppm	SO_4^{2-}, ppm	Cond., µS/cm	pH at 25°C					
57	2	0.25	0.5	10.0	71.0	3.8	64	364	23	27	0.21D, $0.79G_3$
39	2	0.20	0.5	1.0	8.0	4.8	45	291	16	15	0.19D, 0.81I
35	2	0.18	0.6	0.1	0.8	5.8	74	413	26	27	0.49D, 0.51I
41	2	0.20	0.5	0.01	0.2	6.1	81	493	29	29	0.58D, 0.42I
47	2	0.07	0.5	0.1	0.9	5.8	133	500	48	48	0.57D, 0.43T
51	2	0.03	0.5	10.0	71.0	3.8	67	383	24	25	$0.30D, 0.70G_3$
49	2	0.03	0.5	1.0	8.0	4.8	119	495	43	40	$0.45D, 0.55G_2$
37	2	0.05	0.5	0.1	0.8	5.8	129	510	46	46	$0.43D, 0.57T^2$
59	2	0.03	0.5	0.1	0.8	5.8	118	504	43	48	0.63D, 0.37T
43	2	0.03	0.5	0.01	0.2	6.1	128	514	45	46	0.67D, 0.33T
64	2	<0.005[c]	2.0	10.0	26.0	4.3	110	475	40	40	$0.48D, 0.52G_2$
67	2	<0.005[c]	2.0	1.0	4.4	8.9	126	498	45	47	0.78D, 0.22T
68	2	<0.005[c]	2.0	0	1.1	8.4	147	518	59	65	0.77D, 0.23T
58	20	0.23	0.5	10.0	71.0	3.8	66	349	24	23	$0.34D, 0.66G_3$
40	20	0.20	0.5	1.0	8.0	4.8	51	261	18	21	0.35D, 0.65I
36	20	0.20	0.5	0.1	0.9	5.8	80	425	38	38	0.46D, 0.32T, 0.22I
52	20	0.03	0.5	10.0	69.0	3.8	72	356	26	27	0.28D, 0.72I
50	20	0.03	0.5	1.0	8.0	4.8	115	502	42	34	$0.70D, 0.30G_2$
38	20	0.05	0.5	0.1	0.8	5.8	124	499	44	44	$0.68D, 0.32T^2$
44	20	0.02	0.5	0.01	0.2	6.1	125	513	44	45	0.70D, 0.30T
65	20	<0.005[c]	2.0	10.0	26.0	4.4	91	437	33	32	0.34D, 0.66I
66	20	<0.005[c]	2.0	1.0	4.4	8.9	126	502	45	48	0.57D, 0.43T
69	20	<0.005[c]	2.0	0	1.0	8.5	141	523	51	60	0.93D, 0.07T

[a]Specimens were exposed to the environment for ~20 h at 289°C before straining.

[b]Ductile (D), transgranular (T), granulated (G), intergranular (I), in terms of the fraction of the reduced cross-sectional area. Characterization of the fracture surface morphologies is in accordance with the illustrations and definitions provided in Alternate Alloys for BWR Pipe Applications: Sixth Semiannual Progress Report, April-September 1980, General Electric Company Report NEDC-23750-8, pp. 5-70 to 5-81.

[c]Hydrazine was added to the feedwater to decrease the oxygen level to <0.005 ppm.

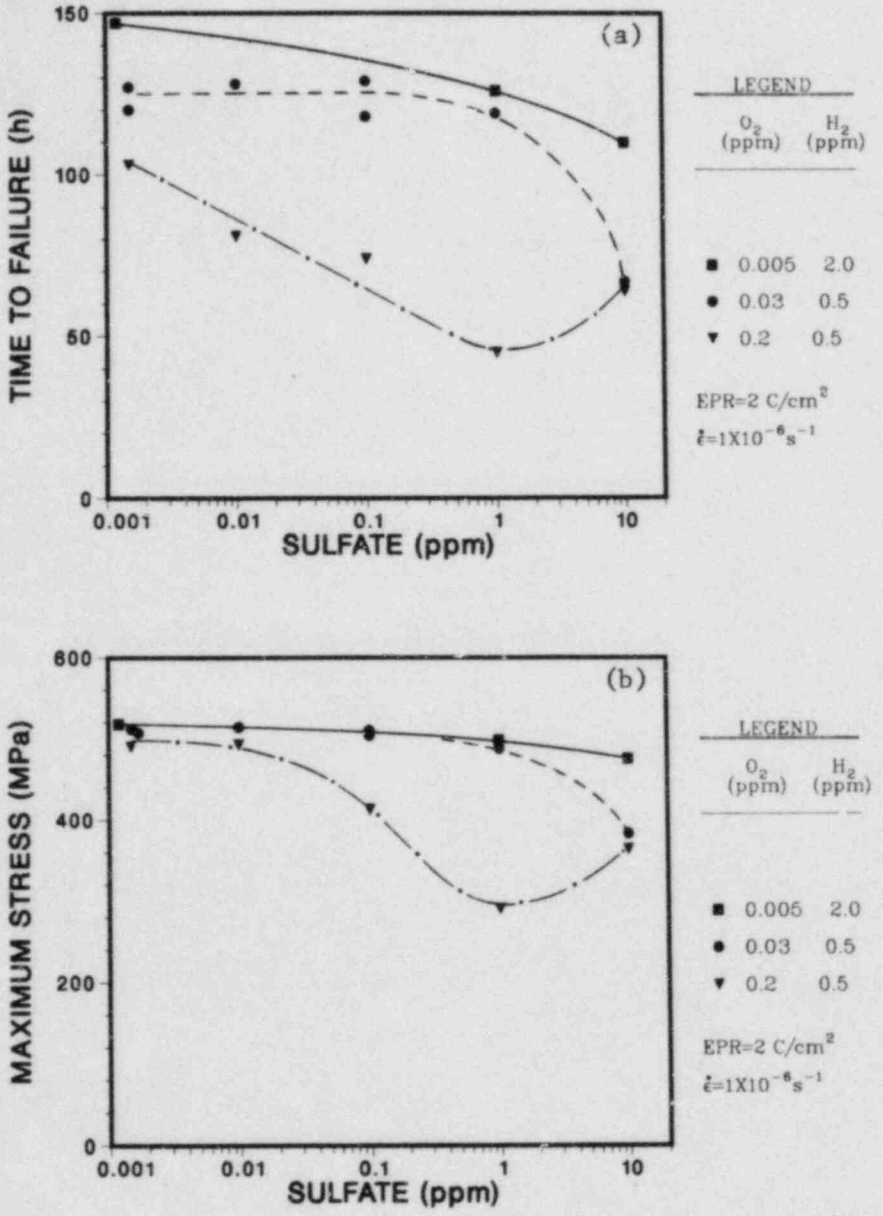

Fig. 1.13. Influence of ~0.005, 0.03, and 0.2 ppm Dissolved Oxygen with 0.5 and 2.0 ppm Hydrogen at Several Sulfate Concentrations in 289°C Water on (a) Time to Failure and (b) Maximum Stress of Lightly Sensitized (EPR = 2 C/cm^2) Type 304 SS Specimens. Data points at a sulfate concentration of 0.001 ppm represent high-purity water in which no sulfate was added to the feedwater.

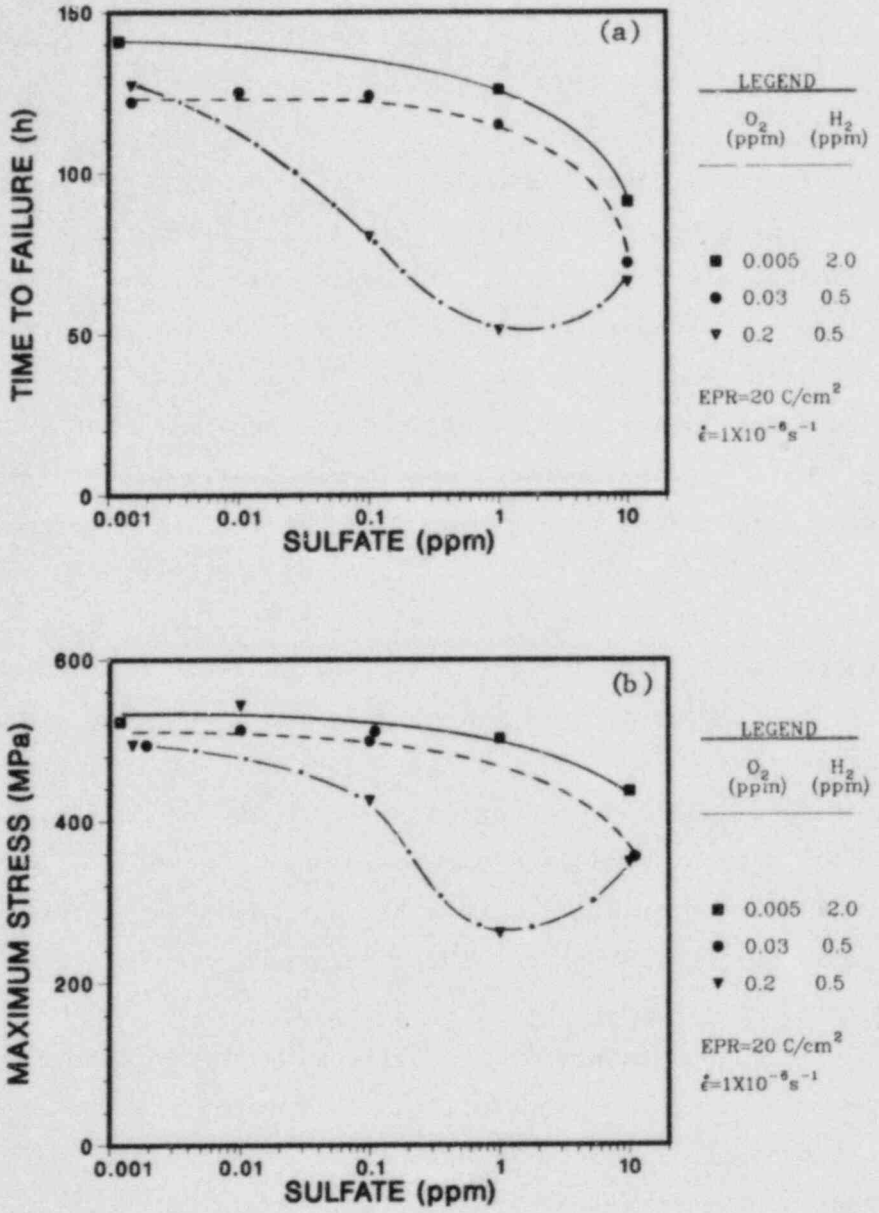

Fig. 1.14. Influence of ~0.005, 0.03, and 0.2 ppm Dissolved Oxygen with 0.5 and 2.0 ppm Hydrogen at Several Sulfate Concentrations in 289°C Water on (a) Time to Failure and (b) Maximum Stress of Moderately Sensitized (EPR = 20 C/cm^2) Type 304 SS Specimens. Data points at a sulfate concentration of 0.001 ppm represent high-purity water in which no sulfate was added to the feedwater.

Fig. 1.15 for different environments. Since a large change in the potentials was observed in low-oxygen environments after the autoclave temperature reached 289°C, straining of the specimens was initiated after ~20 h in all of the experiments to allow the corrosion and redox potentials to approach the steady-state values.

The relationship between the time to failure and the corr sion and redox potentials is shown in Figs. 1.16 and 1.17 for the lightly (EPR = 2 C/cm^2) and moderately (EPR = 20 C/cm^2) sensitized material, respectively. The symbols indicate whether the test environment contained sulfate and/or hydrogen as well as the fracture mode, i.e., ductile plus transgranular (open symbols) or ductile plus intergranular (closed symbols). For the purpose of constructing these figures, a fracture morphology with both transgranular and intergranular or granulated regions was considered to be intergranular. The information clearly indicates that IGSCC susceptibility extends to very negative potentials, and the corrosion or redox potential per se is not suffient to predict susceptibility to IGSCC in impurity environments. Since conductivity, rather than the concentration of specific impurities, is the common measure of water purity in BWRs, the time to failure of CERT specimens with both levels of sensitization was correlated with the conductivity of the water in Fig. 1.18. The importance of dissolved oxygen concentration (0.2 versus $\leq$0.03 ppm) on IGSCC susceptibility at conductivity values between ~0.2 and 10 µS/cm is also quite evident from these figures.

From the standpoint of delineating the influence of the high-temperature water on IGSCC susceptibility of Type 304 SS, the corrosion potential of the steel is primarily a function of the dissolved oxygen concentration whereas the conductivity is directly related to the concentration of ionic impurities in the water. The regime of corrosion potential and conductivity that yields immunity to IGSCC of Type 304 SS at 289°C, based upon the CERT results at a strain rate of 1×10^{-6} s^{-1}, is shown in Fig. 1.19. Similar plots in terms of the redox potential of the platinum electrode that was exposed to the environment during the CERT experiments are shown in Fig. 1.20. It is clear from the results that the sensitized steel is susceptible to IGSCC at 289°C in very pure water ($\lesssim$0.1 µS/cm) at corrosion potentials $\gtrsim$50 mV(SHE). Water purity is still an important factor in IGSCC at

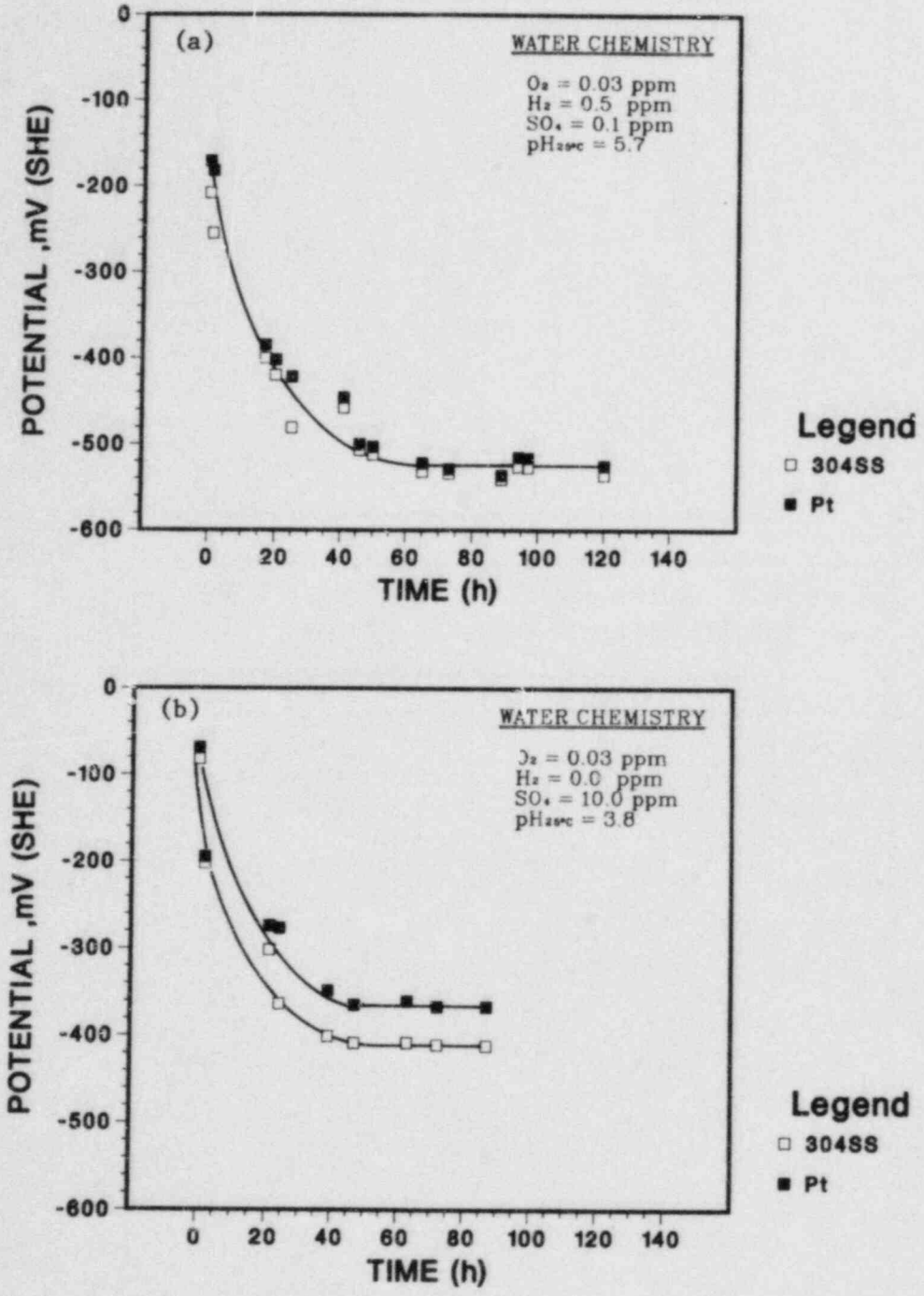

Fig. 1.15. Time-Dependence of the Electrochemical Potential of Type 304 SS and Platinum during CERT Experiments in 289°C Water Containing Dissolved Oxygen, Hydrogen, and Sulfate. Straining of the CERT specimen was initiated after ~20 h when the potentials approached the steady-state values.

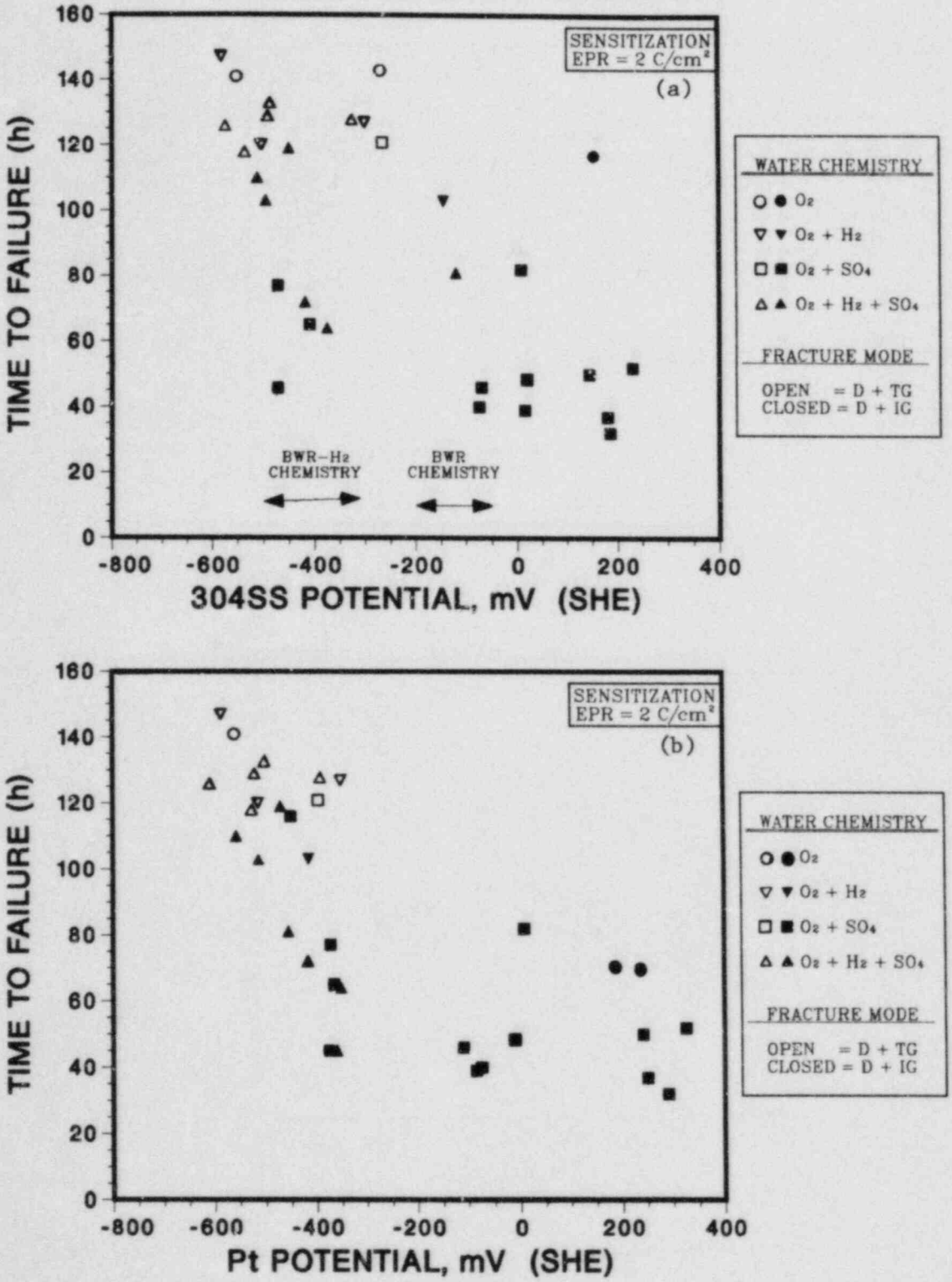

Fig. 1.16. Time to Failure of Lightly Sensitized (EPR = 2 C/cm^2) Type 304 SS Specimens in CERT Experiments at 289°C and a Strain Rate of 1 x 10^{-6} s^{-1} versus the Steady-State Potentials of (a) Type 304 SS and (b) Platinum Electrodes at 289°C in Simulated BWR Environments.

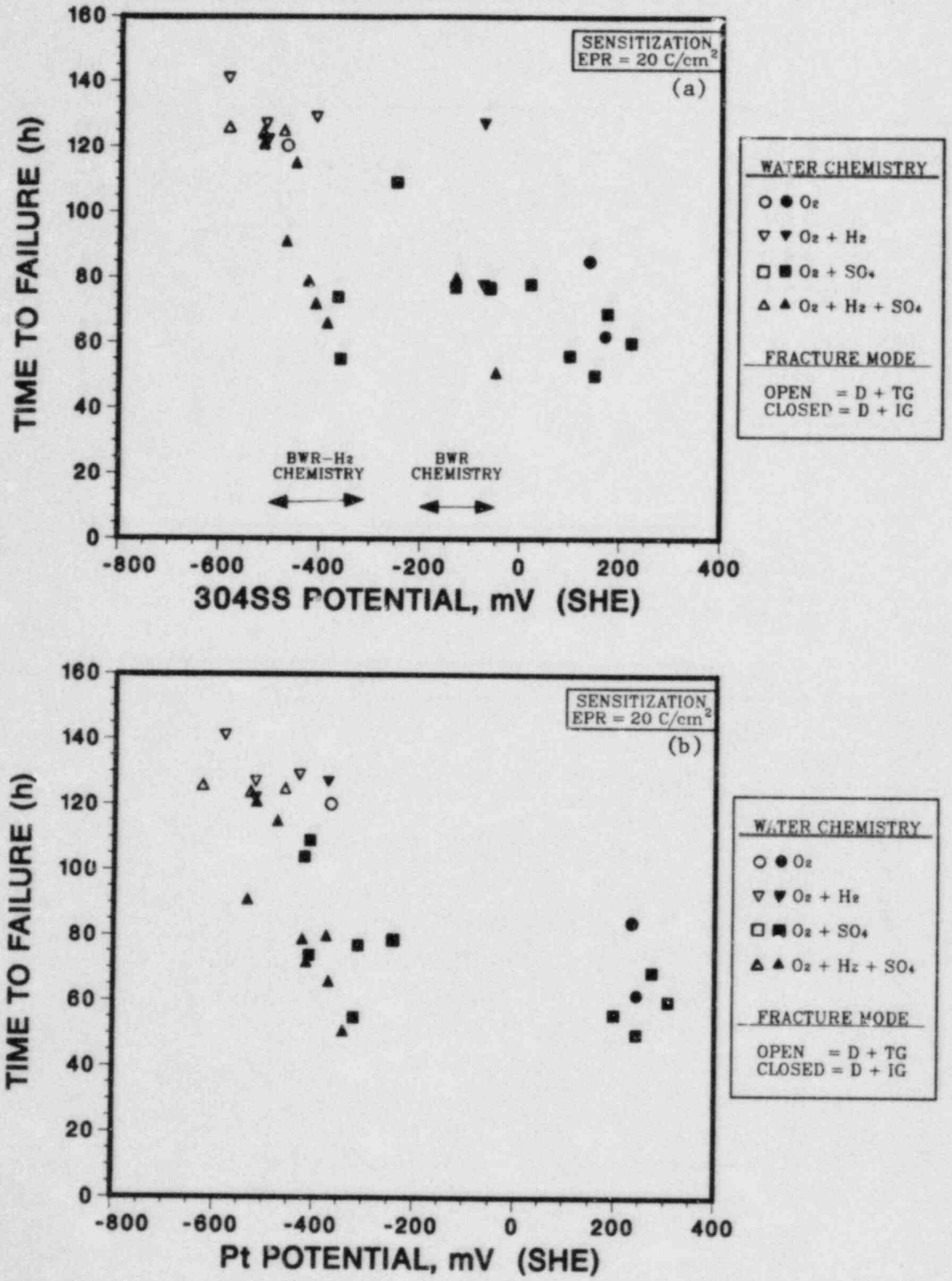

Fig. 1.17. Time to Failure of Moderately Sensitized (EPR = 20 C/cm^2) Type 304 SS Specimens in CERT Experiments at 289°C and a Strain Rate of 1 x 10^{-6} s^{-1} versus the Steady-State Potentials of (a) Type 304 SS and (b) Platinum Electrodes at 289°C in Simulated BWR Environments.

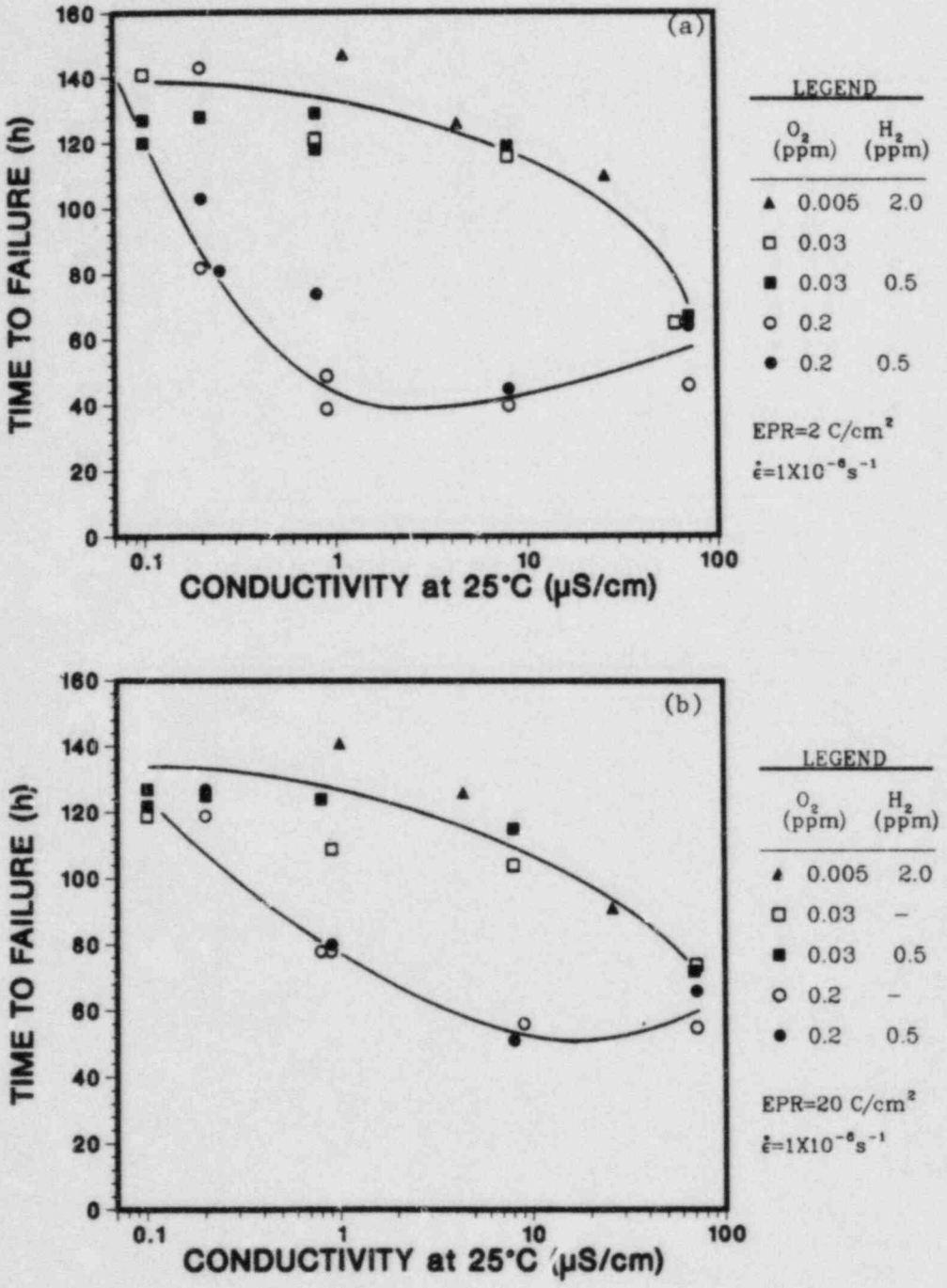

Fig. 1.18. Influence of Feedwater Conductivity on the Time to Failure of (a) Lightly (EPR = 2 C/cm^2) and (b) Moderately (EPR = 20 C/cm^2) Sensitized Type 304 SS in CERT Experiments at 289°C and a Strain Rate of 1 x 10^{-6} s^{-1} in Water Containing 0.2, 0.03, and 0.005 ppm Dissolved Oxygen Without (Open Symbols) and With (Closed Symbols) 0.5 or 2.0 ppm Hydrogen.

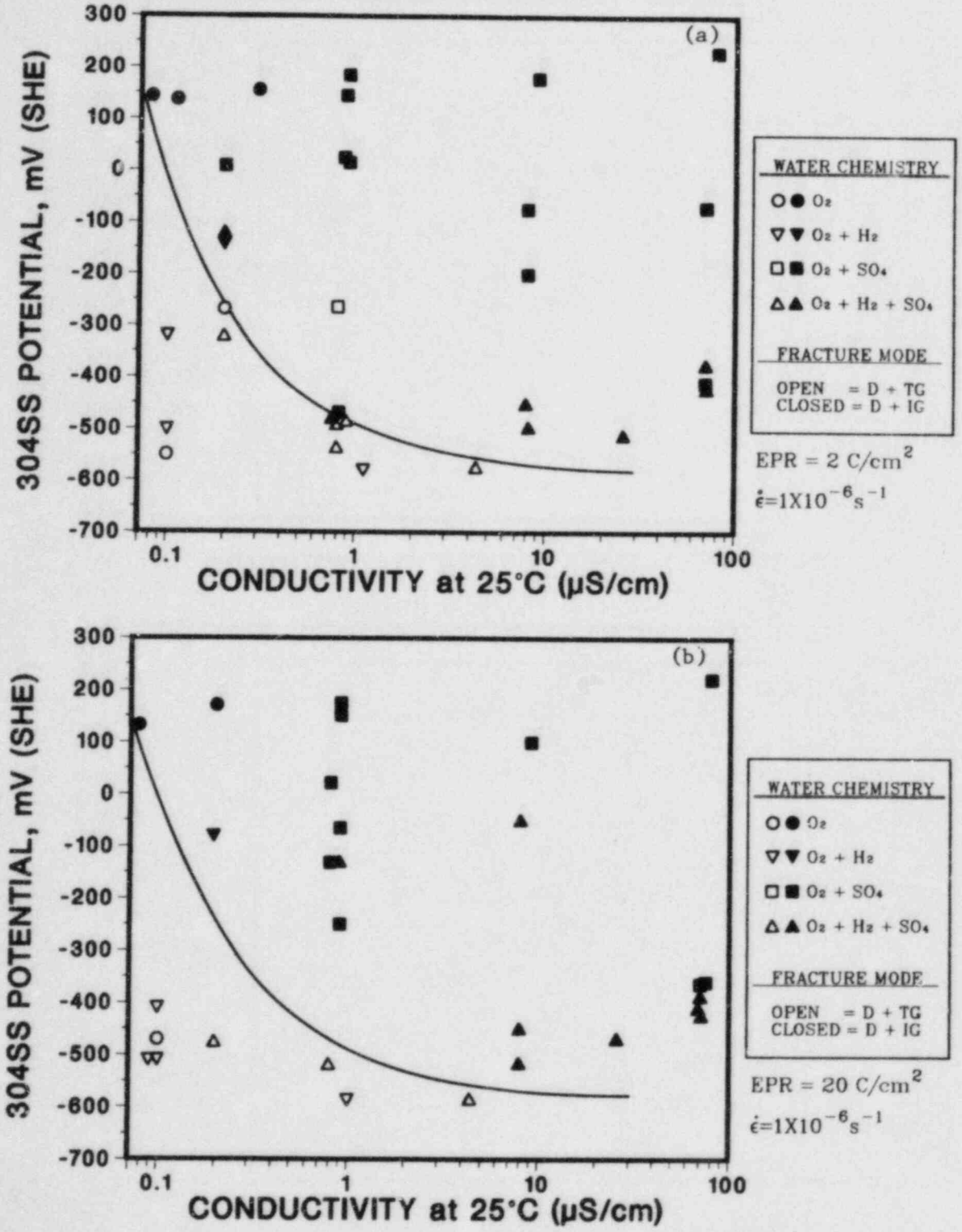

Fig. 1.19. Regime of Corrosion Potential and Feedwater Conductivity That Results in Immunity to IGSCC (Region Below Curve in Each Panel) for (a) Lightly (EPR = 2 C/cm^2) and (b) Moderately (EPR = 20 C/cm^2) Sensitized Type 304 SS in CERT Experiments at 289°C in Simulated BWR-Quality Water Containing Dissolved Oxygen, Hydrogen, and Sulfate as H_2SO_4. Open and closed symbols represent transgranular and intergranular fracture mode, respectively.

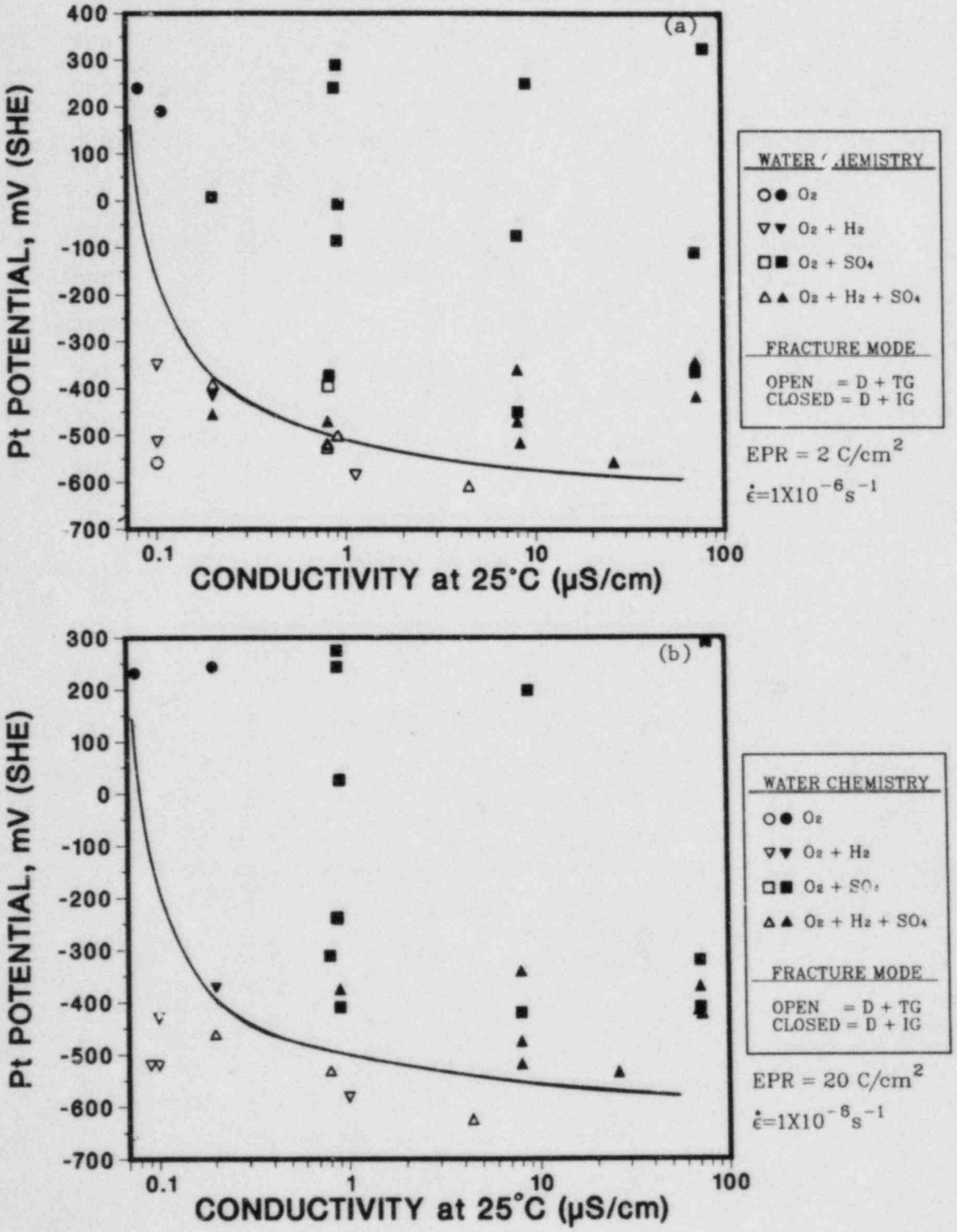

Fig. 1.20. Regime of Redox Potential and Feedwater Conductivity That Results in Immunity to IGSCC (Region Below Curve in Each Panel) for (a) Lightly (EPR = 2 C/cm^2) and (b) Moderately (EPR = 20 C/cm^2) Sensitized Type 304 SS in CERT Experiments at 289°C in Simulated BWR-Quality Water Containing Dissolved Oxygen, Hydrogen, and Sulfate as H_2SO_4. Open and closed symbols represent transgranular and intergranular fracture mode, respectively.

a corrosion potential of -350 mV(SHE), which was obtained during hydrogen addition to the feedwater of the Dresden-2 reactor.[22] Dissolved hydrogen in the recirculating-loop water suppressed the oxygen concentrations to $\lesssim$20 ppb, which decreased both the corrosion and redox potentials to approximately -350 and -600 mV(SHE), respectively, as shown in Fig. 1.21. The information in Fig. 1.19 indicates that the conductivity of the reactor coolant water would have to be maintained at $\lesssim$0.2 μS/cm to achieve immunity to IGSCC with the alternate hydrogen-water chemistry. The information in Fig. 1.20, which is based on redox potential measurements with a platinum electrode, suggests a somewhat larger conductivity margin for immunity to IGSCC. In general, the platinum electrode responds more rapidly to changes in the environment, and the steady-state corrosion and redox potentials differed by $\lesssim$50 mV in most of our CERT experiments at low dissolved oxygen concentrations. Consequently, it is possible that the steady-state corrosion potential of Type 304 SS in the Dresden-2 reactor during long-term operation with the hydrogen-water chemistry could be lower than the value shown in Fig. 1.21.

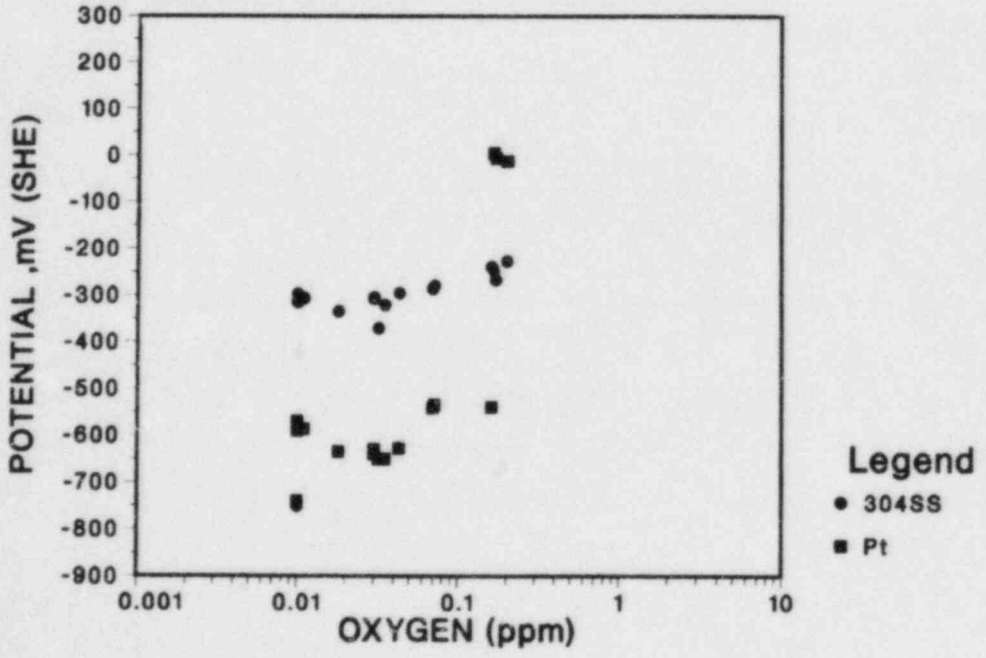

Fig. 1.21. Electrochemical Potentials of Type 304 SS and Platinum Electrodes at 273°C versus Dissolved Oxygen Concentration of Dresden-2 Reactor Water during the Oxygen Suppression Experiment,[22] in Which Hydrogen was Added to the Feedwater.

The influence of strain rate on susceptibility must also be considered[23,24] relative to the regime for immunity to IGSCC in Figs. 1.19 and 1.20. For a given temperature, material condition (degree of sensitization), and environment the deformation rate has the following effect on IGSCC susceptibility: At strain rates higher than $\sim 10^{-5}$ s^{-1}, electrochemical processes (viz., dissolution and repassivation) at the crack tip are eclipsed by the usual mechanical fracture processes and failure occurs at ductilities observed in air or inert gas environments. At very low strain rates that approach creep deformation, film rupture events at the crack tip may not occur or may be too infrequent to sustain a significant average dissolution rate. In this case, repassivation can more than keep up and normal fracture processes prevail; the result is relatively high ductility. As the environment becomes more benign at lower dissolved oxygen and impurity concentrations, the critical range of deformation rates that promotes the low-ductility SCC process, in general, decreases. The extent to which this may occur in simulated BWR-quality water at high temperature has not been established adequately. Consequently, several CERT experiments will be performed at strain rates of $\lesssim 10^{-6}$ s^{-1} to quantify the influence of deformation rate on the transition from intergranular to transgranular failure for conditions of low conductivity and corrosion or redox potential as depicted in Figs. 1.19 and 1.20.

b. Crack Growth Results on Type 304 SS in Simulated BWR-Quality Water at 289°C

Fracture-mechanics-type crack-growth tests are in progress on the same heat of material as in the CERT experiments. Two ITCT specimens of the steel (designated 10 and 11) were sensitized to an EPR value of 20 C/cm^2, fatigue precracked in air at 289°C (to avoid the long period for crack initiation observed in a previous experiment), and stressed in high-purity water with 8 ppm dissolved oxygen at an initial K_{max}, frequency, and R value of 34-35 $MPa \cdot m^{1/2}$, 8 x 10^{-2} Hz, and 0.95, respectively. The crack growth rates from the initial phase of the experiment are given in Table 1.6 along with previously reported results.[25] When K_{max} was increased in subsequent phases of the experiment, the crack growth rates decreased; this suggests that multiple cracks may have formed in the specimens. Consequently, the experiment was terminated at an apparent K_{max} of 60 $MPa \cdot m^{1/2}$ based on a single

TABLE 1.6. Crack Growth Rate Results on Sensitized (EPR = 20 C/cm^2) Type 304 SS in High-Purity Water with 8 ppm Dissolved Oxygen at 289°C and an R Value of 0.95

Specimen[a] No.	Loading Time, s	Frequency,[b] Hz	K_{max}, MPa·m$^{1/2}$	Crack Growth Rate		
				m·s^{-1}	mm·h^{-1}	mm·yr^{-1}
2	12	8×10^{-2}	28	7.5×10^{-10}	2.7×10^{-3}	23.6
10	12	8×10^{-2}	34	1.0×10^{-9}	3.7×10^{-3}	32.4
11	12	8×10^{-2}	35	1.2×10^{-9}	4.3×10^{-3}	37.6
2	126	8×10^{-3}	34	1.2×10^{-10}	4.7×10^{-4}	3.7
↓	126	8×10^{-3}	38	1.5×10^{-10}	5.6×10^{-4}	4.9
	126	8×10^{-3}	50	4.7×10^{-10}	1.7×10^{-3}	14.7
	126	8×10^{-3}	61	1.1×10^{-9}	3.9×10^{-3}	34.4
	126	8×10^{-3}	64	1.7×10^{-9}	6.0×10^{-3}	53.0
2	1260	8×10^{-4}	28	1.2×10^{-10}	4.3×10^{-4}	3.8
↓	1260	8×10^{-4}	67	1.9×10^{-9}	6.8×10^{-3}	59.5
	1260	8×10^{-4}	70	3.2×10^{-9}	1.1×10^{-2}	100.0
	1260	8×10^{-4}	72	3.3×10^{-9}	1.3×10^{-2}	104.0

[a]Compact tension specimens (1TCT) from heat number 30956 were sensitized at 700°C for 12 h.
[b]Frequency of the positive sawtooth waveform is based primarily on the loading time, since the load decrease occurs within ~1 s.

crack, and the specimens were sectioned to determine the crack morphology. As shown in Fig. 1.22, macroscopic crack branching occurred in both specimens, i.e., two cracks formed from a single source early in the experiment and grew at an acute angle to each other at approximately the same velocity. Microbranches, i.e., small side cracks which arrest after being outrun by the main crack, as well as macrobranches can produce a plateau region (or even a decrease in the crack velocity) in a logarithmic plot of crack velocity versus stress intensity factor.[26-28] This type of plot is shown in Fig. 1.23 for the moderately sensitized steel in high-purity water with 8 ppm oxygen at 289°C (Table 1.5). A plateau region was not observed in the curves at the lower frequencies for stress intensity factors up to ~60-70 MPa·m$^{1/2}$. Occasionally, single cracks can propagate over a range of stress intensities where crack branching is frequently encountered. To obtain reliable measurements of crack growth by compliance techniques and to calculate meaningful stress intensity values, it is essential to avoid macroscopic crack branching. This was

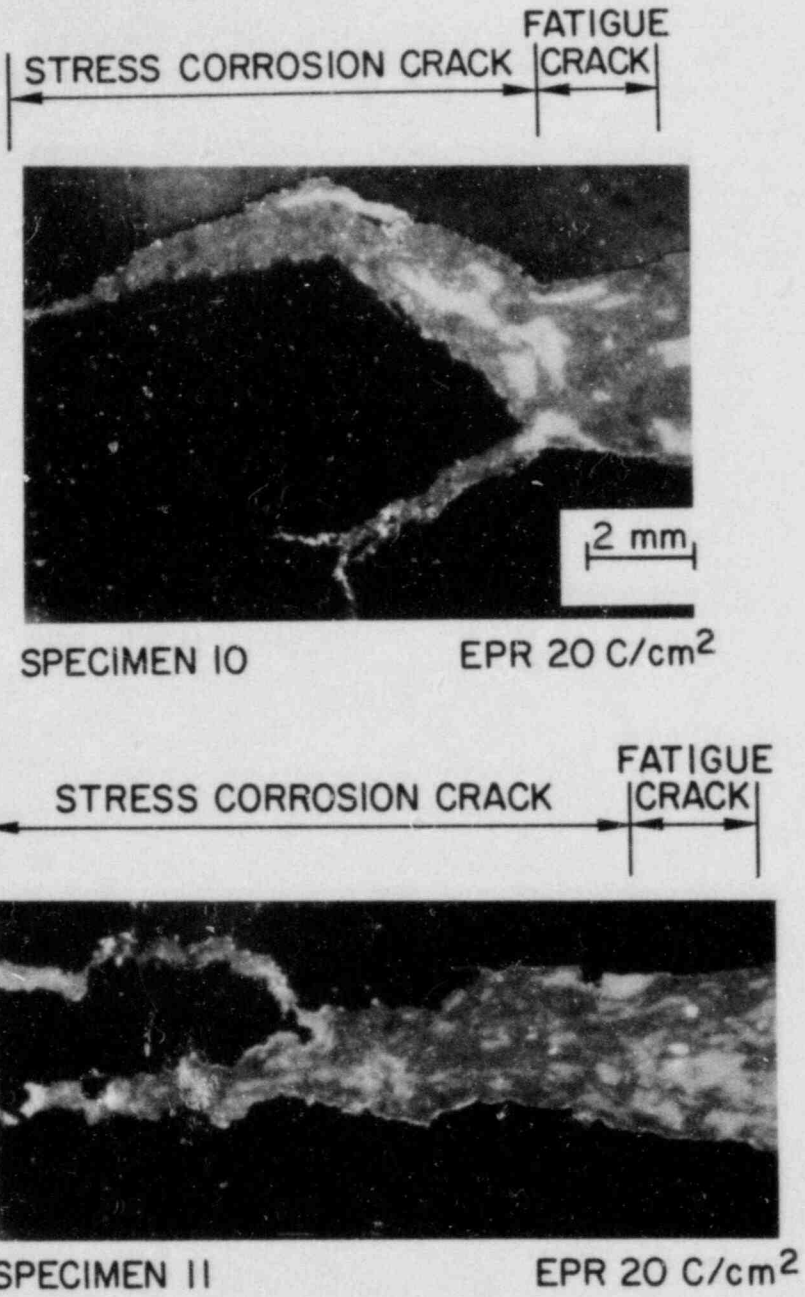

Fig. 1.22. Micrographs of Cross Sections of 1TCT Specimens of Sensitized (EPR = 20 C/cm^2) Type 304 SS from a Crack Growth Experiment at 289°C in High-Purity Water with 8 ppm Dissolved Oxygen. Branching of the stress corrosion cracks occurred early in the experiment (initial K_{max} = 35 $MPa \cdot m^{1/2}$); this caused the apparent crack growth rate (based on compliance measurements of crack length) to decrease as the stress intensity increased during subsequent phases of the test.

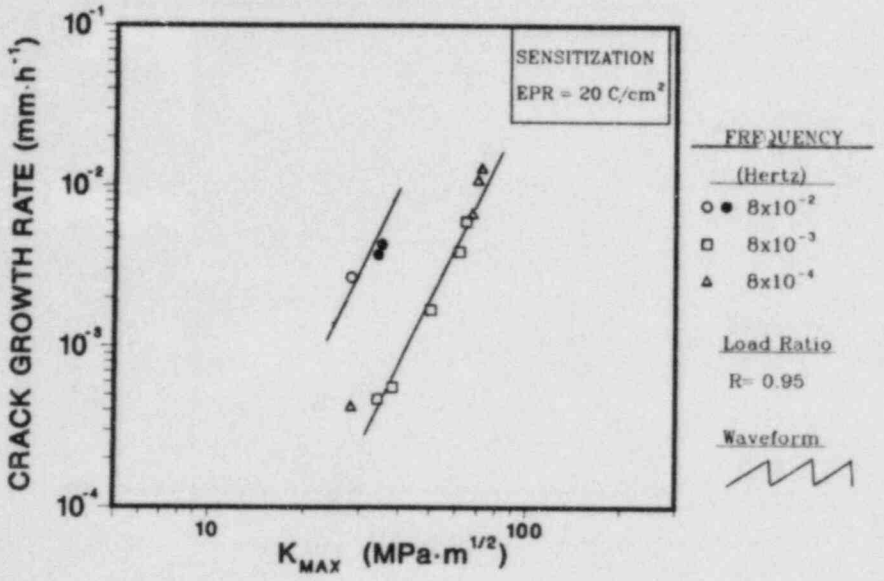

Fig. 1.23. Dependence of Crack Growth Rate on Stress Intensity Factor, K_{max}, for Moderately Sensitized (EPR = 20 C/cm^2) Type 304 SS in High-Purity Water with 8 ppm Dissolved Oxygen at 289°C. Steady-state crack growth rates were obtained at an R value of 0.95 with a positive sawtooth waveform, in which the frequency was determined by the slow loading time.

achieved in the first experiment by applying a lower initial stress intensity (K_{max} = 28 MPa·m$^{1/2}$), and possibly by initiating the crack in the high-temperature water environment.

Another experiment is in progress to investigate the effect of impurities, viz., H_2SO_4 from decomposition of ion exchange resins, on the cyclic crack-growth properties of the steel at 289°C. Instrumented ITCT specimens with EPR values of 0, 2, and 20 C/cm^2 were fatigue precracked in air at 289°C to provide 3-mm-deep starter cracks, and the specimens are being tested in water containing 0.2 ppm dissolved oxygen and 0.1 ppm sulfate (as H_2SO_4). The initial results in Fig. 1.24 were obtained under a positive-sawtooth-waveform, high-R (0.95) loading at a K_{max} of 28 MPa·m$^{1/2}$ and a frequency of 8 x 10^{-2} Hz. In contrast to results obtained in high-purity water with 8 ppm dissolved oxygen, the lightly sensitized specimen (EPR = 2 C/cm^2) exhibits the highest crack growth rate (3.6 x 10^{-4} mm/h) in the impurity environment, which is consistent with the relative susceptibilities of specimens with the two levels of sensitization in CERT experiments in these environments.

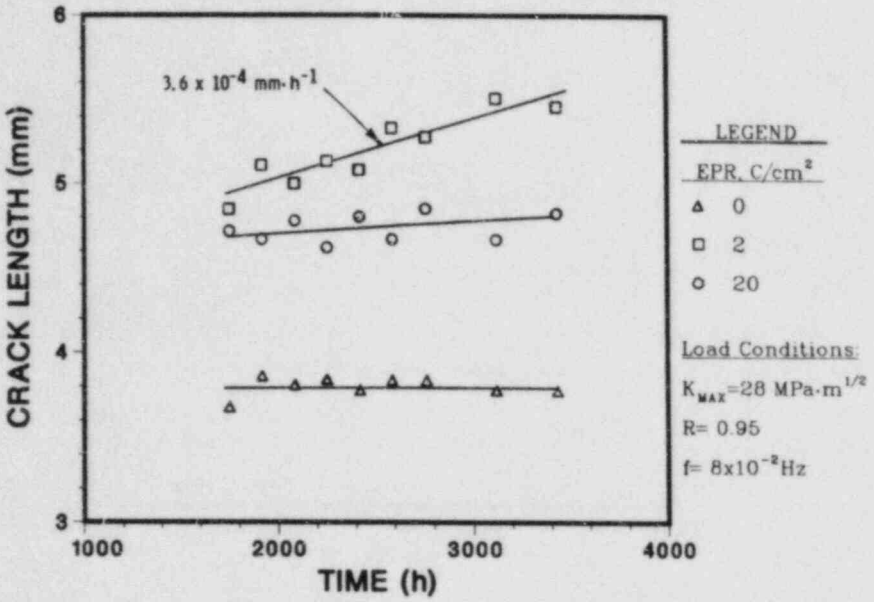

Fig. 1.24. Crack Length versus Time for 1TCT Specimens of Solution-annealed (EPR = 0) and Sensitized (EPR = 2 and 20 C/cm^2) Type 304 SS in 289°C Water Containing 0.2 ppm Dissolved Oxygen and 0.1 ppm Sulfate as H_2SO_4. The loading conditions for the positive sawtooth waveform with a slow loading time (12 s) and rapid unloading (1 s) are as follows: stress ratio R = 0.95, K_{max} = 28 MPa·m$^{1/2}$, and frequency = 8 x 10^{-2} Hz.

c. Determination of pH of Dilute H_2SO_4, NaOH, and H_2SO_4/Na_2SO_4 Solutions at 289°C

The pH of dilute H_2SO_4, NaOH, and H_2SO_4/Na_2SO_4 solutions at 289°C and 8.3 MPa pressure was experimentally determined by means of a solid-electrolyte sensor (ZrO_2-16.9% Y_2O_3 with a Cu/Cu_2O internal reference) and a 0.1M KCl/AgCl/Ag external reference electrode. The dissolved oxygen concentration at the inlet of the refreshed 1.8-liter titanium autoclave was maintained at 0.15 to 0.32 ppm. The pH of the feedwater was varied by incremental changes in the H_2SO_4 and NaOH concentrations as well as the molar ratio of H_2SO_4/Na_2SO_4 at a constant sulfate concentration of 100 ppm.

The experimental $pH_{(289°C)}$ values were obtained from the measured cell potentials by means of the following expressions. The emf, in volts, of the oxygen-ion conducting electrode with respect to the SHE is given by the relation[29-31]

$$E_{\phi/SHE}(T) = E^{\circ}_{Cu_2O/Cu}(T) - \frac{2.303\ RT}{F} \cdot pH; \qquad (1.8)$$

at 289°C,

$$E_{\phi/SHE}(289°C) = 0.365 - 0.1113 \cdot pH. \qquad (1.9)$$

The response of the external Ag/AgCl reference electrode versus SHE, $E_{Ref(25°C)/SHE(T)}$, has been correlated by a third-order polynomial relation as a function of temperature (T - 25°C) and KCl electrolyte concentration.[32] At 289°C,

$$E_{Ref(25°C)/SHE(289°C)} = -0.022\ V. \qquad (1.10)$$

The measured pH cell potentials are expressed as

$$E_{\phi/Ref} = E_{\phi/SHE} - E_{Ref/SHE}, \qquad (1.11)$$

and the pH at 289°C can be determined by substituting Eqs. (1.9) and (1.10) into (1.11), which yields

$$pH_{(289°C)} = \frac{0.387 - E_{\phi/Ref}}{0.1113}. \qquad (1.12)$$

Cell potentials for various H_2SO_4 and NaOH solutions and high-purity water are given in Table 1.7; also shown are calculated 289°C pH values based on the second dissociation constant of the bisulfate ion reported in Ref. 34 ("Case 2"). In Fig. 1.25, the measured potentials for these solutions are compared with the theoretical response of the pH sensor as a function of pH at 289°C.

Table 1.8 provides experimental feedwater chemistry data (sulfate concentration, molar ratio, dissolved oxygen, pH, and conductivity at 25°C) for a series of H_2SO_4/Na_2SO_4 solutions, and 289°C pH values determined from Eq. (1.12) and calculated on the basis of both the Case 2 constant and the corresponding constant reported in Ref. 33 ("Case 1"). Both sets of calculated 289°C pH values agree well with the experimentally determined

TABLE 1.7. Measured and Calculated Potentials for a Solid-Electrolyte pH Sensor in High-Purity Water and Dilute H_2SO_4 and NaOH Solutions at 289°C

Test No.	Feedwater Chemistry: Oxygen, ppm	H_2SO_4, ppm	NaOH, ppm	pH at 25°C: Meas.	pH at 25°C: Calc.	Calculated pH at 289°C (Case 2)[a]	$E_{\phi/Ref}$, V: Meas.[b]	$E_{\phi/Ref}$, V: Calc.[c]
4	0.20	0	0	6.44	7.00	5.59	-0.235	-0.235
	0.15	0	0	6.03	7.00	5.59	-0.258	-0.235
	0.08	0	0	6.31	7.00	5.59	-0.243	-0.235
4	0.15	2.3	0	4.32	4.30	4.61	-0.139	-0.126
	-	46.9	0	3.01	3.06	3.34	-0.023	+0.015
	0.20	57.7	0	2.92	2.98	3.26	-0.052	+0.024
4	0.20	0	2.25	9.70	9.75	7.02	-0.414	-0.394
	0.20	0	20.0	10.73	10.70	7.97	-0.511	-0.500
5	0.20	0	0	6.60	7.00	5.59	-0.228	-0.235
	0.10	0	0	6.73	7.00	5.59	-0.237	-0.235
	0.06	0	0	6.20	7.00	5.59	-0.256	-0.235
5	0.02	42.8	0	3.05	3.10	3.38	+0.006	+0.011
	0.03	0	5.7	10.10	10.15	7.41	-0.431	-0.438
	0.01	0	10.8	10.45	10.43	7.70	-0.476	-0.470

[a]Based on the second dissociation constant for the bisulfate ion at high temperature given in Ref. 34.
[b]Potential of the yttria-stabilized ZrO_2 solid electrolyte pH sensor (with a Cu/Cu_2O internal reference) at 289°C versus a 0.1M KCl/AgCl/Ag external reference at 25°C.
[c]Calculated from "Case 2" pH values by use of Eq. (1.12).

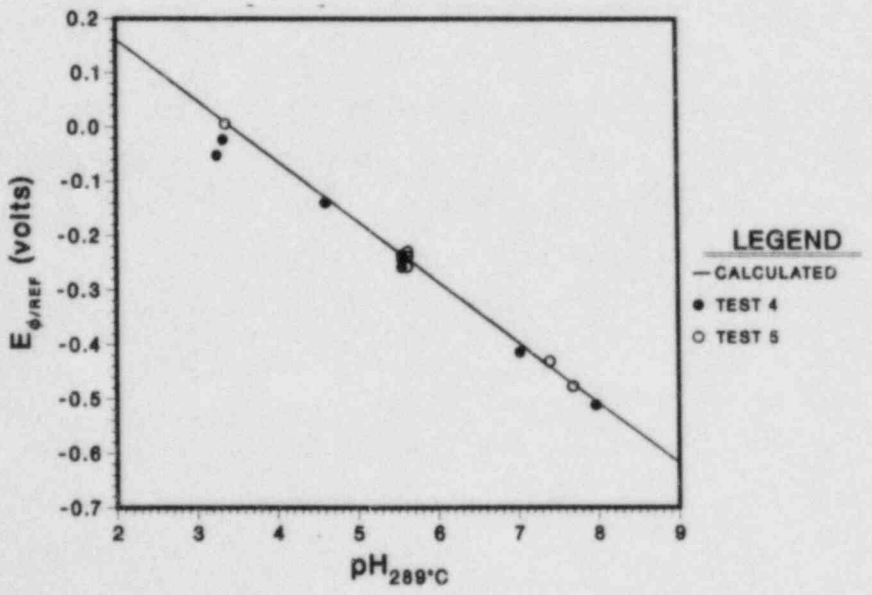

Fig. 1.25. Potential of Yttria-stabilized Zirconia Solid-Electrolyte Sensor (with a Cu/Cu_2O Internal Reference) at 289°C, with Respect to a 0.1M KCl/AgCl/Ag External Reference Electrode, as a Function of pH of Deaerated Water at 289°C. The line denotes the theoretical response of the sensor and the symbols represent measured values for various O_2, H_2SO_4, and NaOH concentrations (see Table 1.7).

TABLE 1.8. Experimentally Determined and Calculated pH of Dilute H_2SO_4/Na_2SO_4 Solutions at 289°C

Test No.	Feedwater Chemistry							pH at 289°C		
	Oxygen, ppm	SO_4^{2-}, ppm	Molar Ratio[a]	Cond., µS/cm		pH at 25°C		Exp.[b]	Calc. (Case 1)[c]	Calc. (Case 2)[d]
				Meas.	Calc.	Meas.	Calc.			
1	0.25	0	-	$\leq$0.2	~0.1	6.40	7.00	5.74	5.59	5.59
2	0.15	1	0	2.4	2.8	6.80	7.00	6.17	5.83	5.99
3	0.23	10	0	25	27	6.60	7.00	6.61	6.27	6.55
4	0.20	100	0	280	270	6.30	7.00	7.00	6.70	7.03
5	0.15	100	0.28	425	407	3.42	3.39	6.06	5.43	6.08
6	0.20	100	0.5	480	478	3.25	3.24	5.70	5.03	5.68
7	0.20	100	1.0	540	582	3.10	3.06	4.60	4.19	4.52
8	0.32	100	2.0	640	686	2.95	2.92	3.90	3.49	3.51
9	0.25	100	10.0	775	837	2.85	2.80	3.67	3.12	3.12

[a]Molar ratio of H_2SO_4/Na_2SO_4.
[b]Determined from Eq. (1.12).
[c]Based on the second dissociation constant for the bisulfate ion at high temperature given in Ref. 33.
[d]Based on the second dissociation constant for the bisulfate ion at high temperature given in Ref. 34.

values. Table 1.9 and Figs. 1.26 and 1.27 depict the difference between the calculated and experimentally determined pH values, and the difference between the calculated and experimentally determined pH changes that arise from successive changes in the feedwater chemistry for the nine test conditions in Table 1.8 over a total time period of ~300 h. As indicated previously, the response of the pH sensor is quite satisfactory in terms of both the absolute pH reading (Fig. 1.26) and incremental changes in the pH values (Fig. 1.27) based upon both methods for calculating the high-temperature pH of the solutions.

In Case 1 the pH values for aqueous solutions containing sulfuric acid and sodium sulfate were calculated by solving for the hydronium ion concentration in the expression

$$[H^+]^3 + [H^+]^2 (Q_2 + B - A) - [H^+] (Q_w + 2AQ_2) - Q_wQ_2 = 0, \qquad (1.13)$$

where A and B are the molal concentrations of H_2SO_4 and Na_2SO_4, respectively. From a study of the self-dissociation of water in KCl solutions from 0 to 300°C,[35] the equilibrium constant of water, K_w, and reaction quotient, Q_w, can be determined as a function of temperature, pressure, and ionic strength where

$$K_w = (a_{H^+})(a_{OH^-}) = [H^+][OH^-]\ \gamma^2_{\pm H_2O} \qquad (1.14)$$

and

$$Q_w = [H^+][OH^-]. \qquad (1.15)$$

The solution pH is expressed by

$$pH = -\log ([H^+]\ \gamma_{\pm}), \qquad (1.16)$$

where the mean activity coefficient $\gamma_{\pm} = (K_w/Q_w)^{1/2}$.

TABLE 1.9. Comparison of Experimentally Determined and Calculated pH Values at 289°C for Dilute H_2SO_4/Na_2SO_4 Solutions, and of Experimentally Determined and Calculated Incremental Changes in Successive Tests

Test[a] No.	pH at 289°C			pH Difference (Calc. - Exp.)		ΔpH[c] at 289°C			ΔpH Difference[d] (Calc. - Exp.)	
	Exp.	Calculated[b]				Exp.	Calculated			
		Case 1	Case 2	Case 1	Case 2		Case 1	Case 2	Case 1	Case 2
1	5.74	5.59	5.59	-0.15	-0.15	-	-	-	-	-
2	6.17	5.83	5.99	-0.34	-0.18	+0.43	+0.24	+0.40	-0.19	-0.03
3	6.61	6.27	6.55	-0.34	-0.06	+0.44	+0.44	+0.56	0	+0.12
4	7.00	6.70	7.03	-0.30	+0.03	+0.39	+0.43	+0.48	+0.04	+0.09
5	6.06	5.43	6.08	-0.63	+0.02	-0.94	-1.21	-0.95	-0.33	-0.01
6	5.70	5.03	5.68	-0.63	-0.02	-0.36	-0.40	-0.40	-0.04	-0.04
7	4.60	4.19	4.52	-0.41	-0.08	-1.10	-0.84	-1.16	+0.26	-0.06
8	3.90	3.49	3.51	-0.41	-0.39	-0.70	-0.70	-1.01	0	-0.31
9	3.67	3.12	3.12	-0.55	-0.55	-0.23	-0.37	-0.37	-0.14	-0.14

[a] Feedwater chemistry for these test conditions is given in Table 1.8.
[b] Based on the second dissociation constant for the bisulfate ion at high temperature given in Ref. 33 ("Case 1") or Ref. 34 ("Case 2").
[c] Incremental change in pH at 289°C that results from each successive change in feedwater chemistry: (pH for test 2 - pH for test 1), etc.
[d] Difference between calculated and experimental ΔpH values.

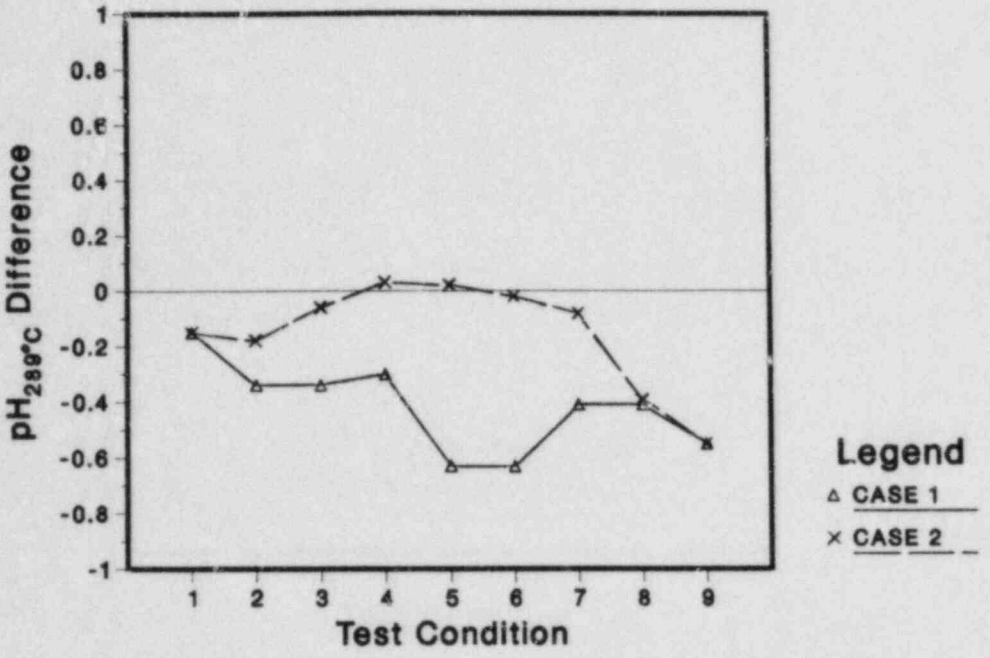

Fig. 1.26. Difference Between the Calculated and Experimentally Determined pH of H_2SO_4/Na_2SO_4 Solutions of Table 1.8 at 289°C, for Calculated pH Values Based on Two Different Values of the Second Dissociation Constant of HSO_4^- at High Temperature.

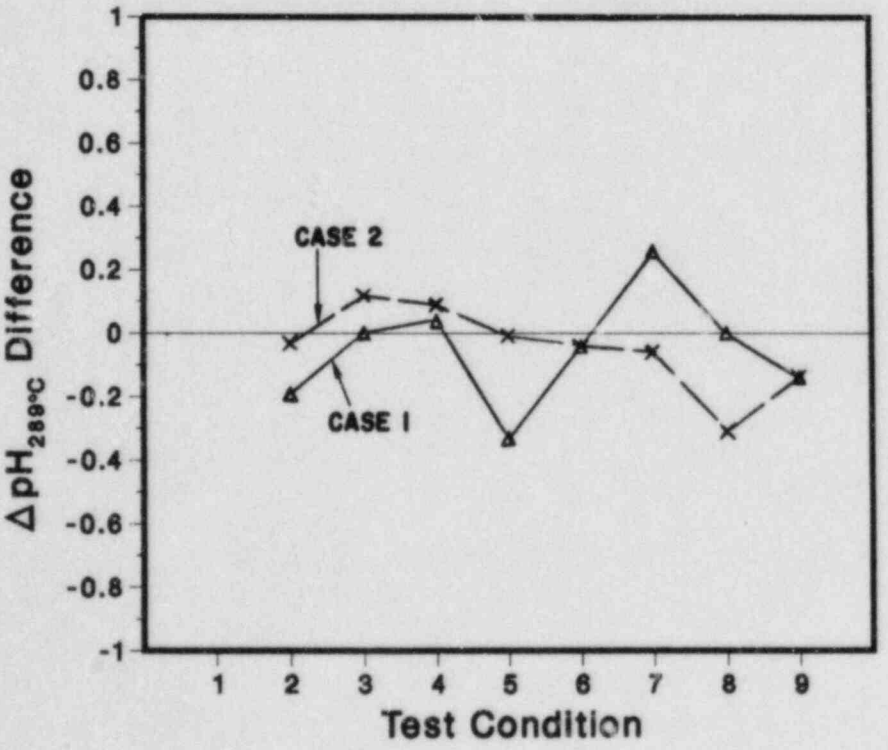

Fig. 1.27. Difference Between Calculated and Experimental ΔpH Values, as Defined in Table 1.9.

The second dissociation constant of sulfuric acid, K_2, and second concentration dissociation quotient, Q_2, used in Case 1 were evaluated over the range 25-350°C from studies of calcium sulfate solubility in sulfuric acid solutions of various ionic strengths.[33] The expression obtained for Q_2 as a function of ionic strength, I, and temperature is

$$\log Q_2(T) = \log K_2(T) + \frac{Z_+|Z_-|S_T\sqrt{I}}{1 + A_K(T)\sqrt{I}}, \qquad (1.17)$$

where S is the Debye-Huckel limiting slope, Z is the ion charge, and the A_K parameter was fitted from a least squares analysis.

However, there is some disagreement regarding the applicability of calcium sulfate solubility data in terms of the true equilibrium constants. Difficulties arise from ionic strength effects of 2:2 ($CaSO_4$) versus 1:2 (HSO_4^-) electrolytes at high temperature in that the bisulfate ion is much weaker.[34] In Case 2, alternative high-temperature values for K_2 were used in Eq. (1.17) that are based upon thermodynamic data, which assume constant heat capacity values for the ionic species and incorporate the Principle of Balance of Identical Like Charges.[34]

The relationships among sulfate concentration, pH at 25°C, and the calculated pH at 289°C for different molar ratios of H_2SO_4/Na_2SO_4 based on the input data in Cases 1 and 2 are shown in Figs. 1.28 and 1.29, respectively. In addition to the uncertainties in the calculated pH values at low sulfate concentrations ($\lesssim$100 ppm), some variability between the measured and calculated pH values at 289°C can be attributed to the long-term performance of the Ag/AgCl reference electrode. For example, drift in the potential of the reference electrode, due to dilution of the KCl solution from 0.1M to 0.01M near the end of the experiment (test conditions 8 and 9), can increase the measured pH values by ~0.32 pH units, and thus decrease the pH difference in Fig. 1.26 accordingly.

The present results indicate that the solid-electrolyte pH sensor, coupled with a stable Ag/AgCl external reference electrode, will be useful in evaluating the high-temperature pH of simulated BWR-quality water containing several ionic species (SO_4^{2-}, CO_3^{2-}, Cl^-, SiO_3^{2-}, etc.) during the crack growth experiments.

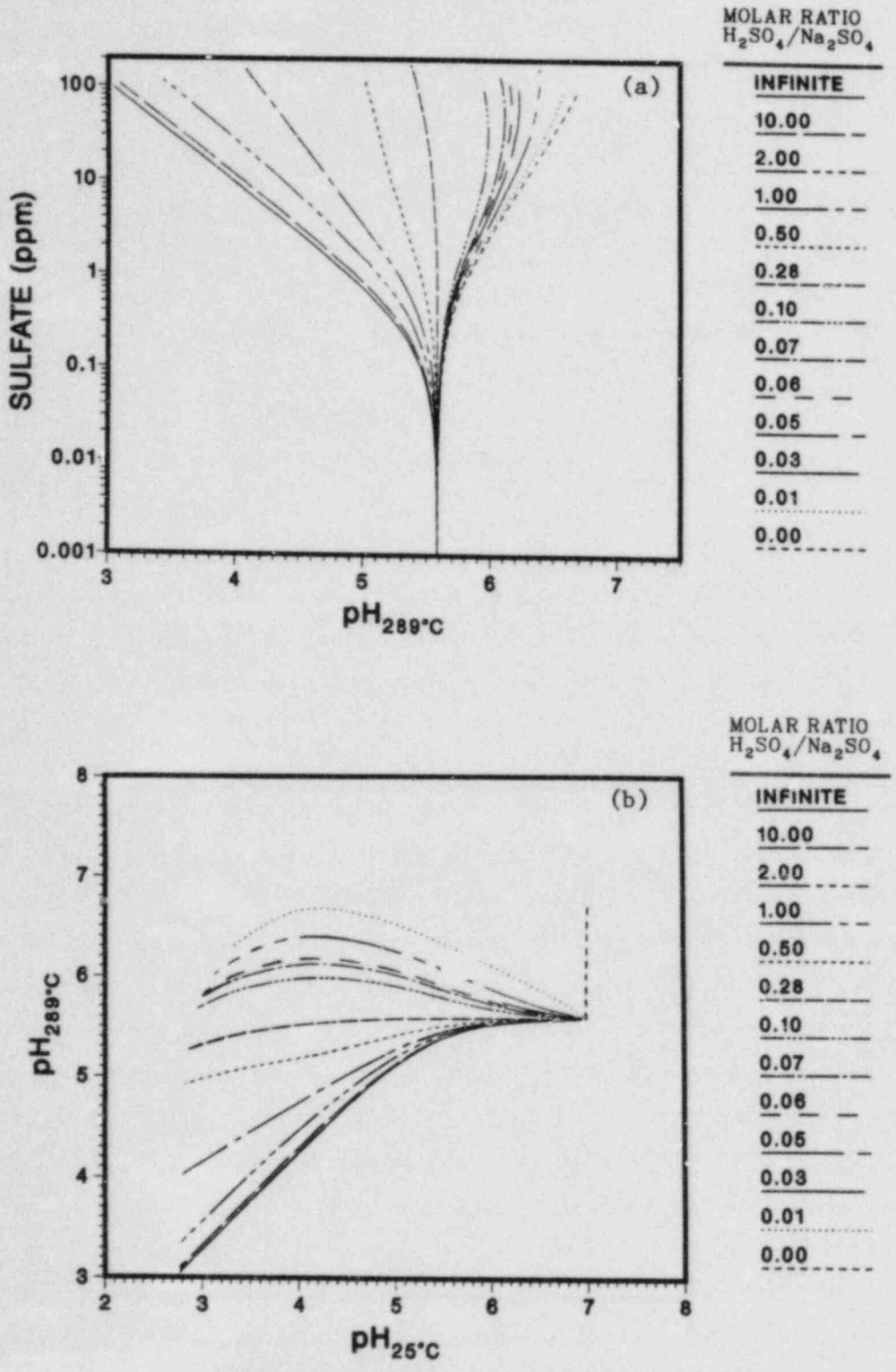

Fig. 1.28. Calculated pH at 289°C as a Function of (a) Sulfate Concentration and (b) pH at 25°C for Various Molar Ratios of H_2SO_4/Na_2SO_4, Based on Data for the Second Dissociation Constant of HSO_4^- in Ref. 33 (Case 1).

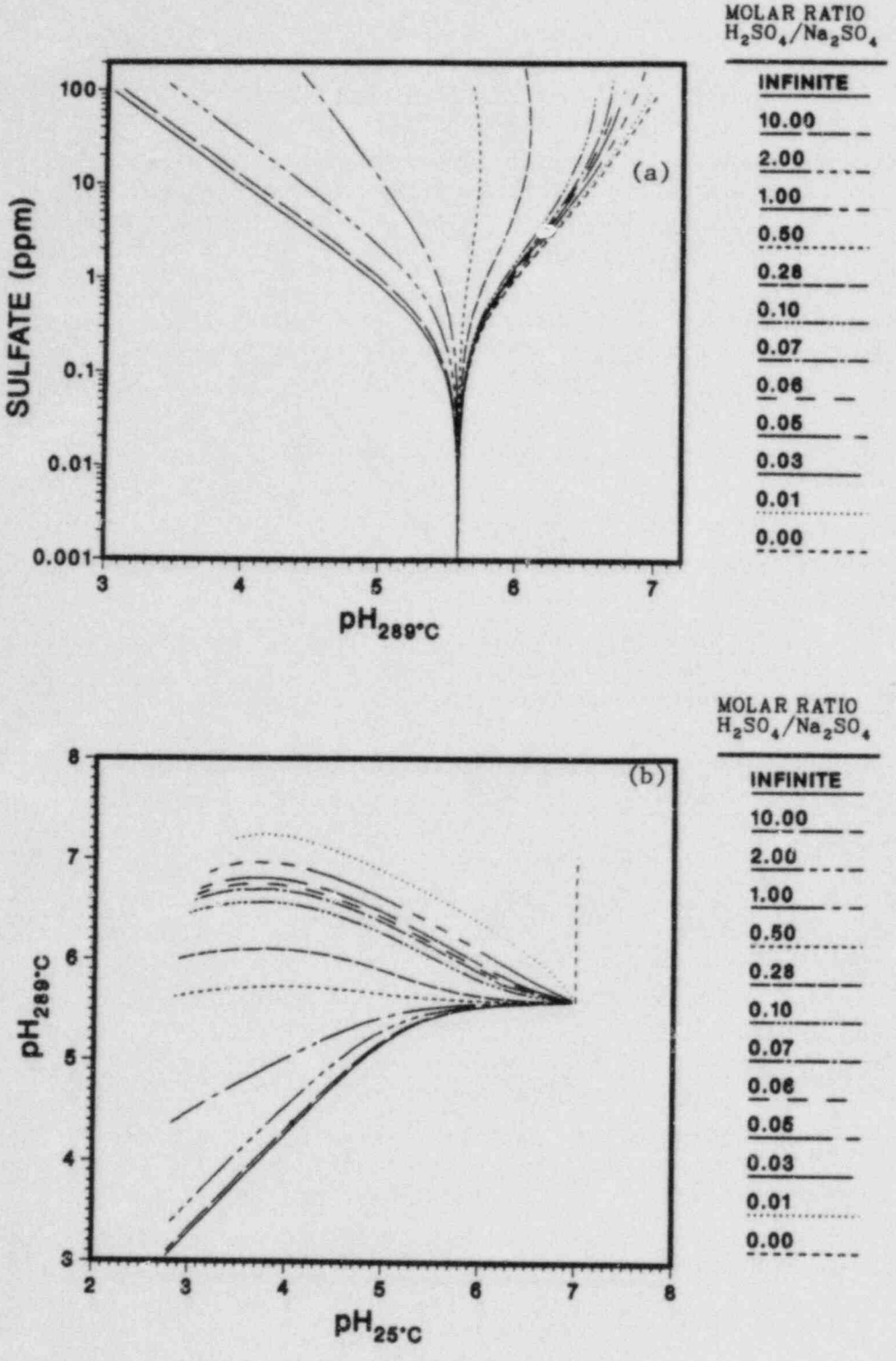

Fig. 1.29. Calculated pH at 289°C as a Function of (a) Sulfate Concentration and (b) pH at 25°C for Various Molar Ratios of H_2SO_4/Na_2SO_4, Based on Data for the Second Dissociation Constant of HSO_4^- in Ref. 34 (Case 2).

F. References for Chapter I

1. D. S. Kupperman, T. N. Claytor, and R. N. Lanham, in Materials Science and Technology Division Light-Water-Reactor Safety Research Program: Quarterly Progress Report, January-March 1983, NUREG/CR-3689 Vol. I, ANL-83-35 Vol. I (April 1984), pp. 2-23.

2. D. S. Kupperman, T. N. Claytor, D. Prine and R. Groenwald, "Analysis of Acoustic Leak Detection for Light Water Reactor Piping," in Periodic Inspection of Pressurized Components, IMechE Conference Publications 1989-9, Institution of Mechanical Engineers, London (October 1982), p. 45.

3. D. S. Kupperman, R. N. Lanham, T. N. Claytor, and R. Groenwald, in Environmentally Assisted Cracking in Light Water Reactors: Annual Report, October 1981-September 1982, NUREG/CR-3292, ANL-83-27 (February 1983), pp. 3-22.

4. P. Hutton, Battelle Pacific Northwest Laboratories, private communication.

5. R. F. Collier, Battelle Columbus Laboratories, private communication.

6. K. Fischer, Kraftwerk Union, Erlangen, W. Germany, private communication.

7. J. Y. Park, in Materials Science and Technology Division Light-Water-Reactor Safety Research Program: Quarterly Progress Report, January-March 1983, NUREG/CR-3689 Vol. I, ANL-83-35 Vol. I (April 1984), pp. 24-29.

8. J. Y. Park and W. J. Shack, in Materials Science and Technology Division Light-Water-Reactor Safety Research Program: Quarterly Progress Report, January-March 1983, NUREG/CR-3689 Vol. I, ANL-83-35 Vol. I (April 1984), pp. 30-33.

9. F. P. Ford, A Mechanism of Environmentally Controlled Crack-Growth of Structural Steels in High-Temperature Water, General Electric Co. Report 81-CRD-125 (August 1981).

10. P. M. Scott and A. E. Truswell, "Corrosion Fatigue Crack Growth in Reactor Pressure Vessel Steels in PWR Primary Water," in Aspects of Fracture Mechanics in Pressure Vessels and Piping, PVP Vol. 58, American Society of Mechanical Engineers, New York (1982), pp. 271-301.

11. J. R. Rice, "Mechanics of Crack Tip Deformation and Extension by Fatigue," in Fatigue Crack Propagation, ASTM STP 415, American Society for Testing and Materials, Philadelphia (1967), pp. 247-309.

12. P. S. Maiya and W. J. Shack, in Materials Science and Technology Division Light-Water-Reactor Safety Research Program: Quarterly Progress Report, January-March 1983, NUREG/CR-3689 Vol. I, ANL-83-35 Vol. I (April 1984), pp. 34-46.

13. P. S. Maiya and W. J. Shack, "Effects of Nominal and Crack-Tip Strain Rate on IGSCC Susceptibility in CERT Tests," to be presented at the Symposium on Localized Chemistry and Mechanics in Environmental-Assisted Fracture, TMS-AIME Fall Mtg., Philadelphia, PA, October 3-6, 1983.

14. P. S. Maiya, "Quantitative Description of Strain Rate Effects on Susceptibility to Intergranular Stress Corrosion Cracking," to be presented at the Sixth International Conference on Fracture, New Delhi, India, December 4-10, 1984.

15. F. P. Ford, "Mechanism of Stress Corrosion Cracking," in Aspects of Fracture Mechanics in Pressure Vessels and Piping, PVP Vol. 58, American Society of Mechanical Engineers, New York (1982), p. 229.

16. F. P. Ford, Mechanisms of Environmentally Enhanced Cracking in Systems Peculiar to the Power Generation Industry, EPRI NP-2589 (September 1982).

17. Hiroshi Takaku, Moriyasu Tokiwai, and Hideo Hirano, Effects of Cyclic Tensile Loading on Stress Corrosion Cracking Susceptibility for Sensitized Type 304 Stainless Steel in 290°C High Purity Water, Corrosion 35(11), 523 (1979).

18. P. S. Maiya and W. J. Shack in Environmentally Assisted Cracking in Light Water Reactors: Annual Report, October 1981-September 1982, NUREG/CR-3292, ANL-83-27 (February 1983), pp. 35-65.

19. E. W. Hart, Constitutive Relations for the Non-elastic Deformation of Metals, J. Eng. Mater. Technol. 93(3), 193 (1976).

20. W. E. Ruther, W. K. Soppet, and T. F. Kassner, in Materials Science and Technology Division Light-Water-Reactor Safety Research Program: Quarterly Progress Report, January-March 1983, NUREG/CR-3689 Vol. I, ANL-83-35 Vol. I (March 1984), pp. 47-59.

21. P. L. Andresen, Innovations in Experimental Techniques in Testing in High-Temperature Aqueous Environments, General Electric CRD Report 81-CRD-088 (May 1981).

22. E. L. Burley, Oxygen Suppression in Boiling Water Reactors - Phase 2 Final Report, General Electric Co. Report NEDC-23856-7, DOE/ET/34203-47 (October 1982).

23. J. Kruger, in Stress Corrosion Cracking, ed. J. Yohalom and A. Aladjem, Freurd Publishing House, Tel-Aviv, Israel (1980), p. 5.

24. F. A. Nichols, Mechanistic Aspects of Stress Corrosion Cracking of Type 304 Stainless Steel in LWR Systems, NUREG/CR-3220, ANL-83-15 (February 1983).

25. W. E. Ruther, W. K. Soppet, and T. F. Kassner, in Materials Science and Technology Division Light-Water-Reactor Safety Research Program: Quarterly Progress Report, October-December 1982, NUREG/CR-2970 Vol. IV, ANL-82-41 Vol. IV (November 1983), pp. 49-52.

26. M. O. Speidel, Stress Corrosion Crack Growth in Austenite Stainless Steel, Corrosion 33(6), 199-203 (1977).

27. F. P. Ford, "Stress Corrosion Cracking," in Corrosion Processes, ed. R. N. Parkins, Applied Science Publishers, London and New York (1982), p. 279.

28. M. O. Speidel, "Branching of Subcritical Cracks in Metals," in L'Hydrogene dans les Metaux, Editions Science et Industrie, Paris (1972) Vol. 2, pp. 358-362.

29. T. Tsuruta and D. D. Macdonald, Stabilized Ceramic Membrane Electrode for the Measurement of pH at Elevated Temperatures, J. Electrochem. Soc. 129(6), 1221-1225 (1982).

30. L. W. Niedrach, Use of a High Temperature pH Sensor as a 'Pseudo-Reference Electrode' in Monitoring of Corrosion and Redox Potentials at 285°C, J. Electrochem. Soc. 129(7), 1445-1449 (1982).

31. D. F. Taylor and C. A. Caramihas, "Crevice Corrosion in High-Temperature Aqueous Systems. Potential/pH Measurements in Alloy 600 Crevices at 288°C," in Proc. Symp. on High Temperature Materials Chemistry, D. D. Cubicciotti and D. L. Hildenbrand, eds., The Electrochemical Society, Denver, CO (1981), Vol. 82-1.

32. D. D. Macdonald, A. C. Scott, and P. Wentrcek, External Reference Electrodes for Use in High Temperature Aqueous Systems, J. Electrochem. Soc. 126(6), 908-911 (1979).

33. W. L. Marshall and E. V. Jones, Second Dissociation Constant of Sulfuric Acid from 25 to 350°C Evaluated from Solubilities of Calcium Sulfate in Sulfuric Acid Solutions, J. Phys. Chem. 70(12), 4028-4040 (1966).

34. J. W. Cobble, R. C. Murray, Jr., P. J. Turner, and K. Chen, High-Temperature Thermodynamic Data for Species in Aqueous Solution, EPRI Report NP-2400 (May 1982).

35. F. H. Sweeton, R. E. Mesmer, and C. F. Baes, Jr., Acidity Measurements at Elevated Temperature; VII. Dissociation of Water, J. Solution Chem. 3(3), 191-214 (1974).

II. TRANSIENT FUEL RESPONSE AND FISSION PRODUCT RELEASE

Principal Investigator:
J. Rest

A. Comparison of FASTGRASS Predictions for Fission Product Release Rate Constants with NUREG-0772 Results (J. Rest and M. Piasecka)

Rates of release of fission gas and volatile fission products from LWR fuel rods have been analyzed in order to compare the results presented in NUREG-0772[1] with the FASTGRASS code predictions. A series of experiments with highly irradiated fuel conducted in steam as well as dry air in the temperature range of 500 to 1600°C provided the data base for fission product release.

Fission product release occurs as a composite of many different mechanisms. Each of these mechanisms is dependent on many variables. The parameters controlling the rate of release of fission products include burnup, fuel grain size, temperature gradient, heating rate, and fuel temperature history.

In NUREG-0772, three sets of experiments (Lorenz et al., Parker et al., and Albrecht et al.) were selected to provide the data base for fission product release. The data from these experiments are expressed in terms of time and temperature by calculating a fractional release rate constant, k(T), defined as the fraction of remaining nuclide released per minute, i.e.,

$$k(T) = \frac{df}{dt} \tag{2.1}$$

where f = fraction of current inventory released, t = time (min), and T = fuel temperature.

For the experiments in which the release rate constant df/dt was not monitored continuously, the value of k is estimated as follows:

$$k(T) = \frac{-\ln (1 - F)}{t} \tag{2.2}$$

where F = fraction (of total amount generated) released during an isothermal test segment, and t = total test time (min).

For tests in which the temperature was changed incrementally and the fission product release monitored continuously, the release rate constant is calculated as

$$k(T) = \frac{\Delta f}{\Delta t} \qquad (2.3)$$

where Δf = fraction of current inventory released at temperature T, and Δt = increment of time for which Δf was measured (min). In all cases, the burst release amounts were not included in determining the release rate constants.

The theoretically based FASTGRASS[2,3] model was used for predicting fission gas and volatile fission product releases from LWR fuel subjected to ORNL-type transient conditions. Calculations were performed for 16 high-burnup transient tests (HBU,[4] HT,[5] and HI[6] series) performed at ORNL with 30.5-cm segments of fuel from the H. B. Robinson reactor. After a steady-state irradiation simulation, the temperatures were ramped to values of 500-1600°C and held for various lengths of time before test termination.

In Fig. 2.1, FASTGRASS predictions are plotted against experimentally measured values for fractional gas release. The diagonal line in this figure indicates perfect agreement between theory and experiment. In general, the agreement between theory and experiment is reasonable. A range of predicted values is shown for each of three tests in Fig. 2.1; this corresponds to reported[7] uncertainties in the fuel temperature during the test. The temperature uncertainties in these tests are attributed to the combined heat from rapid oxidation of cladding and higher levels of ohmic energy deposition.

Iodine, cesium, and noble gas release rate constants were measured in various tests;[4-6] the data are shown in Fig. 4.1 of Ref. 1. The corresponding release rate constants predicted by FASTGRASS for the HBU series of tests are a few orders of magnitude above these data; in general, the FASTGRASS predictions for the HT series of tests are in reasonable agreement with the data. Because of the large scatter of the data, smooth curves were plotted through those points (see Fig. 4.3 of Ref. 1); the I, Cs, and noble gas curves are reproducted in Fig. 2.2. The accuracy of these estimated-release results is about plus or minus one order of magnitude.[1] Also plotted in Fig. 2.2 are the FASTGRASS predictions (symbols) for Xe, I, and Cs release rate constants for the ORNL transient tests shown in Fig. 2.1.

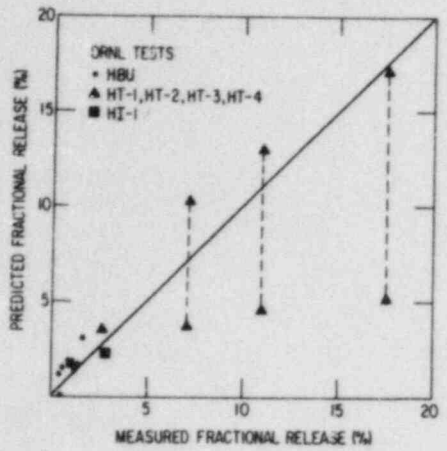

Fig. 2.1. Theoretical Predictions of Transient Gas Release vs Experimentally Measured Values from the HBU, HT, and HI Tests.

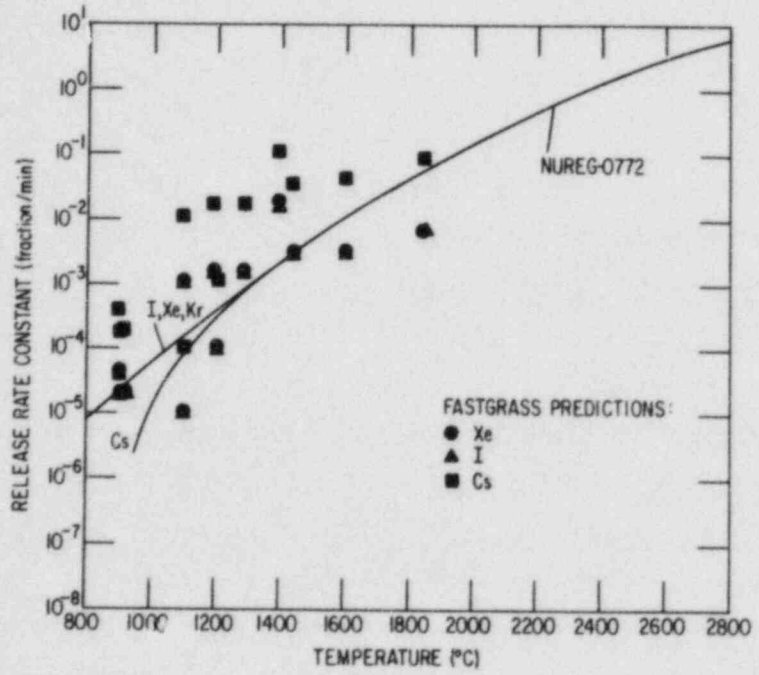

Fig. 2.2. FASTGRASS-predicted Fission Product Release Rate Constants for HBU-, HT-, and HI-Series Tests Compared with the NUREG-0772 Results.

In the low temperature range (up to ~1500°C), FASTGRASS-predicted xenon and iodine release rates (Fig. 2.2) are in good agreement with the NUREG-0772 estimated curve, i.e., FASTGRASS results lie on both sides of this curve in an accuracy range of plus or minus one order of magnitude. When the temperature increases above ~1500°C, predictions for xenon and iodine are somewhat below the NUREG-0772 curve. Cesium release rates calculated with FASTGRASS tend to be higher than the corresponding NUREG-0772 results.

The influence of heating rate, hold time (isothermal segment of the test), and time increment (Δt during which fractional release was measured) on the fission product release rate was also examined. Analyses were performed for different transient-temperature scenarios following a simulated H. B. Robinson fuel steady-state history. In order to cover the whole range of transient conditions used in the ORNL tests, the following values were selected for the specific operating conditions:

fuel temperature T:	800-2800°C
heating rate:	0.2, 1.0, 10.0 K/s
hold time:	1 min - 5 h
time increment Δt:	1 s and 1 min before the temperature, T, was reached and 1 min, 2 min, 30 min, and 5 h after the temperature, T, was reached.

The fractional release rate constant k(T) is defined as in Eqs. (2.2) and (2.3).

In Fig. 2.3, fractional-release-rate constants k(T) predicted by FASTGRASS are plotted as a function of fuel temperature for different values of Δt at a fixed heating rate of 0.2 K/s. The curves for ΔT= -1 min and -1 s represent release rate constants calculated for 1 min and 1 s respectively, before the final temperature T was reached. The remaining curves were generated from the amount of radionuclide released during the isothermal segment of the transient. Figure 2.3 shows that the value of the release rate constant as well as the shape of the function k(T) depends strongly on the choice of Δt. The best agreement with the NUREG-0772 curve, also shown in Fig. 2.3, is given by the FASTGRASS predictions obtained for isothermal releases calculated with Δt = +1 min. That curve is similar in shape to the NUREG-0772 curve, but is several orders of magnitude lower in value. In subsequent calculations, k(T) is defined as the fraction of current inventory released at temperature T during a 1-min period of time.

Figures 2.4 and 2.5 show the dependence of the FASTGRASS-predicted release rate constant k(T) on hold time for three temperatures (1400°C, 1800°C, 2200°C) and three values of heating rate (0.2, 1.0, 10.0 K/s). At all three temperatures, for hold times up to 0.5 h, k(T) changes drastically (by a few orders of magnitude) with changes in the hold time. For hold times longer than 0.5 h, k(T) becomes quite stable. Heating rate has a rather small effect on k(T) in the high-temperature range (above ~2000°C), and this effect is

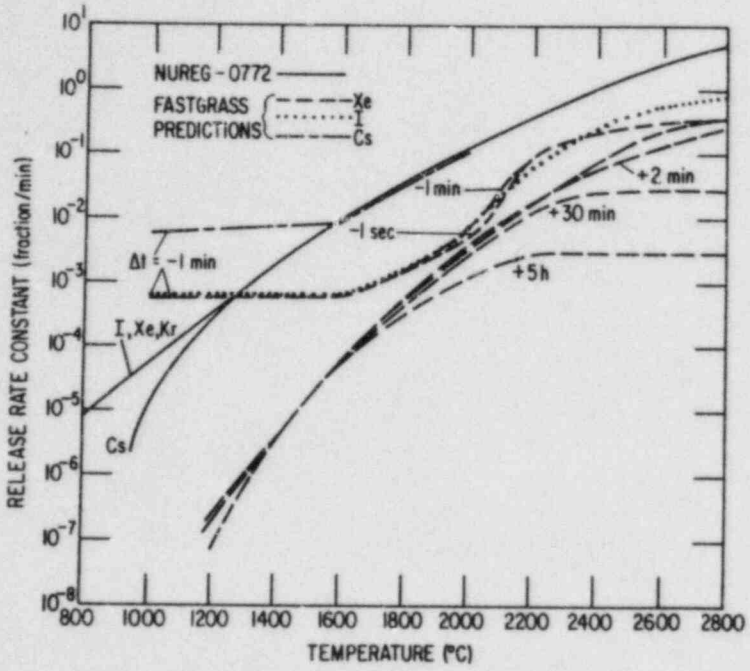

Fig. 2.3. FASTGRASS-predicted Fission Product Release Rate Constants as a Function of Fuel Temperature (Heating Rate = 0.2 K/s) for Various Values of Time Increment, Δt, Compared with the NUREG-0772 Results.

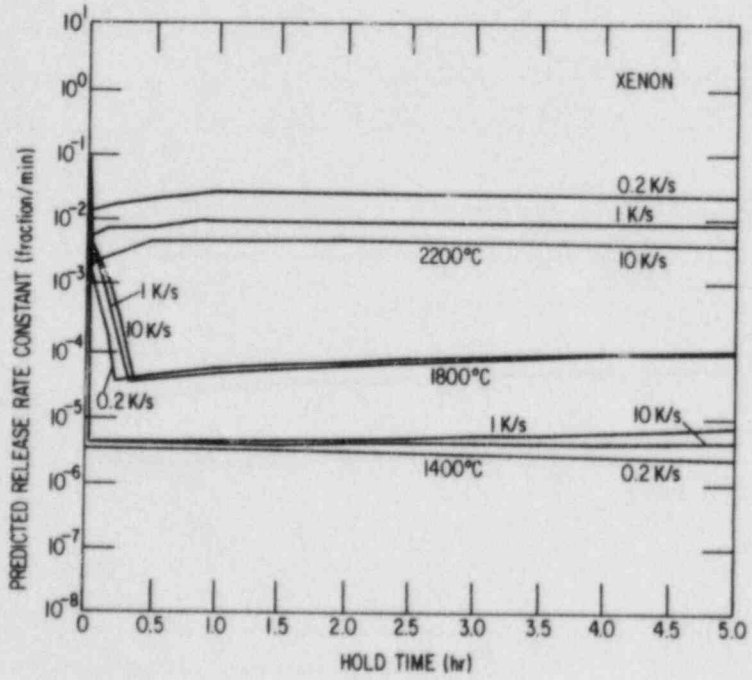

Fig. 2.4. FASTGRASS-predicted Xenon Release Rate Constants as a Function of Hold Time for Various Values of Fuel Temperature and Heating Rate.

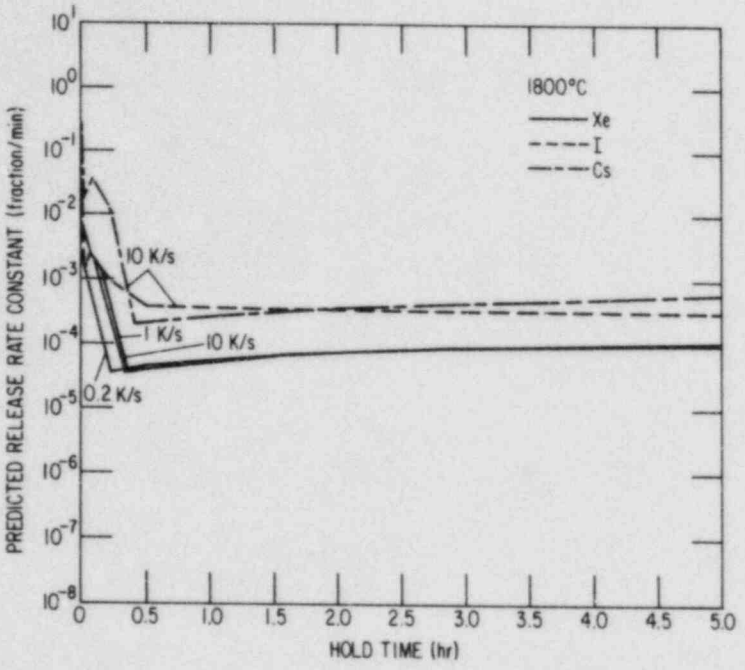

Fig. 2.5. FASTGRASS-predicted Fission Product Release Rate Constants as a Function of Hold Time (Temperature = 1800°C) for Various Values of Heating Rate.

independent of hold time. Below 2000°C, the effect of heating rate on k(T) depends on hold time; for hold times longer than 0.5 h (Figs 2.4 and 2.5), heating rate has little effect, but for hold times shorter than ~0.5 h (Fig. 2.6), k(T) increases markedly with an increase in heating rate.

B. Conclusions

Curves for the fission-product release-rate constant, k(T), provided in NUREG-0772 are based on the gas release data from three sets of experiments (Lorenz et al., Parker et al., and Albrecht et al.), whereas the experimental data base for the FASTGRASS calculations described in this report consists of just the ORNL transient tests.

Xenon and iodine release rates predicted with FASTGRASS for HBU-, HT-, and HI- series tests are in good agreement with the NUREG-0772 curve (Fig. 2.2). Release rates for noble gases and iodine are practically the same.

Cesium release rates, as predicted by FASTGRASS, tend to be higher than those reported in NUREG-0772 and thus are much higher than release rates for xenon and iodine. The diffusion coefficient used for cesium in FASTGRASS is

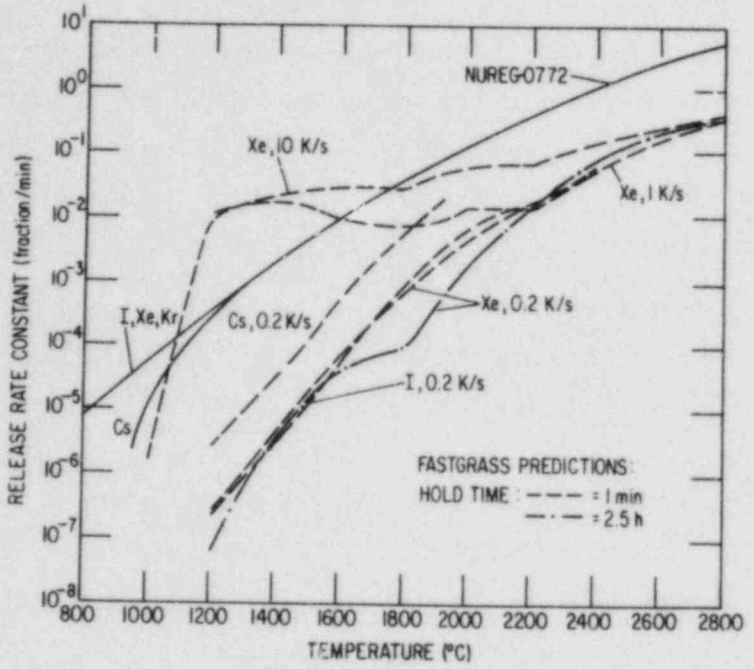

Fig. 2.6. FASTGRASS-predicted Fission Product Release Rate Constants as a Function of Fuel Temperature for Various Values of Hold Time and Heating Rate.

several orders of magnitude higher than the diffusion coefficient for xenon. Thus, the rate at which cesium is predicted to be released from the fuel is higher than for iodine and xenon. The diffusion coefficient for cesium is based on the experimental results of Oi and Takagi.[8] If it is assumed that atomic cesium diffuses at about the same rate as xenon and iodine, the FASTGRASS-predicted release rate constants for cesium will be in reasonable agreement (i.e., similar to the xenon and iodine results) with the NUREG-0772 results shown in Fig. 2.2. (At temperatures greater than ~1200 K, the NUREG-0772 curves for iodine, xenon, and cesium release rate constants are identical.)

Release of fission products is strongly dependent on the transient scenario. Heating rate appears to be important for short releases (less than 0.5 h; see Figs. 2.4-2.6). The choice of the time increment during which release is measured can drastically affect the value of the release rate constant as defined in Eqs. (2.2) and (2.3) (see Fig. 2.3). For example, note that the NUREG-0772 results for release rate constant (fraction/min) become greater than 1 for temperatures above 2400°C.

In general, the release-rate-constant curves generated by FASTGRASS are similar in shape to the NUREG-0772 curves (e.g., see Fig. 2.3), but are

several orders of magnitude lower in value. However, these variances may be due to differences in the transient scenario used for the calculation as compared to the actual test conditions (i.e., FASTGRASS predictions based on the actual test conditions are in better agreement with the NUREG-0772 curves than those based on "average" test conditions: see Figs. 2.2 and 2.3).

Finally, the ORNL transient fission product release tests were conducted in a steam environment. The steam can change fuel stoichiometry and can subsequently affect fission product release. In addition, higher fuel/cladding temperatures can lead to fuel liquefaction.[9] Figure 2.1 shows that FASTGRASS-VFP predictions of fission gas release during ORNL test HI-1 are in reasonable agreement with the data. However, FASTGRASS-VFP underpredicts gas release during the higher temperature HI-2 and HI-3 tests. (Extensive fuel liquefaction occurred during test HI-3; predictions for HI-2 and HI-3 are not shown in Fig. 2.1.) The FASTGRASS underprediction of fission gas release during the higher temperature HI-2 and HI-3 tests (and possibly also the three higher release tests shown in Fig. 2.1) indicates the importance of addressing oxidizing conditions and fuel liquefaction in fission product release models. Theoretical models describing the effects of a steam environment and fuel liquefaction on fission product release are not currently included in FASTGRASS. Models for these processes are currently under development.

C. References for Chapter II

1. U.S. Nuclear Regulatory Commission, Technical Basis for Estimating Fission Product Behavior During LWR Accidents, NUREG-0772 (June 1981).
2. J. Rest, The Prediction of Transient Fission-Gas Release and Fuel Microcracking Under Severe Core-Accident Conditions, Nucl. Technol 56, 553 (1981).
3. J. Rest, Evaluation of Volatile and Gaseous-Fission Product Behavior in Water Reactor Fuel Under Normal and Severe Core Accident Conditions, Nucl. Technol. 61, 33 (1983).
4. R. A. Lorenz, J. L. Collins, A. P. Malinauskas, O. L. Kirkland, and R. L. Towns, Fission Product Release from Highly Irradiated LWR Fuel, NUREG/CR-0722 (February 1980).
5. R. A. Lorenz, J. L. Collins, A. P. Malinauskas, M. F. Osborne, and R. L. Towns, Fission Product Release from Highly Irradiated LWR Fuel Heated to 1300-1600°C in Steam, NUREG/CR-1386 (November 1980).

6. M. F. Osborne, R. A. Lorenz, J. R. Travis, and C. S. Webster, Data Summary Report for Fission Product Release Test HI-1, NUREG/CR-2928 (December 1982).

7. S. M. Gehl, "UO_2-Zircaloy Reaction and Fission-Product Release Under Steam Oxidizing Conditions," in Reactor Safety Aspects of Fuel Behavior, American Nuclear Society, LaGrange Park, IL (1981), Vol. II, pp. 2-354 to 2-365.

8. N. Oi and J. Takagi, Diffusion of Non-Gaseous Fission Products in UO_2 Single Crystals, Z. Naturforsch. 19A, 1331 (1964).

9. A. W. Cronenberg, A. A. Applehans, R. K. McCandell, and J. Rest, "An Assessment of Liquefaction Induced I, Cs, and Te Release from Low and High Burnup Fuel," in Proc. Intl. Mtg. on Light Water Reactor Severe Accident Evaluation, Cambridge, MA, August 28-September 1, 1983, American Nuclear Society, LaGrange Park, IL (1979), Vol. I, pp. 4.5-1 to 4.5-8.

III. CLAD PROPERTIES FOR CODE VERIFICATION

Principal Investigators:
H. M. Chung, F. L. Yaggee, and T. F. Kassner

The Zircaloy cladding of fuel rods in light-water-cooled reactors is susceptible to local breach-type failures, commonly known as pellet-cladding interaction (PCI) failures, during power transients after the fuel has achieved sufficiently high burnup. As a result of the high burnup, the gap between the UO_2 fuel pellets and the cladding is closed and highly localized stress is believed to be imposed on the cladding by differential thermal expansion of the cracked fuel and cladding during power transients. In addition to the localized stress, a high-burnup fuel cladding is also characterized by high-density radiation-induced defects (RID), mechanical constraints imposed by pellet-cladding friction, compositional changes (e.g., oxygen and hydrogen uptake associated with in-service corrosion), and geometrical changes due to creep-down and bowing. It is possible that synergistic effects involving more than one of the above factors influence the deformation and fracture of the in-reactor fuel cladding, e.g., strain aging associated with impurity or alloying elements, irradiation- or stress-induced segregation of the elements and subsequent formation of non-equilibrium phases. Although mechanisms of stress corrosion cracking (SCC) associated with volatile fission products such as I and liquid metal embrittlement (LME) associated with an element such as Cd have been well established for local breach-type failures of irradiated and unirradiated Zircaloy cladding under out-of-reactor simulation conditions, conclusive evidence of these processes is not yet available for in-reactor PCI failures. Consequently, to provide a better understanding of the PCI phenomenon, we have undertaken a mechanistic study of the deformation and fracture behavior of actual power-reactor fuel cladding discharged after a high burnup.

In this program, the effect of temperature, strain rate, and stress localization on the deformation and fracture characteristics of Zircaloy cladding from spent-fuel rods is being investigated by means of internal gas-pressurization and mandrel-loading experiments in the absence of simulated fission product species. The deformed and fractured specimens of spent-fuel

cladding are then being examined by optical microscopy, scanning electron microscopy (SEM), transmission electron microscopy (TEM), and high-voltage electron microscopy (HVEM). The results of microstructural and fracture-property investigations will be used to develop a failure criterion for the cladding under PCI-type loading conditions. The information will be incorporated into fuel performance codes, which can be used to evaluate the susceptibility of extended-burnup fuel elements in commercial reactors to PCI failures during power transients in later cycles, and to evaluate cladding performance and reliability of new fuel-element designs. An optimization of power ramp procedures to minimize cladding failures would result in a significant decrease in radiation exposure of plant personnel due to background and airborne radioactivity as well as an extension of core life in terms of allowable off-gas radioactivity.

A. TEM-HVEM Analysis of Zr_3O Precipitates (H. M. Chung)

1. Introduction

In continuation of the previously reported[1-4] efforts to characterize the Zr_3O precipitates that were correlated with the PCI-like, brittle-type failures of the Big Rock Point and H. B. Robinson reactor spent fuel cladding, thin-foil specimens obtained from the brittle-type failure tubes were examined further by TEM and HVEM. The Zr_3O precipitates that decorated individual dislocations were directly observed. The observation provides strong evidence of the interaction between oxygen solute and moving dislocations in the material.

2. Interaction of Dislocations with Oxygen

The HVEM micrograph of Fig. 3.1(A) shows an area containing dislocations in the thin-foil specimen obtained from the region adjacent to the failure site of the Big Rock Point cladding tube 165AE4B.[3] A selected area encircled in Fig. 3.1(A) is shown at higher magnification in Fig. 3.1(B). The indexed diffraction pattern of the selected area [Fig. 3.1(C)] shows the α-Zr zone of $[1\bar{2}13]_\alpha$ and the Zr_3O zone of $[\bar{1}\bar{3}\ 14\ \bar{1}\ 0]_{Zr_3O}$. Weak reflections from the surface χ-hydride are also visible. The weak reflections $(54\bar{9}0)$, $(54\bar{9}2)$,

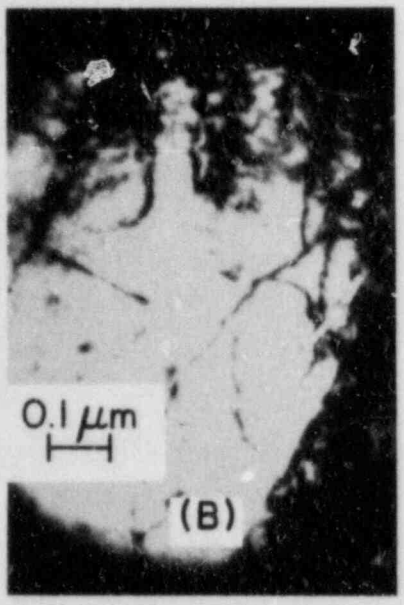

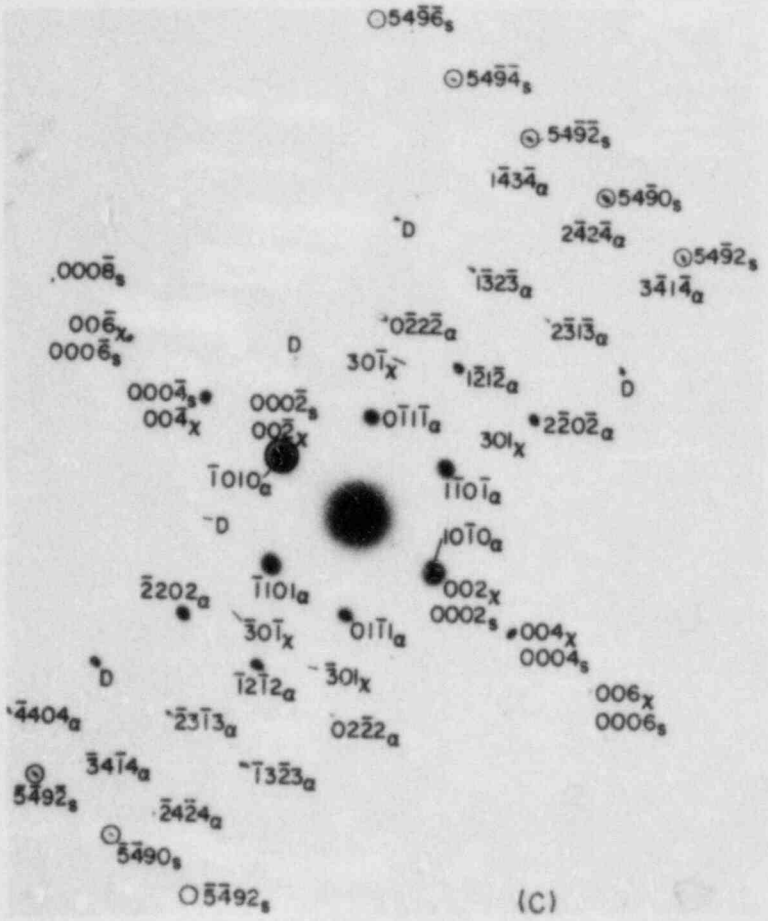

Fig. 3.1.

1-MeV HVEM Micrographs of a Thin-Foil Specimen Obtained from a Region Adjacent to the Failure Site of Big Rock Point Reactor Cladding Specimen 165AE4B. (A) Bright-field morphology; (B) higher magnification of the circled area of (A), showing dislocations; (C) indexed diffraction pattern of (B), showing $[1\bar{2}13]_{\alpha}$ and $[\bar{1}3\ 14\ \bar{1}\ 0]_{Zr_3O}$ zone axes; and (D) dark-field image of $(000\bar{2})_{Zr_3O}$, showing the dislocations decorated by the Zr_3O precipitate. In (C), subscripts α, s, and χ and letter D denote reflections from α-Zr, Zr_3O, χ-hydride, and double diffractions, respectively.

$(54\bar{9}\bar{2})$, $(\bar{5}490)$, $(\bar{5}492)$, $(\bar{5}49\bar{2})$, and $(54\bar{9}\bar{4})$ visible in Fig. 3.1(C) are superlattice reflections[3,4] that are characteristic of the Zr_3O phase. The dark-field image of the reflections denoted by the large circle in Fig. 3.1(C) is shown in Fig. 3.1(D). The dark-field image clearly shows that the individual dislocations are decorated by the Zr_3O precipitates. The moiré fringes, faintly observed in Fig. 3.1(D), are produced by the $(00\bar{2})_\chi$ reflection of the surface hydride film which is superimposed on the $(000\bar{2})_{Zr_3O}$ reflection of the Zr_3O phase. The measured spacing of the moiré fringe is between ~75 and 90 Å. This is in good agreement with the value of 84 Å calculated from the equation

$$D = \frac{d^{Zr_3O}_{000\bar{2}} \cdot d^{\chi}_{00\bar{2}}}{d^{Zr_3O}_{000\bar{2}} - d^{\chi}_{00\bar{2}}}, \qquad (3.1)$$

where $d^{Zr_3O}_{000\bar{2}} = 2.598$ Å and $d^{\chi}_{00\bar{2}} = 2.520$ Å. The observed fringe spacing is not compatible with any other combinations among d-spacings of $(00\bar{2})_\chi$, $(000\bar{2})_\alpha$, and $(\bar{1}010)_\alpha$.

Another direct observation of individual dislocations decorated by Zr_3O precipitates is shown in Fig. 3.2. These results from the 100-keV TEM analysis show that the reflections from the surface χ-hydride are quite strong. Because of the surficial nature of the hydride, a dark-field image of the hydride reflection [e.g., the $(\bar{3}0\bar{1})_\chi$ image shown in Fig. 3.2(F)] does not show images of dislocations. However, in the dark-field image of Fig. 3.2(E), which was produced from the $(000\bar{2})_{Zr_3O}$ and $(00\bar{2})_\chi$ reflections denoted by the small circle in Fig. 3.2(D), individual dislocations that are decorated by the Zr_3O phase can be clearly observed along with the morphologies of the hydride particles.

Another example of the characteristic diffraction patterns of the Zr_3O phase similar to those shown in Fig. 3.1(C) is shown in Fig. 3.3. A recrystallized grain and a selected area in the grain containing the Zr_3O phase are shown in Fig. 3.3(A) and (B), respectively. The diffraction pattern of Fig. 3.3(C) shows numerous double-diffraction spots of the Zr_3O phase similar to those of Fig. 7(D) of Ref. 4.

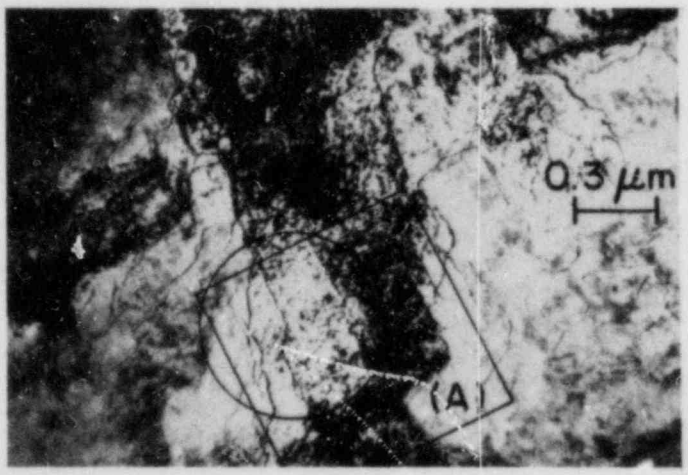

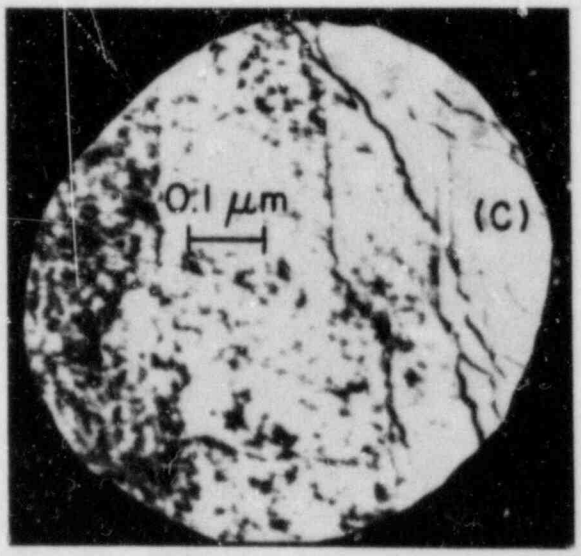

Fig. 3.2. TEM Micrographs (Similar to Fig. 3.1) of Individual Dislocations Decorated by Zr_3O Precipitates. (A) Bright-field morphology of an area containing dislocations; (B) higher magnification of part of boxed-in region of (A); (C) selected area of (B); (D) indexed diffraction pattern of (C); (E) dark-field image of the combined reflections of $(000\bar{2})_{Zr_3O}$ and $(00\bar{2})_{\chi}$; and (F) dark-field image of $(\bar{3}0\bar{1})_{\chi}$ reflection (surface hydride). The labeling notation for (D) is the same as for Fig. 3.1(C).

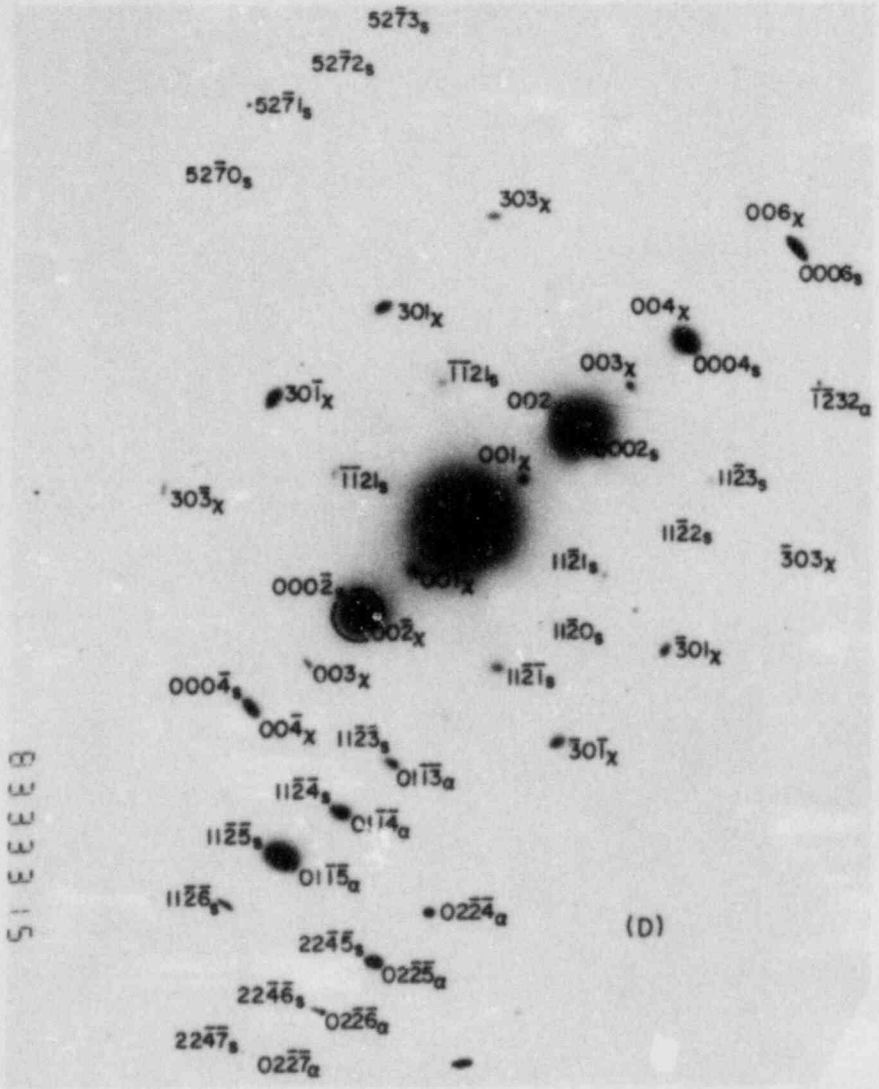
$52\bar{7}3_s$
$52\bar{7}2_s$
$52\bar{7}1_s$
$52\bar{7}0_s$
303_X
006_X
0006_s
301_X
004_X
003_X
0004_s
$\bar{1}\bar{1}21_s$
$30\bar{1}_X$
002
$\bar{1}\bar{2}32_\alpha$
001_X
002_s
$\bar{1}\bar{1}21_s$
$11\bar{2}3_s$
303_X
$11\bar{2}2_s$
$11\bar{2}1_s$
$\bar{3}03_X$
$000\bar{2}_s$
001_X
$00\bar{2}_X$
$11\bar{2}0_s$
$\bar{3}01_X$
0004_s
003_X
$11\bar{2}\bar{1}_s$
$00\bar{4}_X$
$11\bar{2}\bar{3}_s$
$30\bar{1}_X$
$01\bar{1}\bar{3}_\alpha$
$11\bar{2}\bar{4}_s$
$01\bar{1}\bar{4}_\alpha$
$11\bar{2}\bar{5}_s$
$01\bar{1}\bar{5}_\alpha$
$11\bar{2}\bar{6}_s$
$02\bar{2}\bar{4}_\alpha$
(D)
$22\bar{4}\bar{5}_s$
$02\bar{2}\bar{5}_\alpha$
$22\bar{4}\bar{6}_s$
$02\bar{2}\bar{6}_\alpha$
$22\bar{4}\bar{7}_s$
$02\bar{2}\bar{7}_\alpha$
S-33338

Fig. 3.2. (Contd.)

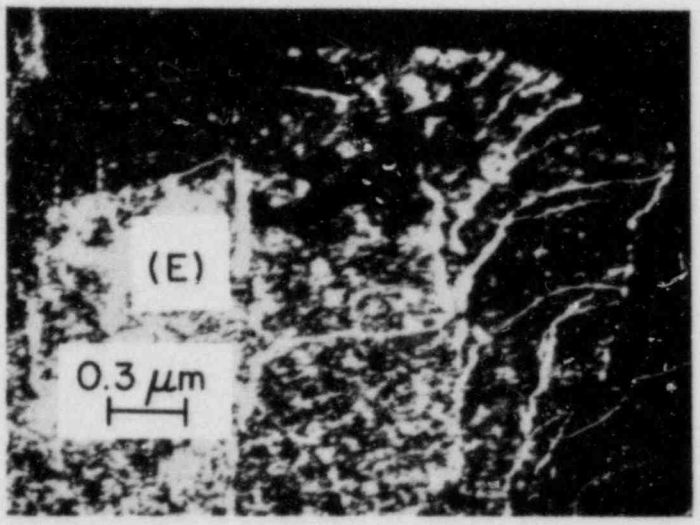

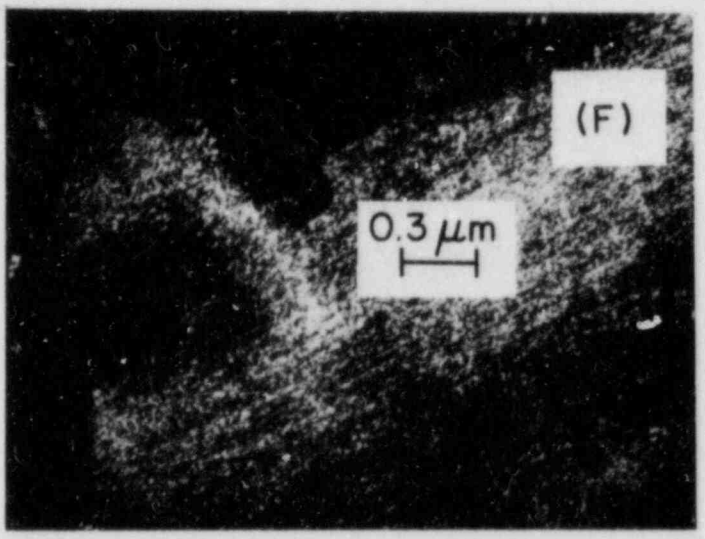

Fig. 3.2. (Contd.)

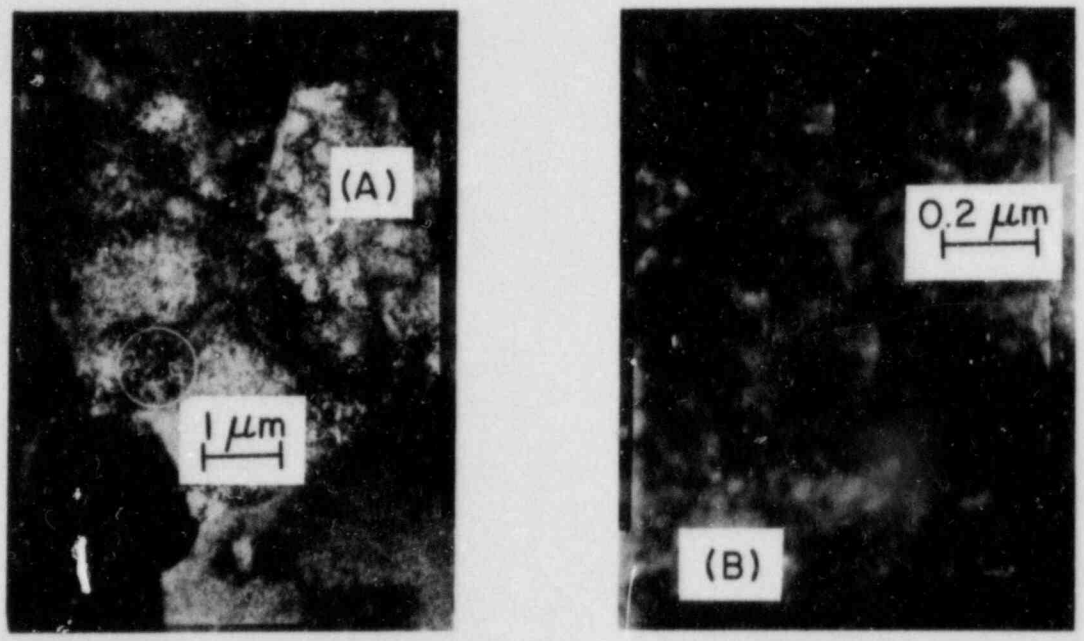

Fig. 3.3. 1-MeV HVEM Micrographs of a Recrystallized Grain of the 165AE4B Specimen Containing Zr_3O Precipitates. (A) Bright-field image containing a recrystallized grain; (B) higher magnification of the circled area within the grain of (A); (C) diffraction pattern of (B) produced with 0.8-m camera length; and (D) indexed diffraction pattern produced with 2-m camera length. The labeling notation for (D) is the same as for Fig. 3.1(C).

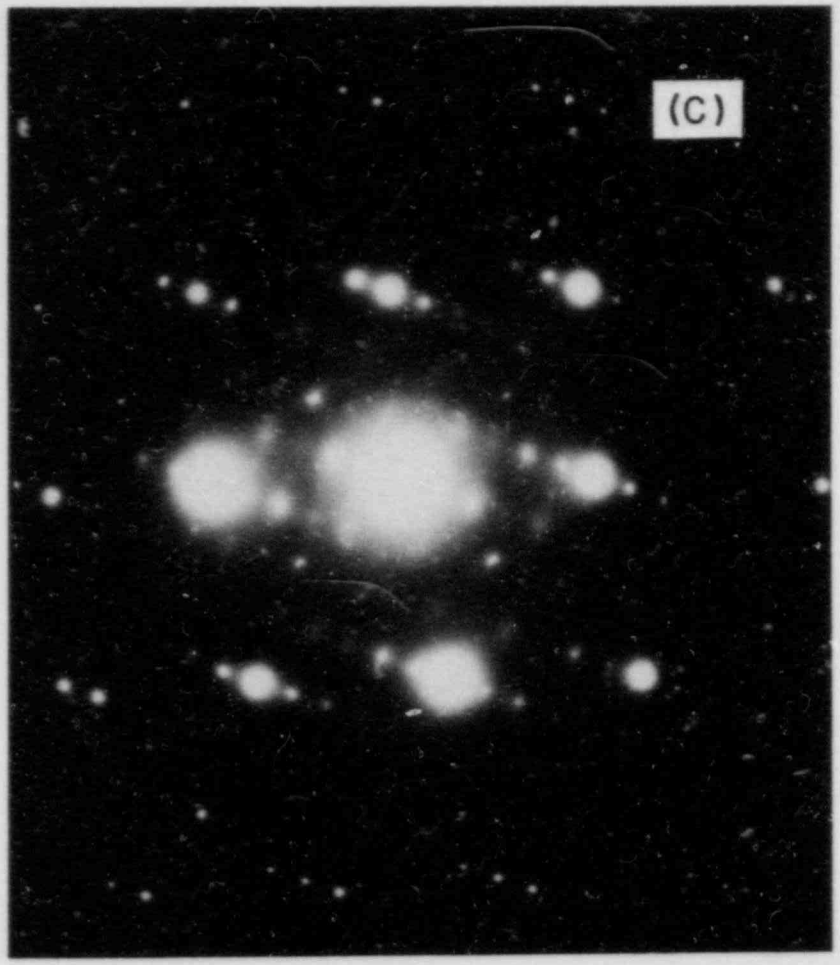

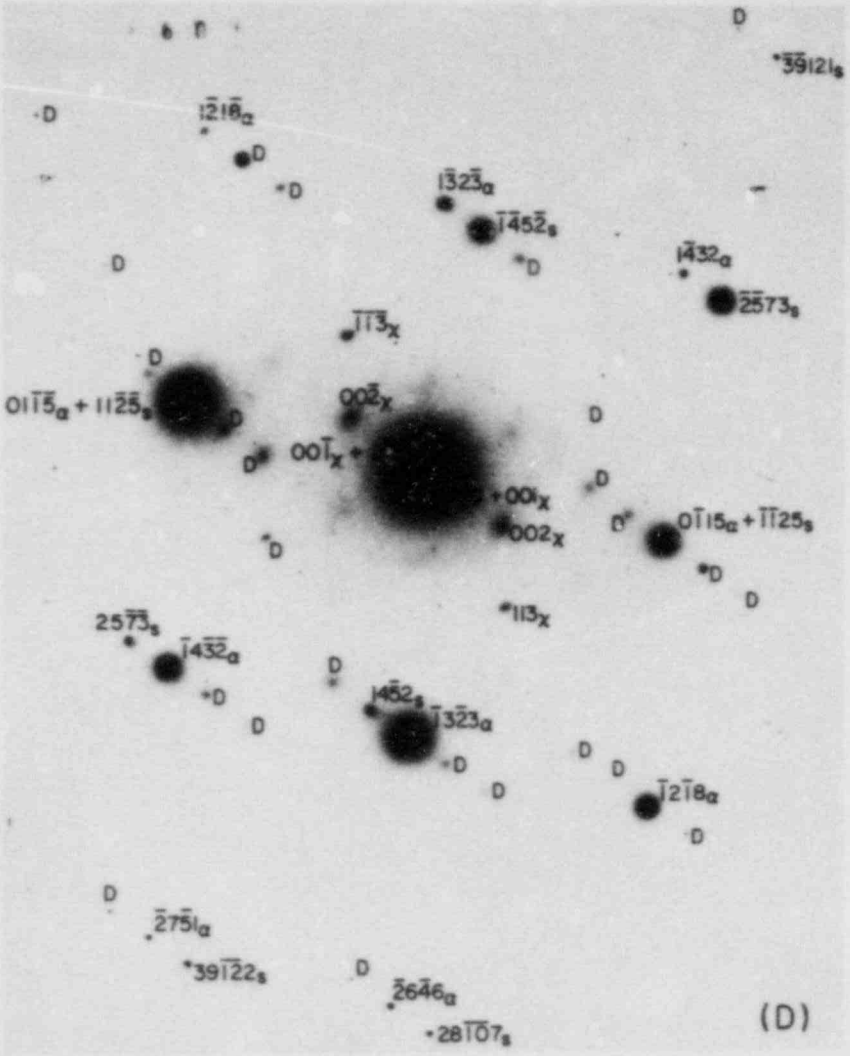

Fig. 3.3. (Contd.)

The results described above (e.g., the results of Fig. 3.1, which show the decoration of individual dislocations by the Zr_3O phase and the superlattice reflections of the phase) provide strong evidence of the segregation of oxygen to the dislocations, thereby leading to formation of the Zr_3O phase and to immobilization of the dislocations. As a result, plastic deformation of the Zircaloy cladding is minimized.

B. SEM Examination of H. B. Robinson Cladding Tubes Fractured by Mandrel Expansion (H. M. Chung)

1. Introduction

The fracture characteristics of the H. B. Robinson reactor spent-fuel cladding as determined by mandrel expansion at 292°C were summarized in Table XIII of Ref. 5. During the current reporting period, the fracture characteristics of the H. B. Robinson cladding specimens have been examined by SEM. Morphologies of the inner and outer surfaces and fracture surfaces were examined to determine the mode of fracture and the direction of crack propagation. Of the specimens described in Table XIII of Ref. 5, only the 217A2E tube was found to have failed; the other three tubes did not contain a through-wall crack. The 217A2E tube failed in a ductile manner. However, SEM examination of two other specimens, subsequently tested at 325°C instead of 292°C (i.e., tubes 217A4C and 217A4E of Table 3.1), confirmed that brittle-type failures had occurred. Fracture types identified from mandrel expansion tests are summarized in Table 3.1 and details of the SEM examinations are described below.

2. Ductile Failure

The fracture surface of the 217A2E tube after fracture at a test temperature of 292°C (see Table 3.1) is shown in Fig. 3.4(A). The specimen was loaded incrementally at an average strain rate of 5×10^{-5} s^{-1} for 0.3 h and held at the maximum load for 0.3 h. Compression marks made by the split rings are visible on the inner surface of the tube in Fig. 3.4(A). Near the inner surface, the fracture surface is featureless and relatively smooth. This morphology extends toward the outer surface of the tube and is more

TABLE 3.1. Mandrel Expansion Tests on H. B. Robinson Spent-Fuel Cladding

Specimen Number	Test Temp., °C	Time of Transient Loading, h	Strain Rate During Transient Loading, s^{-1}	Maximum Mandrel Load, kg	Time in Creep Mode at Max. Load, h	Total Time to Failure, h	Plastic Diametral Strain at Outer Surface, %	Failure Mode
217A2C	292	17.1	5×10^{-7}	505	0	-	1.2	No failure
217A2D	292	5.0	5×10^{-6}	740	0	-	2.4	No failure
217A2E	292	0.3	5×10^{-5}	772	0	0.3	3.3	Ductile (rupture)
217A2F	292	28.9	5×10^{-7}	775	0	-	1.3	No failure
217A4C	325	25.5	5×10^{-7}	459	36.0	68.1	4.7	Brittle (pinhole)
217A4E	325	44.1	2×10^{-7}	845	189.7	223.8	6.0	Brittle (pinhole)

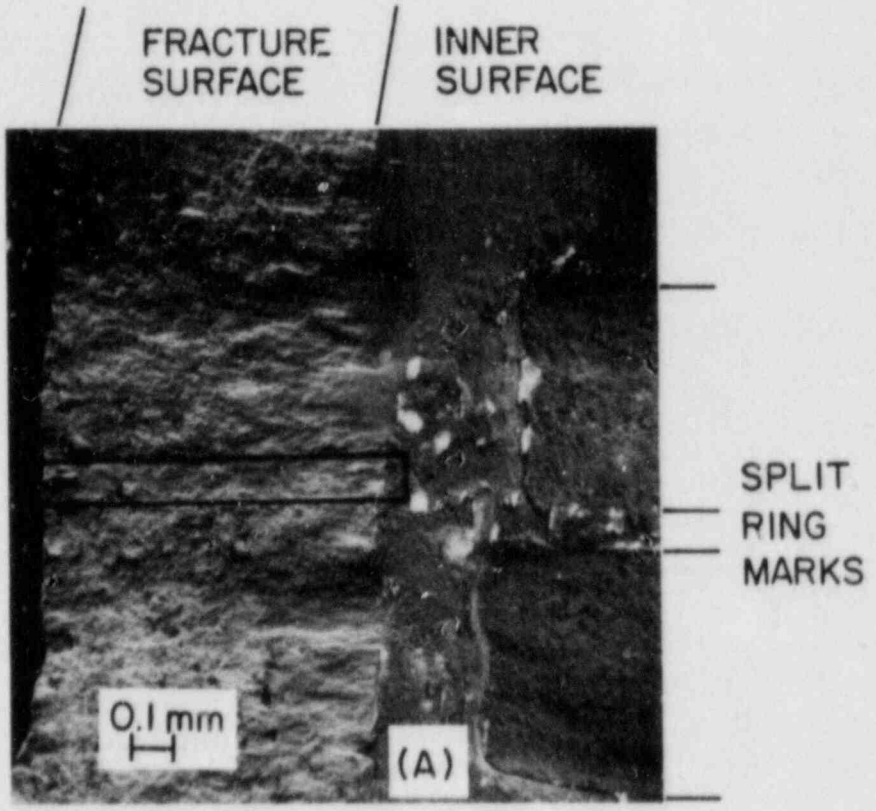

Fig. 3.4. Fracture Surfaces of H. B. Robinson Cladding Tube 217A2E after Ductile Failure in Mandrel Expansion Test at 292°C. (A) Whole fracture surface and (B) higher magnification of the marked strip of (A) showing a ductile fracture.

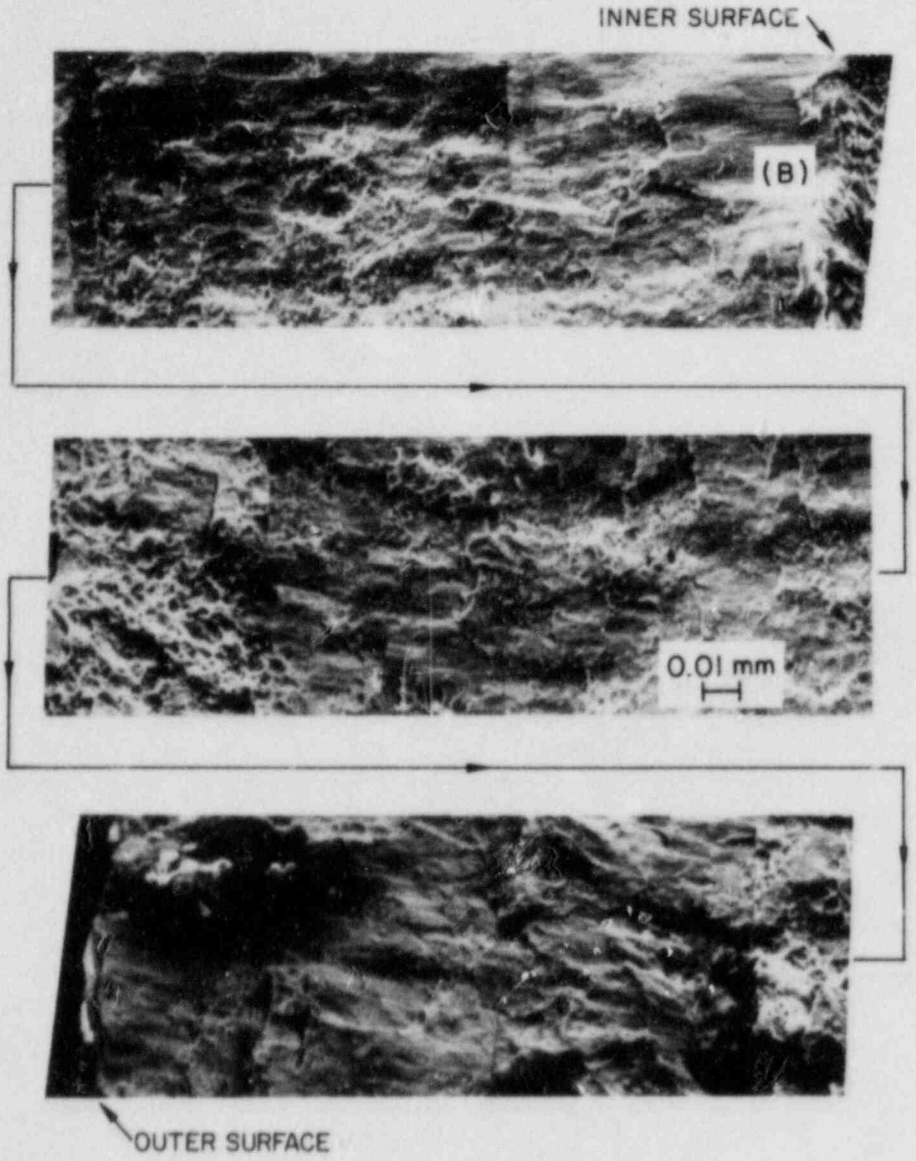

Fig. 3.4. (Contd.)

pronounced near the compression lines of the ring edges than in other regions. The smooth morphology was, however, identified to be an artifact caused by fine particles which smeared the fracture surface during ultrasonic-erosion cutting of the SEM specimen. A higher magnification of the marked strip of Fig. 3.4(A) is shown in Fig. 3.4(B). The morphology of the fracture surface shown in Fig. 3.4(B) is characteristic of a ductile fracture mode. No regions characterized by pseudocleavage or fluting could be observed over the entire fracture surface.

The ductile fracture mode deduced from SEM examination is consistent with the morphology of the fracture tip cross section, which is shown in Fig. 3.5. The orientation of the fracture surface at ~45° to the radial direction of the specimen is typical of ductile shear. The morphology of the fracture tip is similar to that in tube 165W-21 (shown in Fig. 7 of Ref. 6), which underwent ductile failure. As indicated in Fig. 3.5, significant

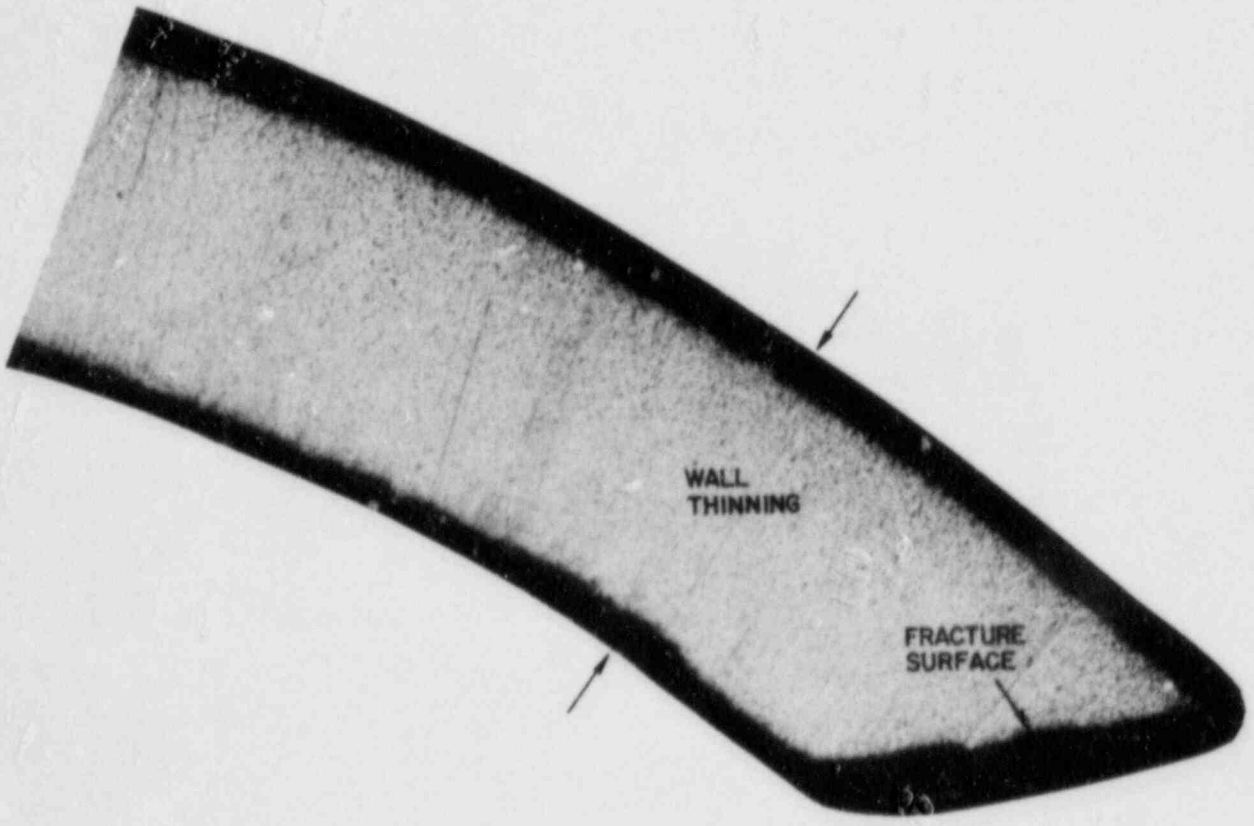

Fig. 3.5. Optical Micrograph of a Cross Section of the Fracture Tip of the Specimen of Fig. 3.4, Showing Ductile Shear Fracture.

(~9.5%) thinning of the cladding wall is observed near the fracture tip; however, wall thinning at the fracture tip itself is negligible. This contrasts with the fracture radial strain of the 165W-21 specimen, which was deformed by internal gas pressurization. Figure 3.5 also reveals an unusual orientation of the bulk hydrides, i.e., hydride stringers nearly perpendicular to the tangential direction. Normally, the bulk hydrides in the spent-fuel cladding material are aligned parallel to the tangential direction of the tube (e.g., see Fig. 7 of Ref. 6) because tangential stress is normally the principal stress that occurs during in-reactor service. Although the observations are inconclusive, it appears that the in-reactor stress imposed on the tube segment of Fig. 3.5 (i.e., at the fracture location of the 217A2E tube) was primarily axial.

3. Brittle-Type Failure

The H. B. Robinson cladding tube 217A4C, deformed and fractured at 325°C at a slower strain rate and at a smaller creep load than other test specimens (see Table 3.1), was examined by SEM. The morphology of the outer surface near the fracture site is shown in Fig. 3.6. Significant ridging and "x-marks," produced by deformation and straining of the surface oxide layer, are visible in Fig. 3.6(A). Two through-wall failure sites (denoted by arrows) are visible in the figure. They are located precisely at the cross points of the x-marks. The x-marks, along with the pseudocleavage-plus-fluting feature of the fracture surface, are generally considered characteristic of a PCI failure. A higher magnification of the fracture site at the right side of Fig. 3.6(A), shown in Fig. 3.6 (B), reveals the crack patterns of the surface oxide layer. Along the ridge, axial as well as circumferential cracks in the oxide layer are visible. This indicates that the stress, concentrated near the ridge by the expanding ring, is complex. In contrast to the stress components expected for an internal gas-pressurization test, the axial component of the stress appears to be comparable to or larger than the circumferential component.

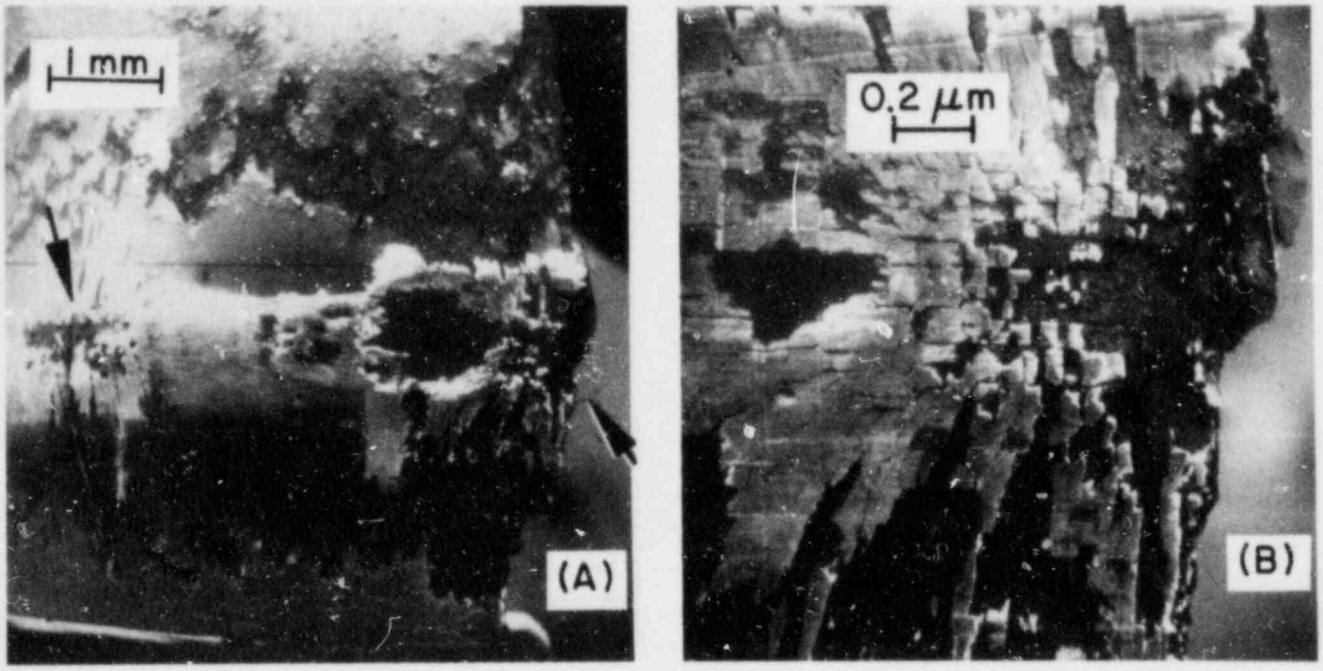

Fig. 3.6. SEM Morphology of the Outer Surface of H. B. Robinson Cladding Tube 217A4C after Brittle-Type Failure in Mandrel Expansion Test at 325°C. (A) Low magnification showing "x-marks" and through-wall cracks (arrows) located at the cross points of the x-marks, and (B) higher magnification showing crack morphology of the surface oxide layer near a through-wall crack.

The distribution of cracks on the inner surface of the cladding tube is shown in Fig. 3.7. The compression mark made by the single expanding ring is visible in Fig. 3.7(A) and (B). In contrast to the outer-surface cracks, located only at the cross points of the x-marks, numerous cracks that are more or less randomly distributed near the expanding ring can be observed. This difference between the crack distributions on the outer and inner surfaces clearly shows that the cracks nucleated at the inner surface and propagated toward the outer surface. The slanting group of small cracks denoted by an arrow in Fig. 3.7(A) and the jogs in the cracks of Fig. 3.7(C) are also characteristic of a PCI failure.

Fracture surfaces of the above specimen at and near the location of the expanding ring are shown in Figs. 3.8 and 3.9, respectively. The fracture surfaces of Figs. 3.8(A) and 3.9(A) show significant roughness, i.e., many "steps" or "plate-like" features. The morphology is similar to that of the fracture surface reported by Rosenbaum et al.[7] for the fuel rods that failed

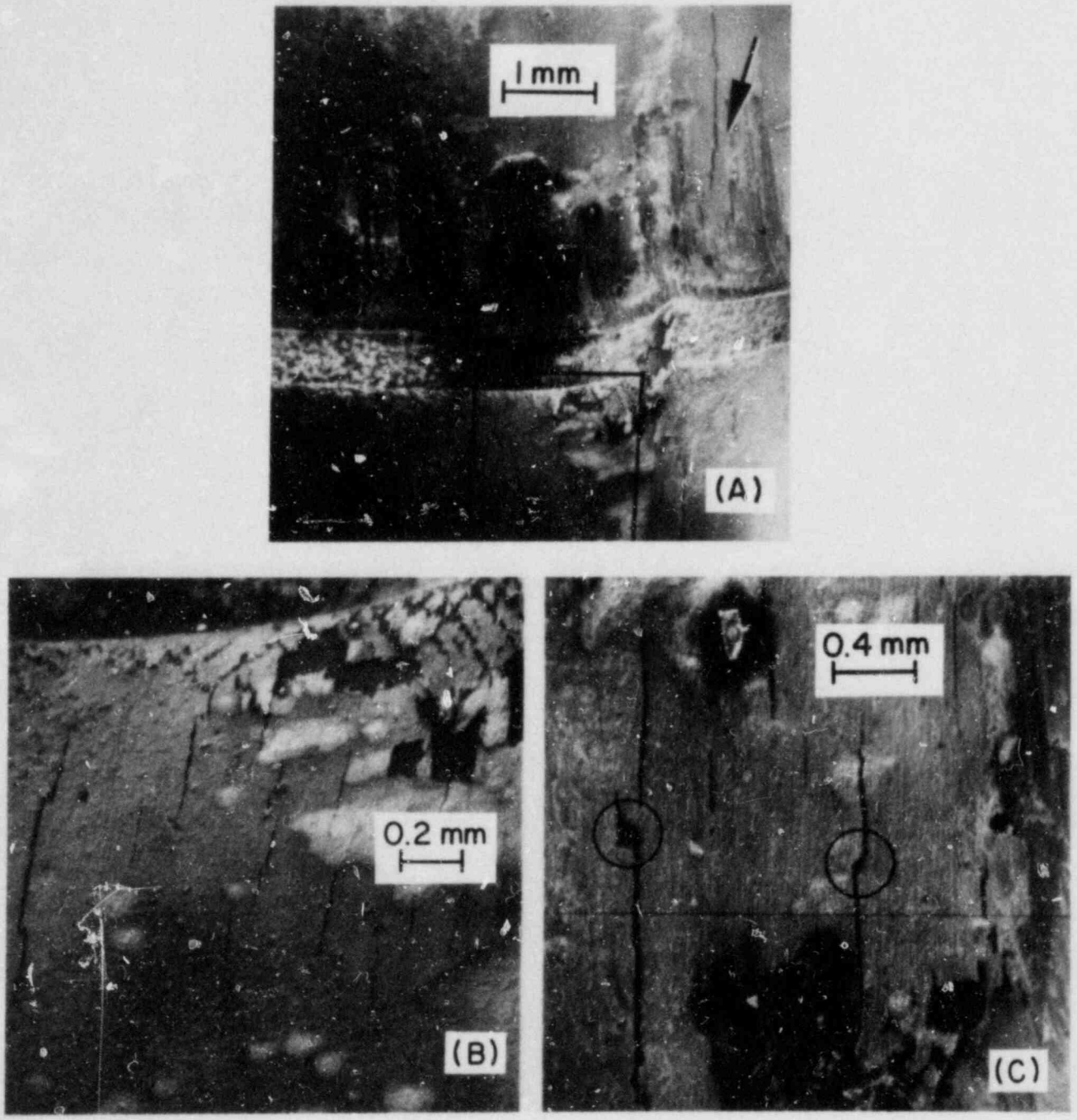

Fig. 3.7. SEM Morphology of the Inner Surface of the Specimen of Fig. 3.6. (A) Low magnification showing numerous cracks and compression mark made by the expanding ring; (B) higher magnification of the bounded area of (A); and (C) higher magnification showing characteristic crack morphology (jogs).

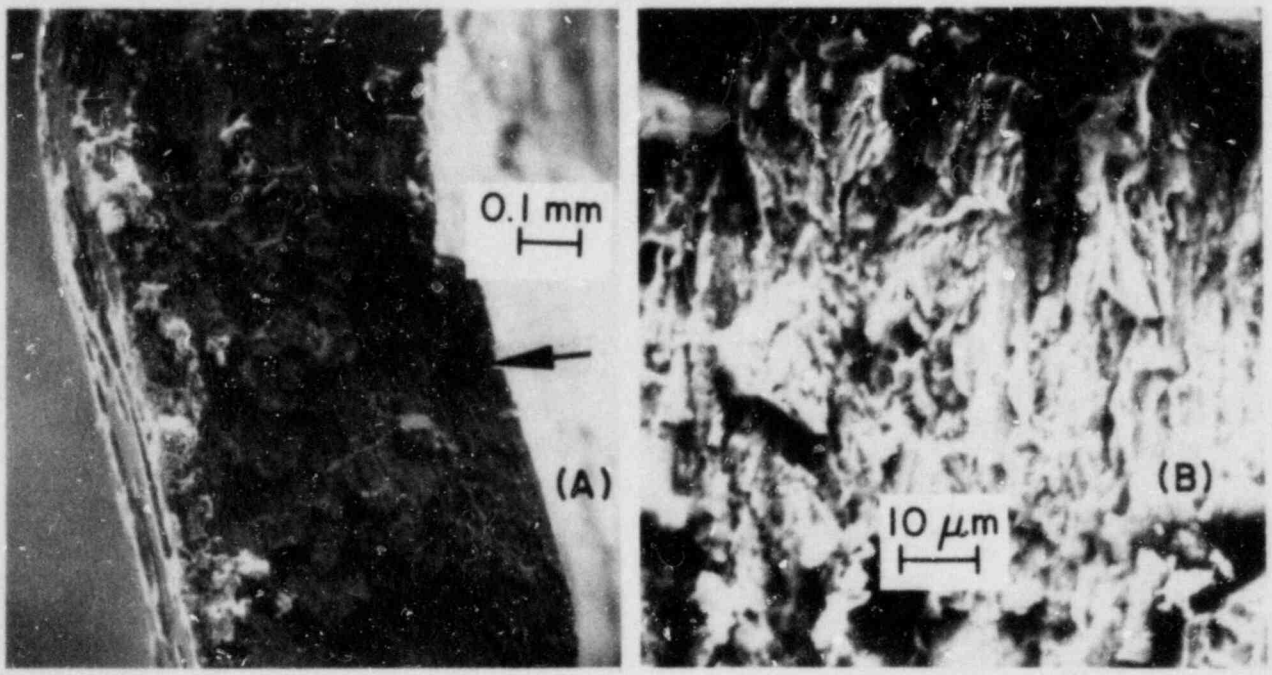

Fig. 3.8. SEM Fracture Surface Morphology of the Specimen of Fig. 3.6, at the Location of the Expanding Ring. (A) View encompassing outer and inner surfaces (the inner-surface compression mark is visible just to the left of the scale marker); (B) higher magnification of the circled, arrowed area of (A), showing pseudocleavage.

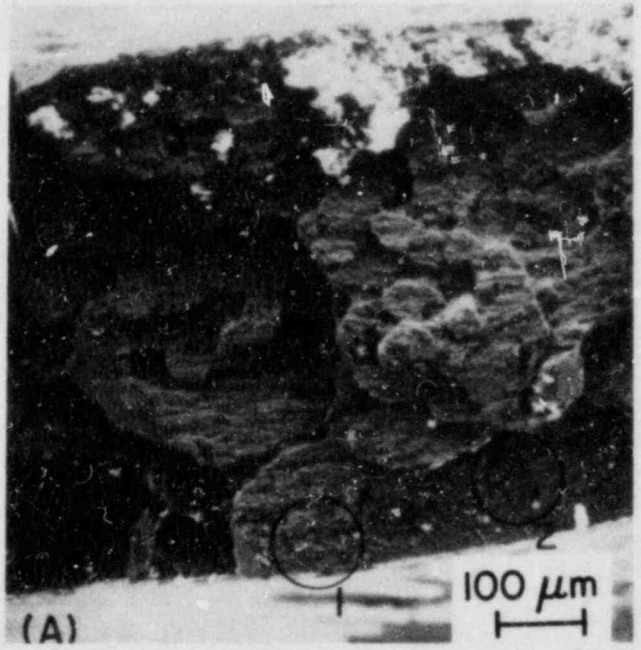

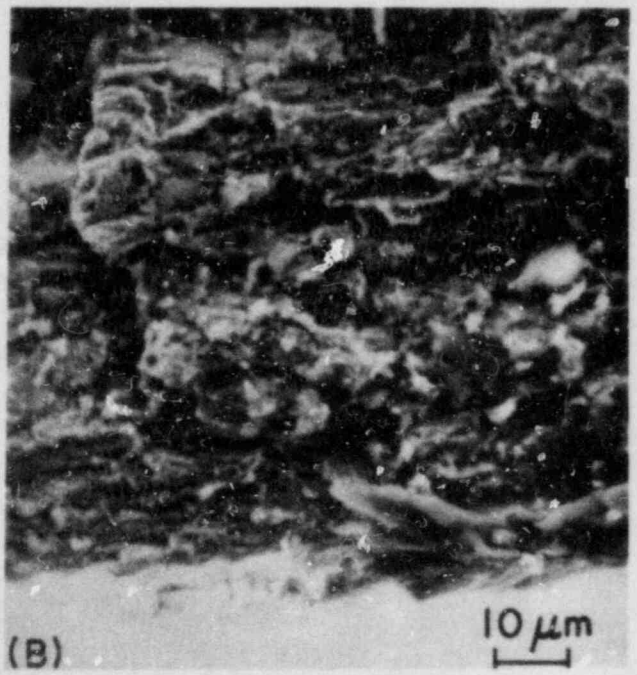

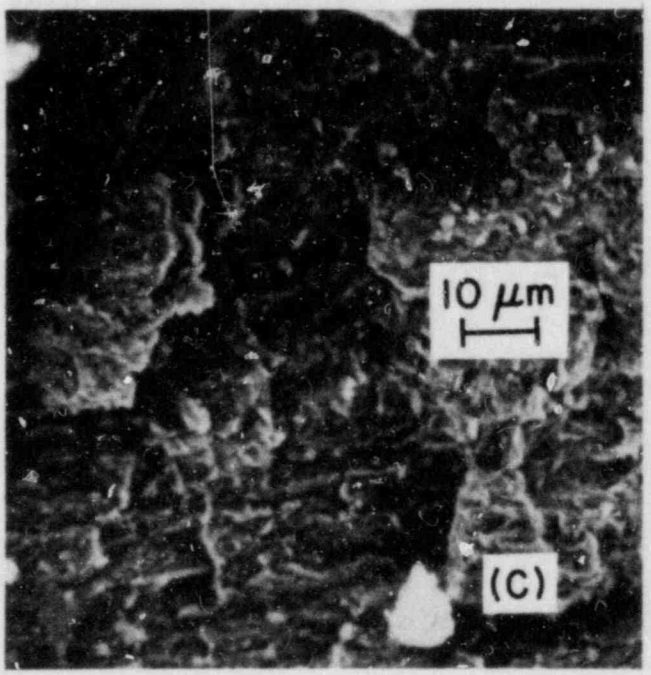

Fig. 3.9. SEM Fracture Surface Morphology of the Specimen of Fig. 3.6, near the Location Shown in Fig. 3.8. (A) Low magnification; (B) and (C) higher magnifications of circles 1 and 2 of (A), respectively, showing pseudocleavage.

during service in the Dresden-III reactor (e.g., see Figs. 3.2-17 of Ref. 7). Figures 3.8(B), 3.9(B), and 3.9(C) show higher magnifications of specific fracture surface regions near the inner surface. At these higher magnifications, the pseudocleavage nature of the fracture surface is evident. However, no area of fluting could be observed in the fracture surface. Overall, the fracture characteristics of the 217A4C tube, revealed in Figs. 3.6-3.9, indicate a brittle-type failure of the specimen.

C. Biaxial Stress Rupture Properties of Irradiated Maine Yankee Fuel Cladding (F. L. Yaggee)

Biaxial stress rupture tests are in progress on another lot of irradiated Zircaloy fuel cladding at 325°C in the absence of simulated fission products. The fast-neutron fluence of the Maine Yankee cladding is ~0.33 of the value for the H. B. Robinson cladding (~4 x 10^{25} n/m^2, E > 0.1 MeV).[8] In these experiments, a small (13.3 mm long x 3.4 mm wide) flat area was ground on the outside surface of the specimen to reduce the wall thickness by ~0.13 mm (20%). This grinding removed the surface oxide layer locally, and hence, the intrinsic tangential stress on the underlying metal, associated with the oxide layer, was also removed. The specimen (217K2G) was tested at a maximum hoop stress of 540 MPa in the oxide-free flat region, and failed within that region after 74 h at a diametral strain of 3.4%. The average strain rate was 1.3 x 10^{-7} s^{-1}. Preliminary results of SEM examination of this specimen have been reported previously.[9] Results of a more detailed examination are described here. The failure site is shown in Fig. 3.10. The location of the failure within the flat region on the cladding specimen is shown schematically in Fig. 3.11; for purposes of discussion, the portion of the specimen containing the flat region has been schematically divided into eight sections of equal length. The physical size, shape, and orientation of the pinhole breach in relation to the specimen axial direction are shown at high magnification (125X) in Fig. 3.12. The breach is oriented parallel to the axial direction and the fracture surface intersects the specimen surface at an angle of about 30°. The dimpled appearance of this part of the fracture surface is consistent with ductile fracture (nucleation, growth, and coalescence of microvoids). Figure 3.13 shows the fracture surface at high magnification.

(a)

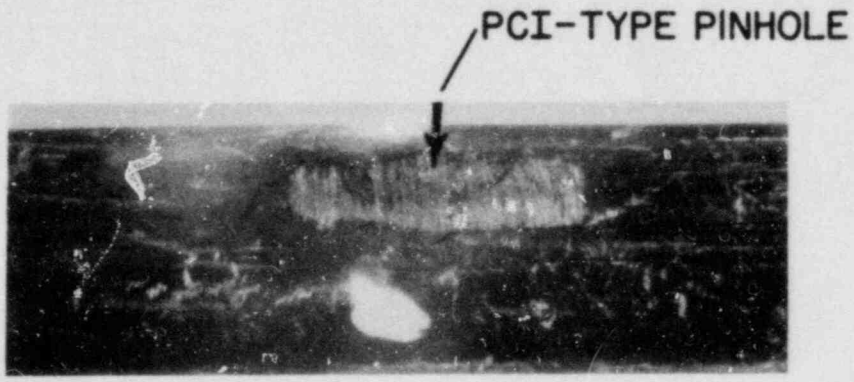

(b)

Fig. 3.10. Pinhole Breach in Maine Yankee Specimen 217K2G Tested for 74 h at 325°C and 540 MPa Hoop Stress. (a) Visual indication produced at 12-μm breach by 6.9-MPa argon pressure and (b) breach location within area of surface flat.

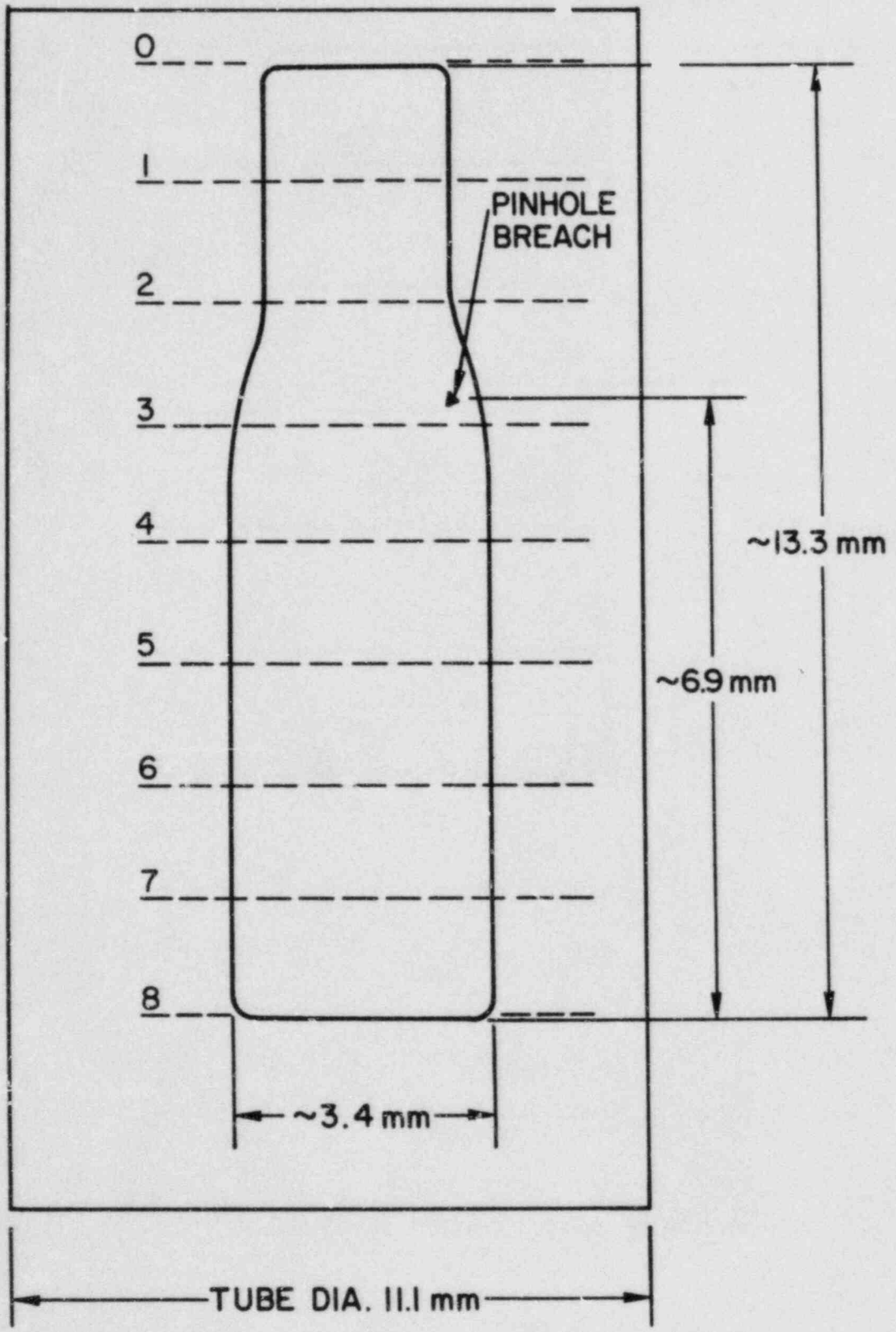

Fig. 3.11. Schematic Showing Location of Pinhole Breach within Flat Surface Region of Specimen 217K2G.

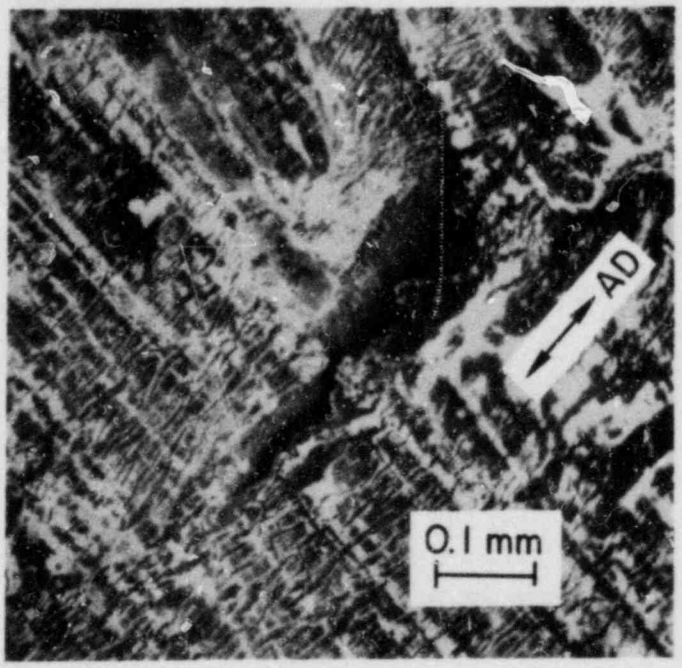

Fig. 3.12. SEM Photograph of the Pinhole Breach Shown in Fig. 3.10(A).

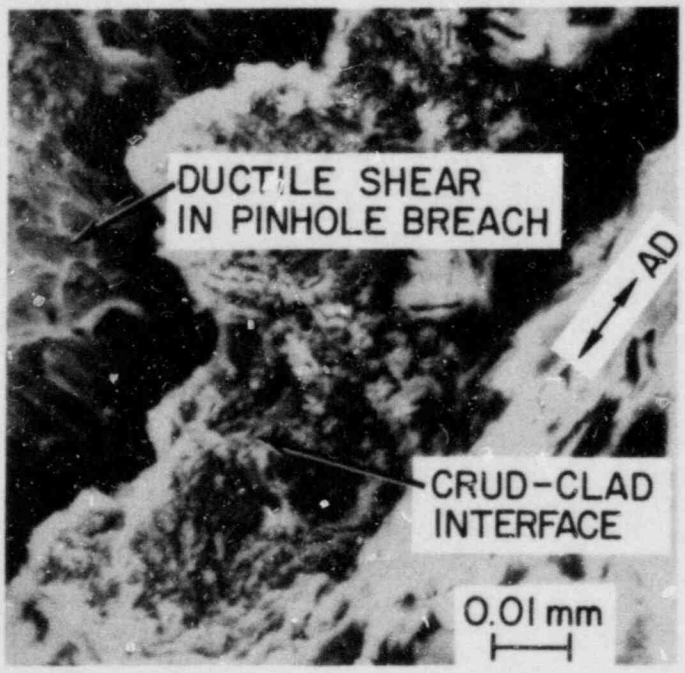

Fig. 3.13. Morphology of the Crud-Cladding Interface Adjacent to the Pinhole Breach in Specimen 217K2G.

The inner surface of specimen 217K2G opposite the surface flat is shown at high magnification in Fig. 3.14. For convenience of presentation, only a narrow strip from the original micrograph is shown. The numbers at the bottom of Fig. 3.14 correspond to the dashed lines in Fig. 3.11. The axial cracks appear to originate in sec. 2, near the upper end of the flat (see Fig. 3.11), perpendicular to the inner surface. The cracks increase dramatically in number and size in sec. 3, begin decreasing in size and number in sec. 5, and are almost totally absent in secs. 7 and 8 at the lower end of the flat. The only inner-surface crack to propagate to the outer surface is identified in sec. 4 of Fig. 3.14, and is shown at high magnification in Fig. 3.15. The fracture surface in Fig. 3.15 has the flat and featureless appearance of brittle cleavage at a depth significantly below the inner surface. All of the remaining cracks shown in Fig. 3.14 are partial cracks of varying depths. The partial crack identified in Fig. 3.14 adjacent to the through-wall crack is shown at high magnification in Fig. 3.16. The features of the fracture surface are brittle and microcracks are present at the bottom of the larger crack.

Figure 3.17 shows a 6.4-mm-diameter disk that was ultrasonically excised[10] from the specimen, which contains the pinhole breach shown in Figs. 3.10 and 3.12. The pinhole is located at the point of intersection of the horizontal and vertical marks. The two cutouts at opposite ends of the disk represent 3-mm-diameter samples that were removed for TEM examination. The disk sample in Fig. 3.17 will be fractured (opened) across the pinhole breach at liquid nitrogen temperature, and the through-wall fracture surface will be examined by SEM.

The fracture characteristics described above in association with Figs. 3.10 to 3.17 confirm that the crack in this specimen initiated on the inner surface and propagated toward the oxide-free zone of the outer surface. This is in contrast to the fracture behavior of all specimens tested by internal gas pressurization without removal of the outer-surface oxide layer. The meaning of this has been discussed in a previous report.[4]

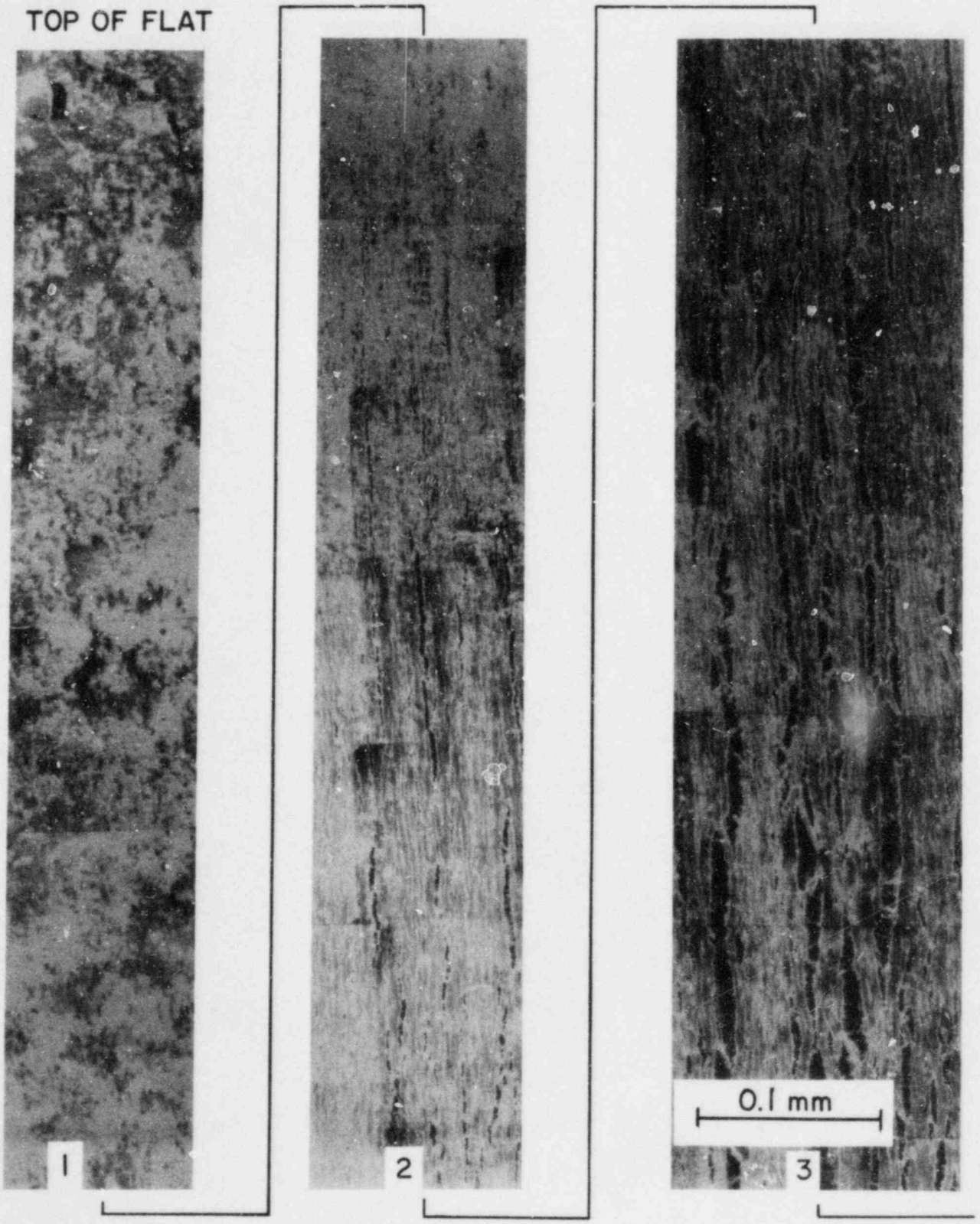

Fig. 3.14. SEM Photograph of the Inner Surface of Specimen 217K2G, Showing Cracks Parallel to Axial Direction in Regions 1 to 8 (see Fig. 3.11).

Fig. 3.14. (Contd.)

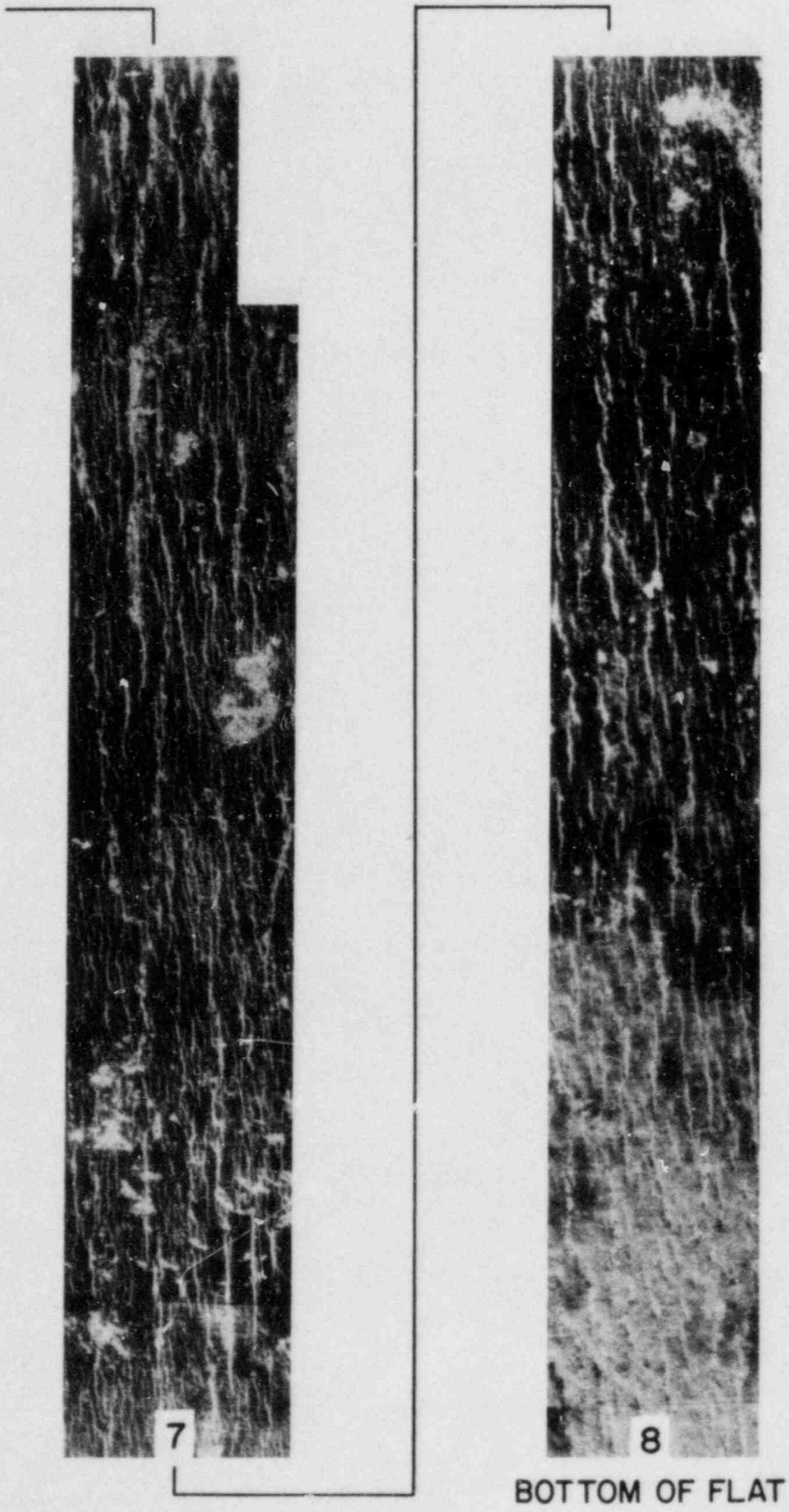

Fig. 3.14. (Contd.)

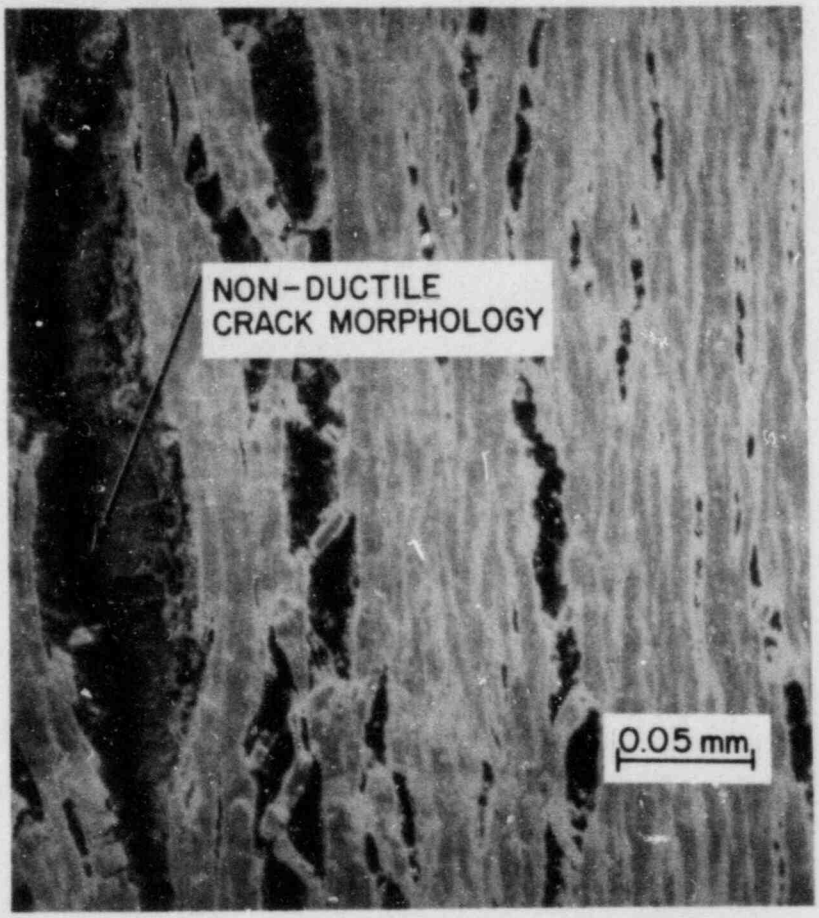

Fig. 3.15. SEM Photograph Showing Non-Ductile Fractographic Features of the Through-Wall Pinhole Breach Indicated in Fig. 3.14.

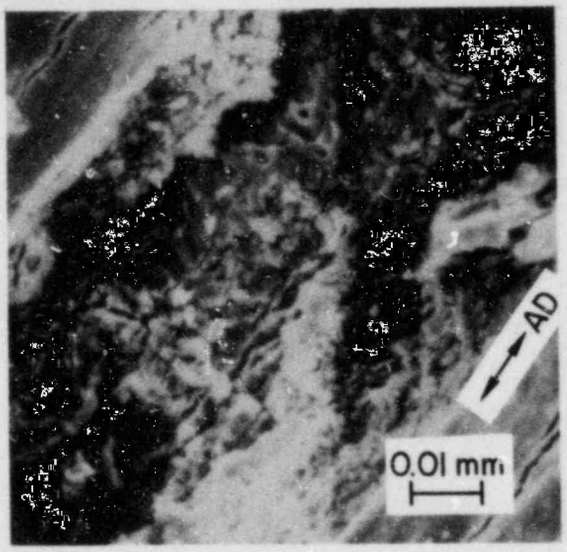

Fig. 3.16. SEM Photograph Showing the Brittle Fractographic Features of the Partial Crack Indicated in Fig. 3.14.

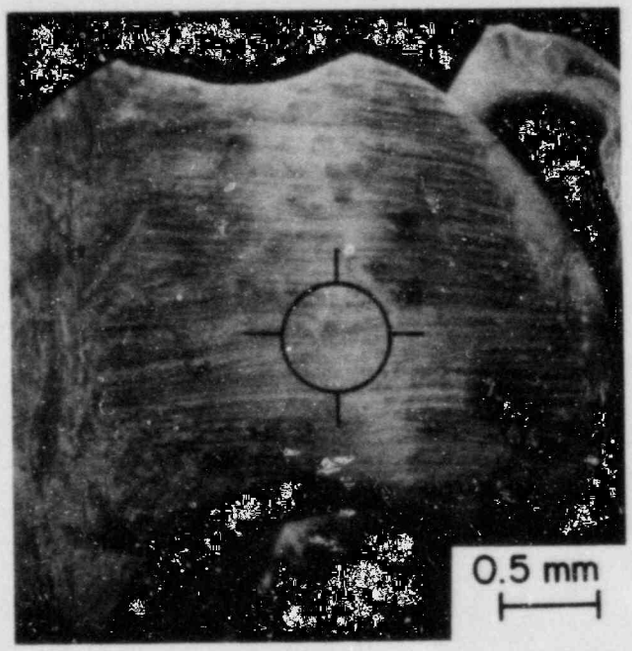

Fig. 3.17. Ultrasonically Cored 6.4-mm-diameter Disk Containing the Pinhole Failure Shown in Figs. 3.10(A) and 3.12. Crack located at intersection of horizontal and vertical marks.

D. Mandrel Tests on Irradiated Zircaloy Cladding (F. L. Yaggee)

In previously reported mandrel tests,[11] it was determined that the (split) hardened-steel ring used to load the specimen internally began yielding at high strains (mandrel loads) on the specimen. This occurred when the unsupported length of the loading ring increased significantly as the slot width of the supporting expanding sleeve increased by more than 50%. The estimated 0.1-mm inward creep of the steel loading ring significantly decreased the coefficient of friction at the ring cladding interface and had an adverse effect on the useful strain range of the mandrel assembly. The combination of initial specimen ovality and possible inward creep of the loading ring raised doubt that a PCI-type failure of the specimen could be detected unambiguously from the mandrel loading curve. Also, the decrease in specimen length that occurred during deformation was in good agreement with predictions based on the measured diametral strain in the absence of axial constraint of the freestanding specimen. Several procedural changes were incorporated into the mandrel tests. A higher strength tungsten-rhenium (W-Re) loading ring replaced the hardened steel ring, and a low-volume (<15 cm^3) high-pressure (13.8 MPa) helium system was assembled to detect the location and determine the size of the pinhole fracture at the end of the test.

Six mandrel tests were conducted on irradiated Zircaloy cladding at 325°C in an argon gas environment. The gas flow rate was ~0.006 ℓ/s. In all mandrel tests, the slit in the metal loading ring was placed over a solid ligament of the slotted, expanding steel sleeve when the mandrel was inserted into the specimen. The test was assembled with the region of the specimen over the ring slit (the simulated pellet crack) oriented in a manner such that the probable failure site could be viewed during the test. The viewing direction was taken as the zero degree orientation and the azimuthal reference was used for documentation of PCI-type failures during subsequent specimen examination.

All of the PCI-type pinhole breaches listed in Table 3.2 were generated at an average specimen strain rate of $<5 \times 10^{-7}$ s^{-1}. A constant crosshead rate of 8×10^{-6} mm·s^{-1} generates a specimen strain rate of about 5.3×10^{-7} s^{-1}. It is likely that strain rates of $<3 \times 10^{-7}$ s^{-1} are conducive to

TABLE 3.2. Mandrel Expansion Tests on Zircaloy Spent-Fuel Cladding at 325°C

Specimen Number	Cladding Type[c]	Ovality, mm	Diametral Strain Rate, s^{-1}	Maximum Mandrel Load, kg	Azimuthal[a] Position of Failure Site, deg	Total Test Time, h	Diametral Strain at Outer Surface[b] Total,[c] %	Plastic, %
217K2C[d]	MY	0.017	3×10^{-7}	910	No Failure	60.1	7.4	6.8
217K2F[d]	MY	0.018	2×10^{-7}	850	No Failure	62.7	5.4	4.9
217A4C[e]	HBR	0.031	2×10^{-7}	459	0	68.1	5.1	4.7
217A4E[e]	HBR	0.029	7×10^{-8}	845	247	223.8	6.2	6.0
217A4F[e]	HBR	0.102	1×10^{-7}	740	90	91.5	4.8	4.7
217B2D[e]	HBR	0.062	7×10^{-8}	1016	0	237.8	6.8	6.1

[a]Orientation with respect to the zero-degree viewing direction.
[b]Total (elastic plus plastic) and plastic diametral strains determined with the mandrel in the specimen and after removal of the mandrel, respectively, based on micrometer measurements.
[c]MY and HBR refer to Maine Yankee and H. B. Robinson Zircaloy-4 fuel cladding, respectively. The nominal dimensions, burnup, fluence, and fission gas release are given in Table VII of Ref. 8.
[d]Mandrel tests with split hardened-steel rings to simulate pellet crack.
[e]Mandrel tests with split tungsten-rhenium rings to simulate pellet crack.

PCI-type failure in irradiated Zircaloy in the absence of fission products. The details of the test conditions for the specimens identified in Table 3.2 are as follows. Specimen 217K2C was loaded at a constant rate with dual (split) hardened steel rings (R_c = 45) for 21 h to an estimated diametral strain of 4%. After an overnight hold period at a constant mandrel load of 423 kg, the test was interrupted for specimen failure inspection. No indications of a PCI-type failure could be visually confirmed and the test was continued at a constant loading rate to the limit of the mandrel displacement range. At a mandrel load of 910 kg, the expanding steel sleeve had come in contact with the inner specimen surface. The test was terminated after a total time of about 60 h.

Maine Yankee specimen 217K2F was the last specimen to be loaded with dual (split) hardened-steel rings. This specimen was loaded at a constant rate for 48 h to a mandrel load of 850 kg, and held at this load overnight. No indication of specimen failure at the zero degree orientation could be detected visually when the test was terminated after about 63 h.

H. B. Robinson specimen 217A4C was the first of four similar specimens to be internally loaded with a split W-Re ring. This specimen was loaded at a constant rate for three incremental periods of about 15 to 18 h each. Each

continuous loading period was followed by a short period (~5 h) at constant loads of 250, 370, and 459 kg. No indications of PCI-type failures could be detected visually at diametral strains of 1.7 and 3.2%. At a diametral strain of 4.7%, a PCI-type failure was detected visually at the zero-degree orientation (i.e., at the simulated pellet crack).

H. B. Robinson specimens 217A4E, 217A4F, and 217B2D were each loaded with a split W-Re ring at a constant rate to the maximum mandrel load. During each test, a PCI-type failure at the zero-degree orientation could not be detected visually at the end of the loading period. In specimens 217A4E and 217B2D, indications of possible specimen failure at the zero-degree orientation were visually detected after an overnight hold period at the maximum mandrel load. In specimen 217A4F, no failure at the zero-degree orientation could be detected visually after a similar overnight hold period.

The surface condition of the H. B. Robinson specimens contributed to the problem of visual confirmation of PCI-type failure. Axial cracking of the surface crud layer began at about 1.5% diametral strain and was followed by circumferential cracking shortly thereafter. Shadows caused by inadequate lighting often made certain axial striations (surface scratches due to fuel element handling) appear as cladding failures, as did the cracks in the surface crud layer. It was concluded that pressurization of the specimens with argon or helium gas provided the only reliable detection technique for identifying cladding failure sites. A low-volume (<15 cm^3) system, capable of pressurization to >10 MPa, was developed for use with both the 152-mm-long biaxial specimens and the 51-mm-long open-end mandrel specimens. The pressurization was performed in situ in biaxial specimens and after the test in the mandrel specimens.

It was also determined that the small sawtooth-like changes in the mandrel loading curve were the result of lateral adjustments between the loading ring and the inner surface of the specimen as the mandrel load increased. These load adjustments were usually constant in frequency and magnitude, and typically greater than 15 to 20% of the instantaneous mandrel load. Somewhat larger load adjustments occurred immediately upon resumption of a constant-rate loading when the specimen had been held at constant load

overnight. This indicated that sufficient specimen creep had occurred during the hold period to lower the coefficient of friction at the interface between the loading ring and the specimen. The fact that in some instances a visual detection of failure could be made after an overnight hold period at constant load indicated that partial cracks propagated with the small creep strain.

Figures 3.18-21 show the strained region of specimen 217A4C at orientations of 0, 45, 90, 135, 180, 225, 270, and 315 degrees at a magnification of 10X. The slip lines seen above and below the point of maximum diametral strain show cusps at several of the azimuthal orientations, indicating points of high stress and strain localization. The pinhole breach at the zero-degree orientation in Fig. 3.18 is located at such a point, and the stress and strain localization is due to the slit in the W-Re loading ring, which simulates a fuel pellet crack. Similar strain cusps appear in all of the photographs in Figs. 3.18-21. At diametral strains above ~3.5-4.5%, the expanding sleeve assumes an octagonal shape which is impressed upon the specimen as shown in Fig. 3.22. The outer surface of the metal loading ring develops small cracks at some of the octagonal points and these cracks have the effect of a simulated fuel pellet crack. Thus, Fig. 3.21 shows what appears to be a PCI-type failure at the 315° orientation. The expanded W-Re loading ring was retained in specimen 217A4C after removal of the mandrel assembly as shown in Fig. 3.22 for specimen 217A4E. Specimen 217A4C cracked axially through the pinhole failure at the zero-degree orientation during an attempt to remove the expanded loading ring intact. The crack occurred at 25°C and extended over the entire specimen length. As a result, none of the PCI-type failures shown in Figs. 3.18-21 were confirmed as through-wall failures by helium pressure tests. It is expected that an SEM examination will confirm the size and depth of these apparent failures, and transverse metallographic sections will reveal the number, density, and depth of existing cracks at the point of maximum diametral strain in a selected section of the specimen.

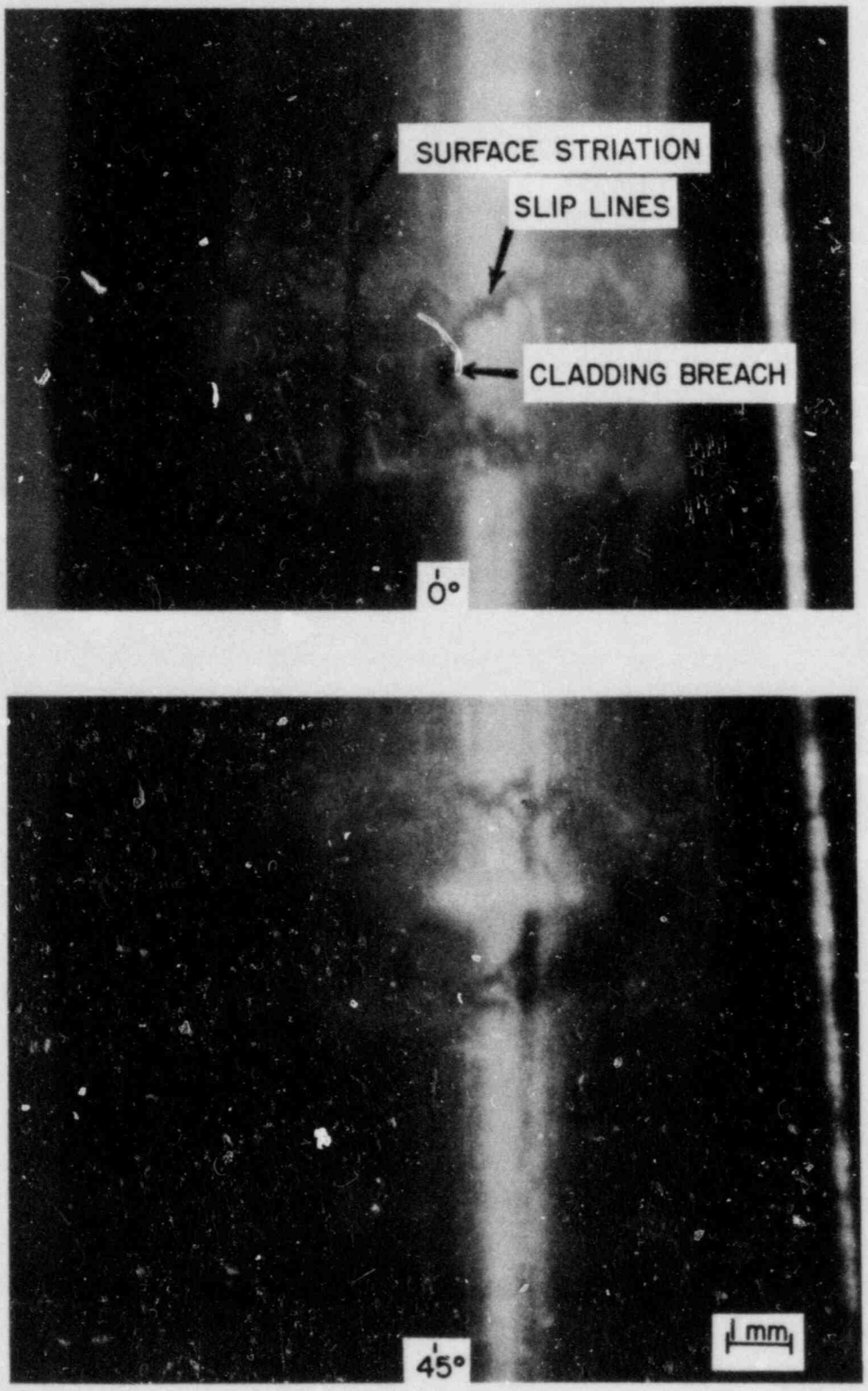

Fig. 3.18. Post-Test High-Magnification Photograph of H. B. Robinson Specimen 21/A4C at 0 and 45° Orientations.

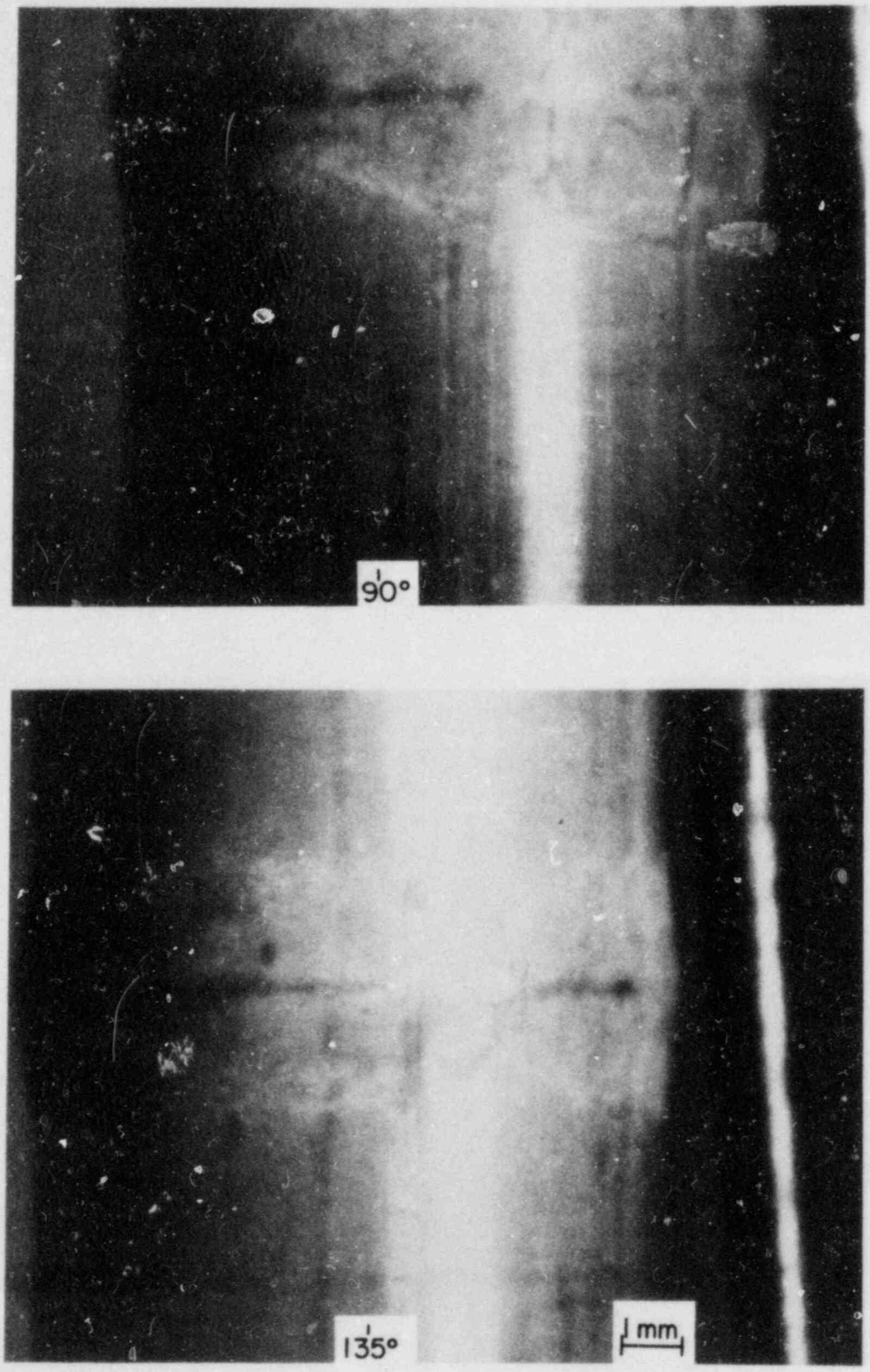

Fig. 3.19. Post-Test High-Magnification Photograph of H. B. Robinson Specimen 217A4C at 90 and 135° Orientations.

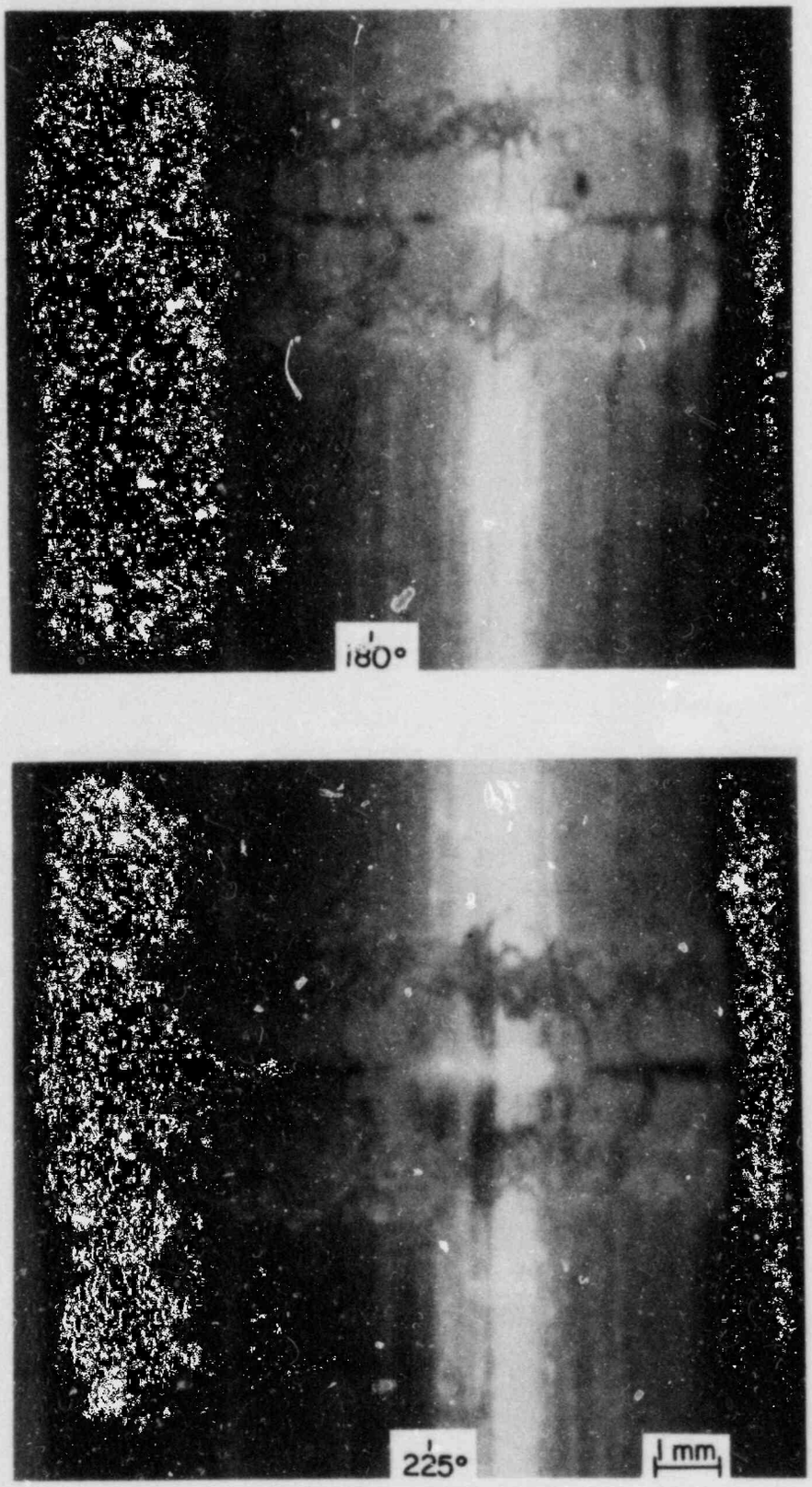

Fig. 3.20. Post-Test High-Magnification Photographs of H. B. Robinson Specimen 217A4C at 180 and 225° Orientations.

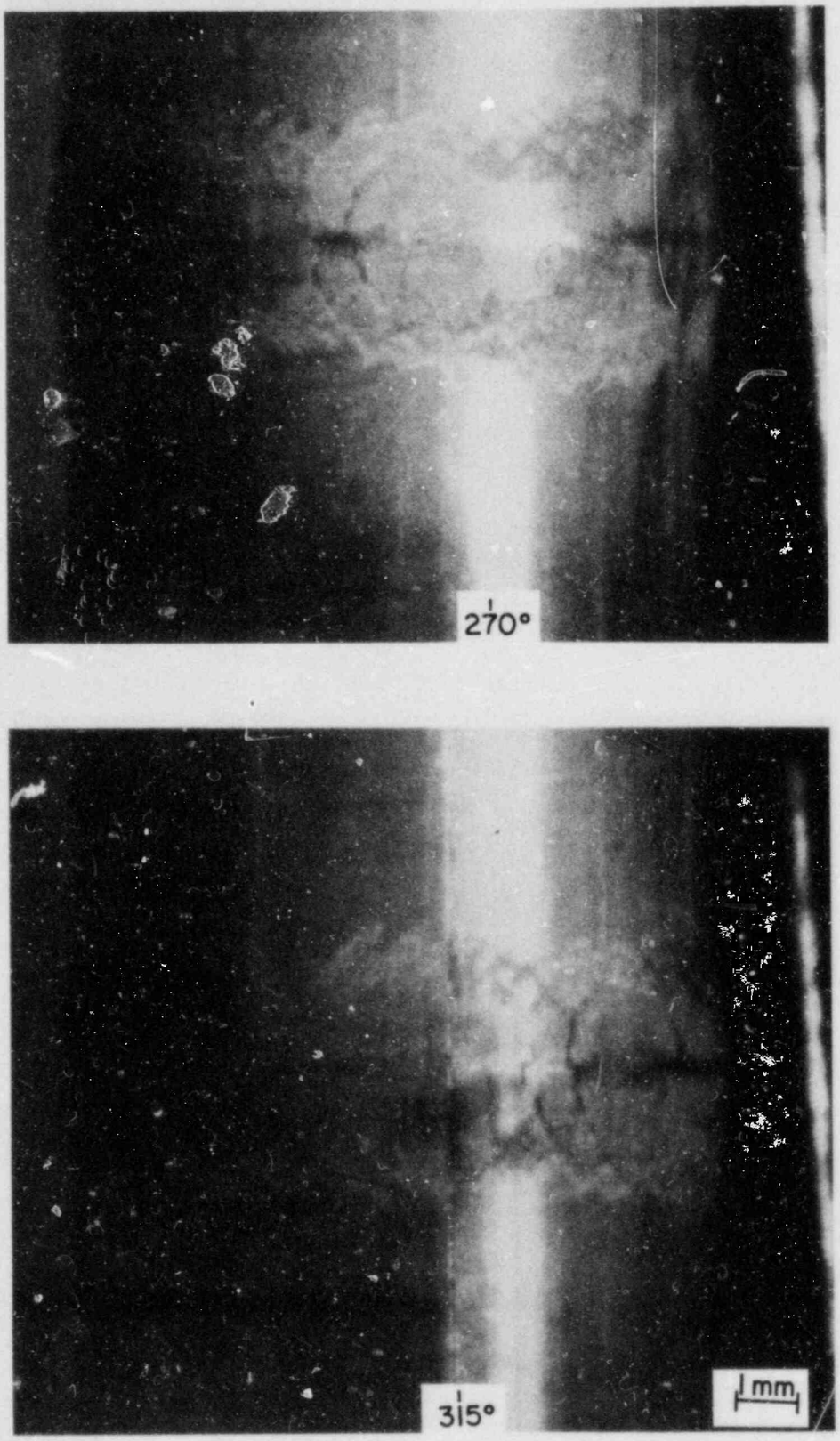

Fig. 3.21. Post-Test High-Magnification Photograph of H. B. Robinson Specimen 217A4C at 270 and 315° Orientations.

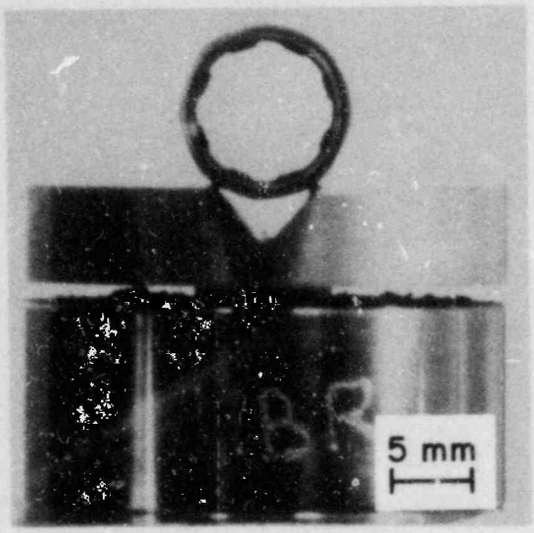

Fig. 3.22.
Expanded W-Re Loading Ring in H. B. Robinson Specimen 217A4E with Slit in Ring at Bottom.

Figures 3.23-28 are photographs of specimen 217A4E, at low and high magnification, showing apparent PCI-type failures at orientations of 0, 45, and 247°. The PCI-type failure shown at the 247° orientation in Figs. 3.27 and 3.28 was confirmed as a through-wall failure in helium leak tests at 6.9 MPa pressure. The effective orifice diameter of the crack was determined to be about 6 μm. The apparent PCI-type failures shown in Figs. 3.23-26 are assumed to be partial cracks. The 6-μm pinhole breach at the 247° orientation is shown in Fig. 3.29 as a spot of white foam, caused by a bubble-by-bubble leak rate.

Figure 3.30(A) is a low-magnification photograph of specimen 217B2D with an apparent PCI-type failure at the zero-degree orientation. The through-wall nature of this failure was confirmed by a helium leak test at a pressure of 6.9 MPa [Fig. 3.30(B)]. The effective orifice diameter of the pinhole leak was 8 μm.

Future tests on irradiated H. B. Robinson cladding will employ mandrel loading and axial constraint of the specimen. It is expected that tests with axial constraint will generate PCI-type pinhole failures at diametral strains of <1%. Hardware for these tests is currently being made.

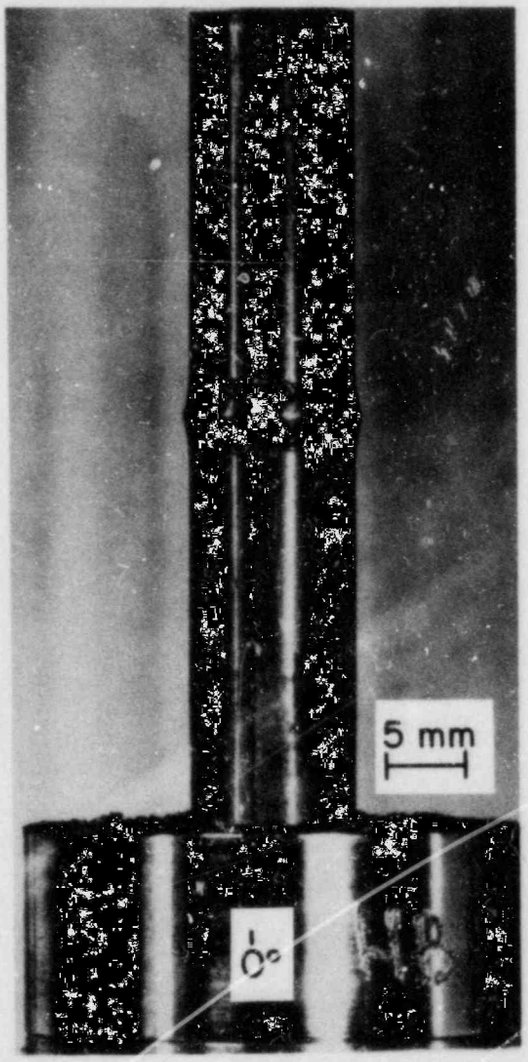

Fig. 3.23. Post-Test Low-Magnification Photograph of H. B. Robinson Specimen 217A4E Showing Apparent Pinhole Failure at Zero-Degree Orientation.

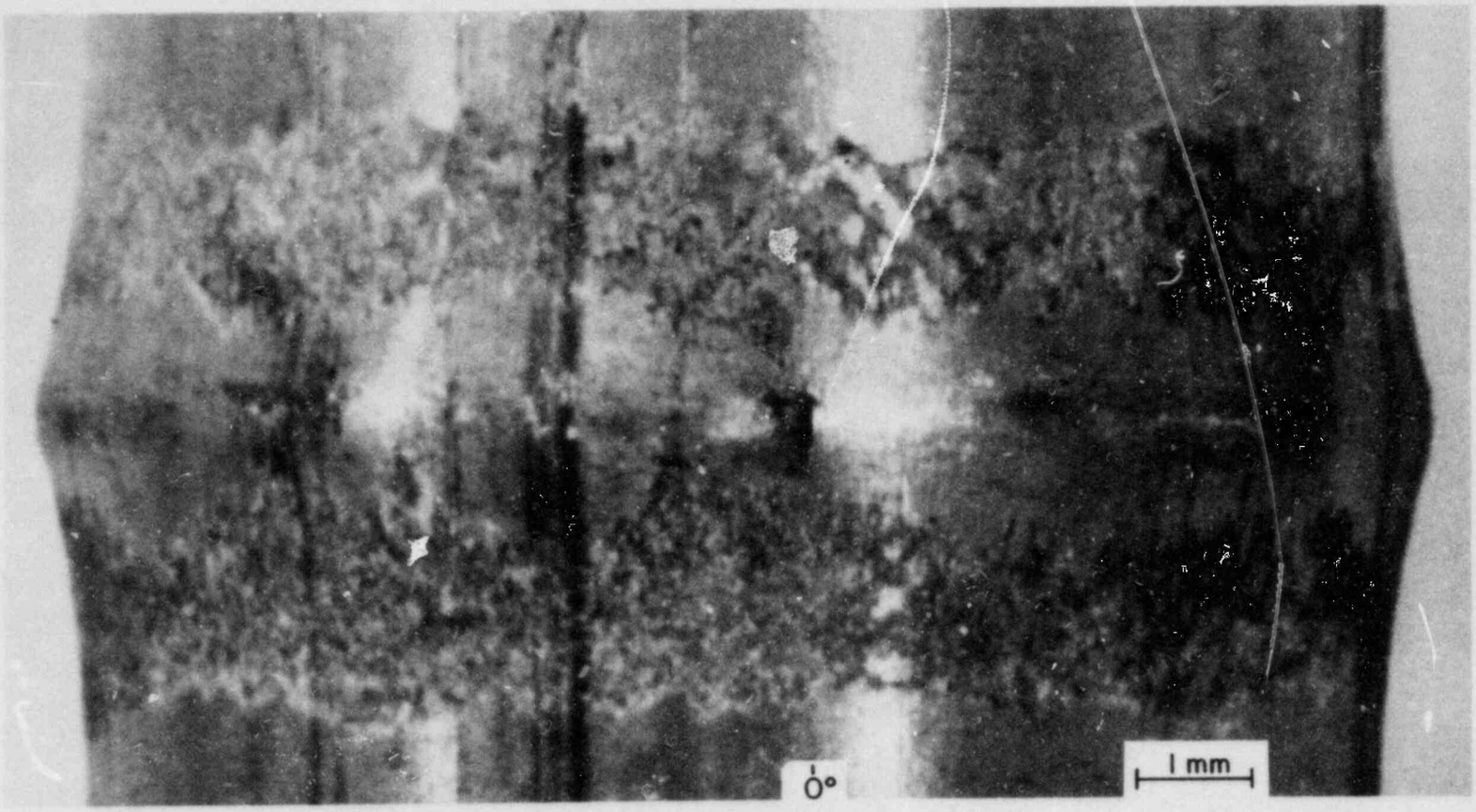

Fig. 3.24. Post-Test High-Magnification Photograph of H. B. Robinson Specimen 217A4E Showing Apparent Pinhole Failure at Zero Degree Orientation.

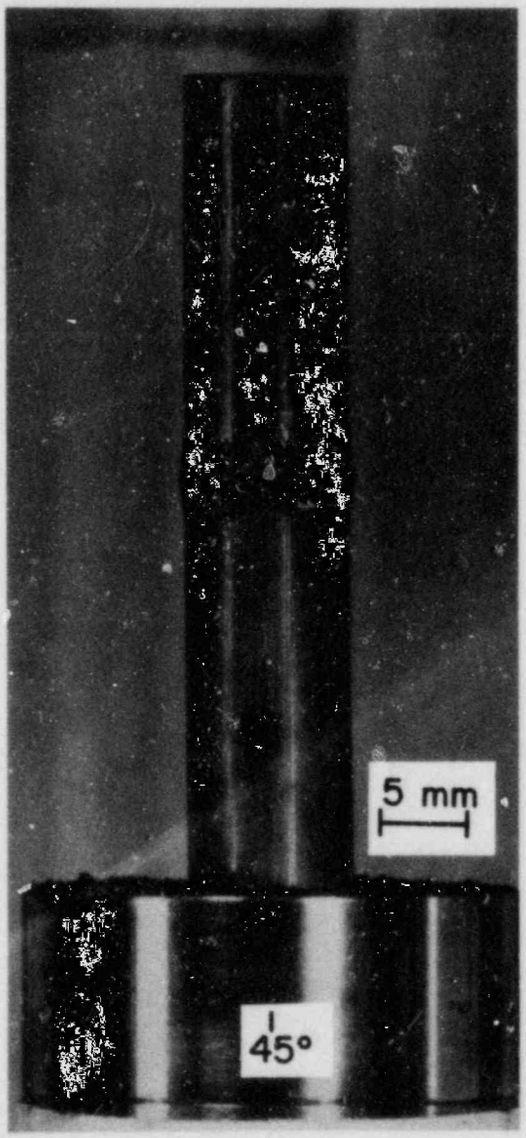

Fig. 3.25. Post-Test Low-Magnification Photograph of H. B. Robinson Specimen 217A4E Showing Apparent Pinhole Failure at 45° Orientation.

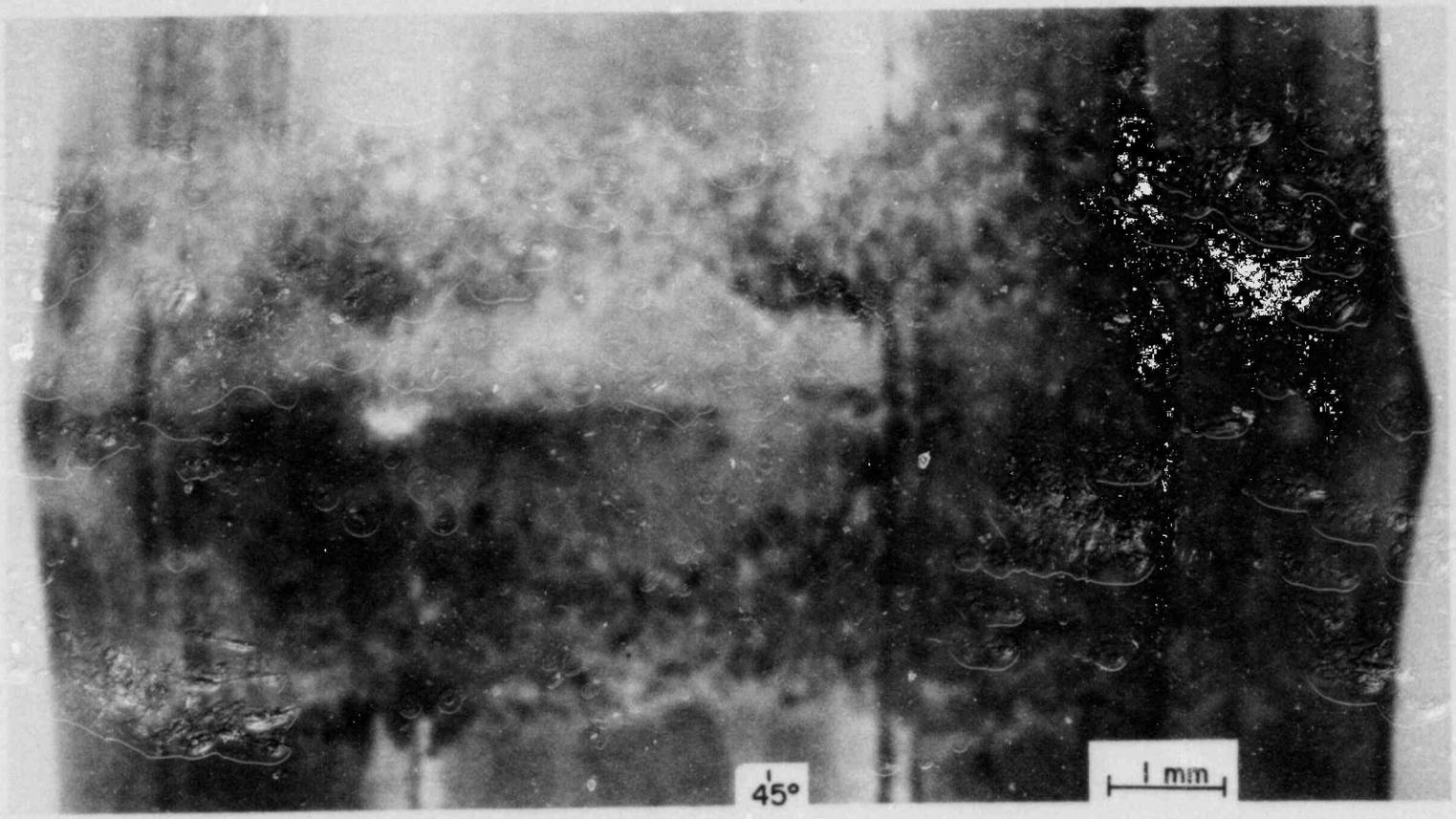

Fig. 3.26. Post-Test High-Magnification Photograph of H. B. Robinson Specimen 217A4E Showing Apparent Pinhole Failure at 45° Orientation.

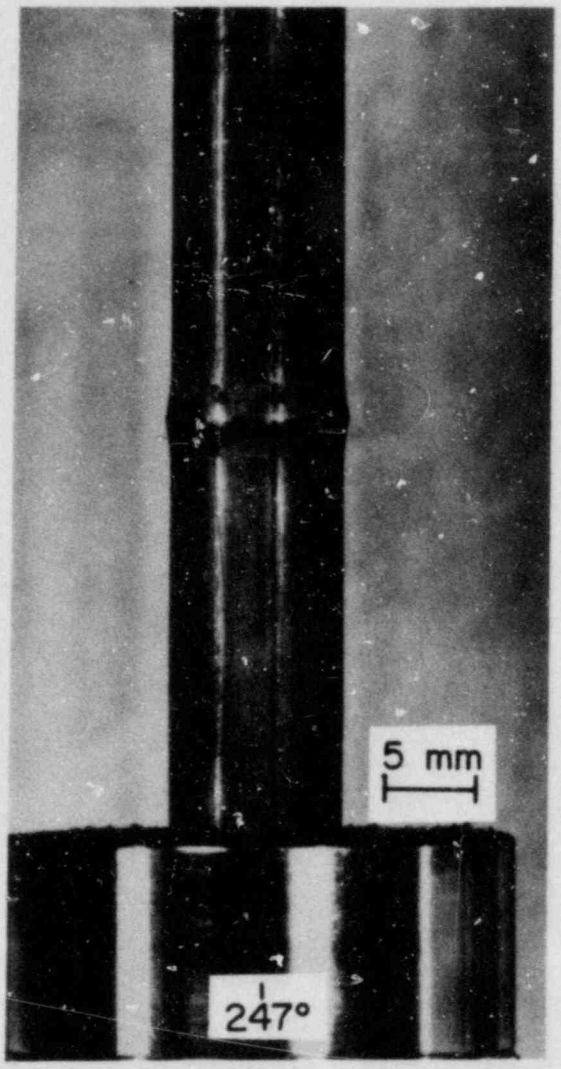

Fig. 3.27. Post-Test Low-Magnification Photograph of H. B. Robinson Specimen 217A4E Showing Apparent Pinhole Failure at 247° Orientation.

Fig. 3.28. Post-Test High-Magnification Photograph of H. B. Robinson Specimen 217A4E Showing Apparent Pinhole Failure at 247° Orientation.

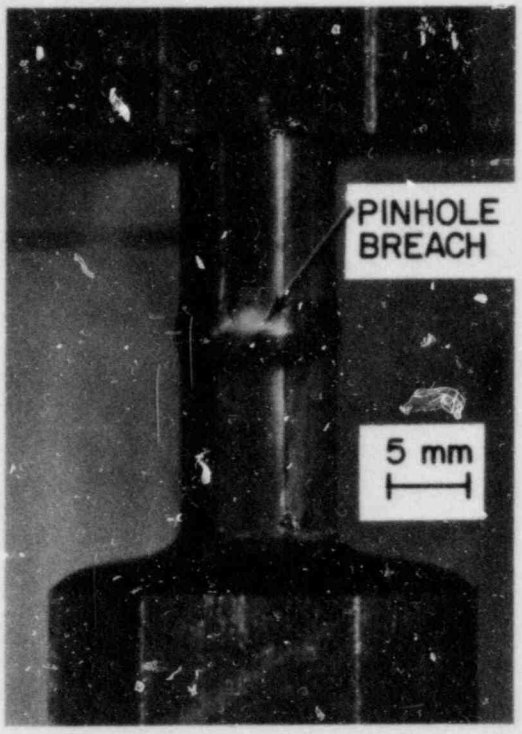

Fig. 3.29. Pinhole Leak Indication in H. B. Robinson Specimen 217A4E at the 247° Orientation. Helium pressure 6.9 MPa.

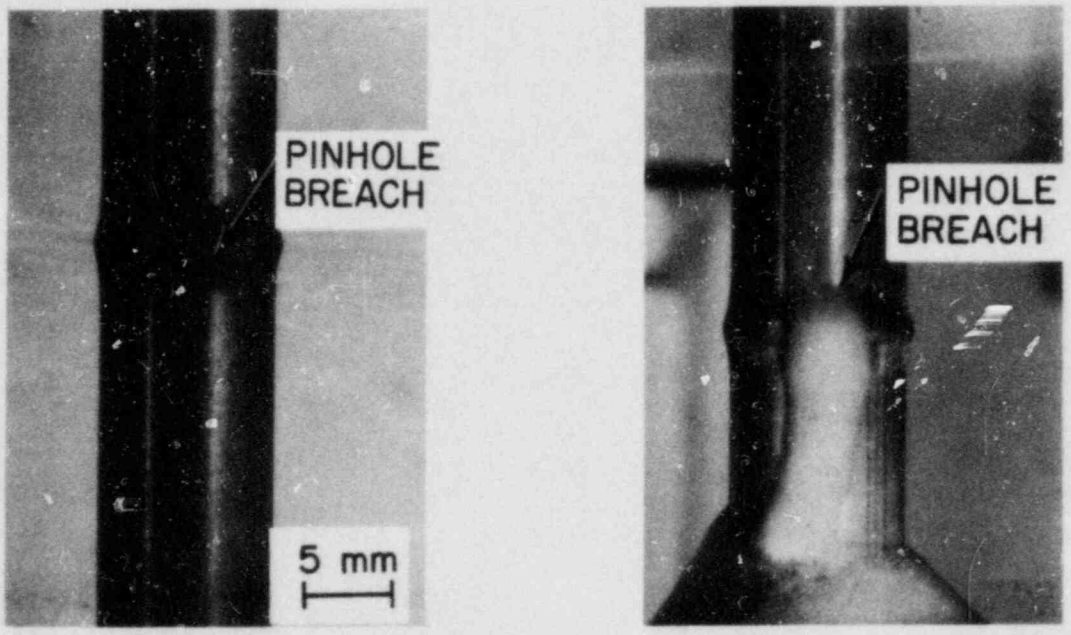

Fig. 3.30. Pinhole Failure in H. B. Robinson Specimen 217B2D (a) Before Leak Testing and (b) During Leak Testing at 6.9 MPa Helium Pressure.

E. References for Chapter III

1. H. M. Chung, in Materials Science Division Light-Water-Reactor Safety Research Program: Quarterly Progress Report, April-June 1982, NUREG/CR-2970 Vol. II, ANL-82-41 Vol. II (April 1983), pp. 72-78.

2. H. M. Chung, in Materials Science and Technology Division Light-Water-Reactor Safety Research Program: Quarterly Progress Report, October-December 1982, NUREG/CR-2970 Vol. IV, ANL-82-41 Vol. IV (November 1983), pp. 82-98.

3. H. M. Chung, in Materials Science and Technology Division Light-Water-Reactor Safety Research Program: Quarterly Progress Report, January-March 1983, NUREG/CR-3689 Vol. I, ANL-83-85 Vol. I (April 1984), pp. 121-135.

4. H. M. Chung, "TEM-HVEM Observation of Ordered Zirconium-Oxygen Phase in Zircaloy Spent-Fuel Cladding," in Proc. Intl. Symp. on Environmental Degradation of Materials in Nuclear Power Systems-Water Reactors, Myrtle Beach, SC, August 22-24, 1983 (in press).

5. F. L. Yaggee, in Materials Science Division Light-Water-Reactor Safety Research Program: Quarterly Progress Report, April-June 1982, NUREG/CR-2970 Vol. II, ANL-82-41 Vol. II (April 1983), pp. 79-100.

6. H. M. Chung, in Materials Science Division Light-Water-Reactor Safety Research Program: Quarterly Progress Report, July-September 1982, NUREG/CR-2970 Vol. III, ANL-82-41 Vol. III (August 1983), pp. 21-37.

7. H. S. Rosenbaum, U. E. Wolff, and W. L. Bell, "Fractography of Incipient Cracks on Rod KE-2225," in Determination and Microscopic Study on Incipient Defects in Irradiated Power Reactor Fuel Rods, EPRI NP-812 (July 1978), pp. 3-97 to 3-141.

8. F. L. Yaggee, in Light-Water Reactor Safety Research Program: Quarterly Progress Report, July-September 1981, NUREG/CR-2437 Vol. III, ANL-81-77 Vol. III, p. 52.

9. H. M. Chung and F. L. Yaggee, in Materials Science and Technology Division Light-Water-Reactor Safety Research Program: Quarterly Progress Report, January-March 1983, NUREG/CR-3689 Vol. I, ANL-83-85 Vol. I (April 1984), pp. 112-121.

10. F. L. Yaggee, "An SEM-TEM Sampling Technique for Use with Fueled LWR Cladding," Trans. Amer. Nucl. Soc. 41, 248 (1982).

11. F. L. Yaggee, in Materials Science Division Light-Water-Reactor Safety Research Program: Quarterly Progress Report, April-June 1982, NUREG/CR-2970 Vol. II, ANL-82-41 Vol. II (April 1983), pp. 79-96.

IV. LONG-TERM EMBRITTLEMENT OF CAST DUPLEX STAINLESS STEELS IN LWR SYSTEMS

Principal Investigators:
O. K. Chopra and G. Ayrault

Recent investigations of the aging behavior of ASTM A-351 grades CF-8 and -8M cast duplex stainless steels show substantial reductions in room-temperature impact strength after 10,000 to 70,000 h of exposure to temperatures as low as 300°C.[1-5] The ferrite content of the cast structure has a pronounced influence on the embrittlement behavior, viz., an increase in ferrite content increases the susceptibility to embrittlement. Also, addition of molybdenum to the steel, e.g., cast CF-8M, increases both the rate and extent of embrittlement. The very limited data available on J_{IC} fracture toughness also indicate significant reduction in fracture toughness due to low-temperature aging,[4,5] although the results do not always show good correlation with the trends indicated by the Charpy data.

At temperatures below 500°C, embrittlement of the duplex stainless steels is attributed to precipitation of the α' phase in the iron-rich α matrix. The kinetics of embrittlement are evaluated by assuming that the aging phenomenon is a thermally activated process which can be expressed by an Arrhenius relation. The activation energy is determined by examining the degree of embrittlement (e.g., Charpy impact strength measured at room temperature) produced by different time/temperature histories. In the temperature range of 300 to 400°C, the data obtained by George Fisher, Ltd. of Switzerland[2] for thermal aging of various cast duplex stainless steels yield an activation energy of 100.4 kJ/mole (24,000 cal/mole) for the onset of embrittlement. Arrhenius extrapolation of the data can be used to determine the time for onset of embrittlement at reactor operating temperatures:

$$t = 10^{P} \exp\left(\frac{U}{R}\frac{1}{T} - \frac{1}{673}\right), \qquad (4.1)$$

where U is the activation energy, R the gas constant, T the absolute temperature, and P represents the degree of aging reached after 10^{P} h at 400°C. For example, a service life of 40 yr at 288 or 316°C is equivalent to 10,000 or 28,000 h of aging at 400°C, respectively.

Recent investigations[5] have described the activation energy for the process of embrittlement as a function of chemical composition of the cast material, given by the relationship

$$Q(\text{kJ/mole}) = -182.6 + 19.9(\%\ \text{Si}) + 11.08(\%\ \text{Cr}) + 14.4(\%\ \text{Mo}). \qquad (4.2)$$

The chemical compositions of the various cast materials used by George Fisher, Ltd. yield activation energies between 65 and 90 kJ/mole (~15 and 22 kcal/mole) for cast CF-8 stainless steels and between 75 and 105 kJ/mole (~18 and 25 kcal/mole) for cast CF-8M stainless steel.

A satisfactory understanding of the aging process and the mechanism of embrittlement is required to ensure that the activation energy obtained from the laboratory tests is representative of the actual process. The value of activation energy as determined from the aging data for cast duplex stainless steels is much lower than that expected for a mechanism controlled by solute bulk diffusion (i.e., activation energy of 54,900 cal/mole). These results indicate that the precipitation of the α' phase occurs not via nucleation and growth but by another mechanism, e.g., spinodal decomposition, or that processes other than α' precipitation contribute to embrittlement. The available information on the microstructure of aged cast duplex stainless steels is not sufficient for correlating the microstructure with the mechanical properties or for determining the mechanism of low-temperature embrittlement.

The objectives of this program are to (1) characterize and correlate the microstructure of in-service reactor components and laboratory-aged material with loss of fracture toughness and identify the mechanism of embrittlement, (2) determine the validity of laboratory-induced embrittlement data for predicting the toughness of component materials after long-term aging at reactor operating temperatures, (3) characterize the loss of fracture toughness in terms of fracture mechanics parameters in order to provide the data needed to assess the safety significance of embrittlement, and (4) provide additional understanding of the effects of key compositional and metallurgical variables on the kinetics and degree of embrittlement.

A. Material Procurement

Nineteen different heats of cast stainless steel, ASTM A351 grades CF-8, -8M, and -3, have been obtained in the form of keel blocks. The composition of the heats was varied to provide different concentrations of nickel, chromium, carbon, and nitrogen in the material and ferrite contents in the range of 3 to 30%. Sections from five different centrifugally cast pipes (grades CF-8 and -8M), a pump impeller, and a pump casing (grade CF-8) were also procured. The commercial castings provide a range of chemical compositions, microstructure, and ferrite content, as well as cast shapes and sizes. The product form and chemical composition of the different cast materials are given in Table 4.1. Mechanical testing will focus on materials obtained from the reactor components. The experimental heats will be used to investigate the influence of the compositional and metallurgical variables on the long-term aging of cast stainless steels.

Charpy-impact specimen blanks have been obtained from keel blocks of the experimental heats and material from five reactor components (four centrifugally cast pipes and the static cast pump casing ring). Blanks for 1-T compact-tension specimens were obtained from sections of two cast pipes and the static cast pump casing. Detailed drawings and a schedule were prepared for cutting the various sections of cast components and keel blocks. Each specimen blank was identified relative to the location and orientation of the material in the keel blocks and cast components. The orientation and location of the Charpy-impact and compact-tension specimen blanks are shown in Figs. 4.1-3. Specimen blanks are also being prepared from cast material from the pump impeller. The specimen blanks will be aged at 450, 400, 350, 320, and 290°C for various lengths of time. The temperature and time of aging for the various specimens are given in Table 4.2. The final test specimens will be machined after the aging treatment. The orientation of the crack plane for the Charpy-impact and compact-tension specimens prepared from the reactor

TABLE 4.1. Product Form and Chemical Composition of the Cast Stainless Steel

Heat	OD (m)	Wall Thickness (mm)	Casting Process	Specification	Grade	Composition[a] (wt %) Mn	Si	Mo	Cr	Ni	N	C	Ferrite Content[b] (%)
58	Keel block[c]		Static	A351	CF-8	0.66	1.21	0.29	19.56	10.37	0.040	0.05	4.5
57						0.69	1.24	0.28	18.45	8.94	0.041	0.06	4.7
54						0.58	1.08	0.31	19.42	8.91	0.073	0.065	5.3
53						0.70	1.28	0.35	19.62	8.86	0.045	0.07	7.8
56						0.60	1.16	0.30	19.33	8.93	0.031	0.06	8.1
59						0.63	1.14	0.26	20.35	8.95	0.040	0.07	9.9
61						0.70	1.20	0.27	20.54	8.59	0.060	0.06	12.1
60						0.71	1.01	0.26	21.02	8.07	0.050	0.07	16.9
50					CF-3	0.67	1.26	0.28	17.63	8.84	0.064	0.019	4.4
49						0.66	1.11	0.29	19.32	10.10	0.064	0.022	5.1
48						0.67	1.21	0.26	19.42	9.90	0.071	0.016	6.0
47						0.65	1.23	0.45	19.67	10.04	0.027	0.018	10.2
52						0.63	1.04	0.31	19.51	9.07	0.049	0.021	10.9
51						0.66	1.06	0.28	20.36	8.69	0.048	0.023	17.5
62					CF-8M	0.84	0.64	2.46	18.38	11.35	0.030	0.07	4.2
63						0.69	0.75	2.52	19.39	11.22	0.030	0.05	9.1
66						0.71	0.60	2.36	19.41	9.13	0.030	0.06	17.9
65						0.66	0.63	2.53	20.95	9.39	0.060	0.06	22.3
64						0.70	0.71	2.41	20.87	9.01	0.030	0.05	32.2
P3	0.58	51.6	Centr.	A451	CF-8	1.13	0.91	0.01	19.05	8.94	0.21	0.033	1.7
C1	0.60	57.1	Static	A351	CF-8	1.13	1.08	-	19.30	8.90	-	0.06	4.0[d]
P1	0.89	63.5	Centr.	A451	CF-8	-	-	-	-	-	-	-	24.0[d]
P2	0.93	73.0	Centr.	A451	CF-3	0.83	1.02	0.11	20.09	9.64	-	0.027	14.0[d]
P4	0.58	31.8	Centr.	A451	CF-8M	1.12	1.00	2.37	20.20	10.22	0.17	0.044	6.5

[a]Chemical composition supplied by the vendor.
[b]Calculated from the composition using Hull's equivalent factor.
[c]Keel blocks approximately 203 mm long x 127 mm high and third dimension tapered from 63 to 36 mm.
[d]Measured values.

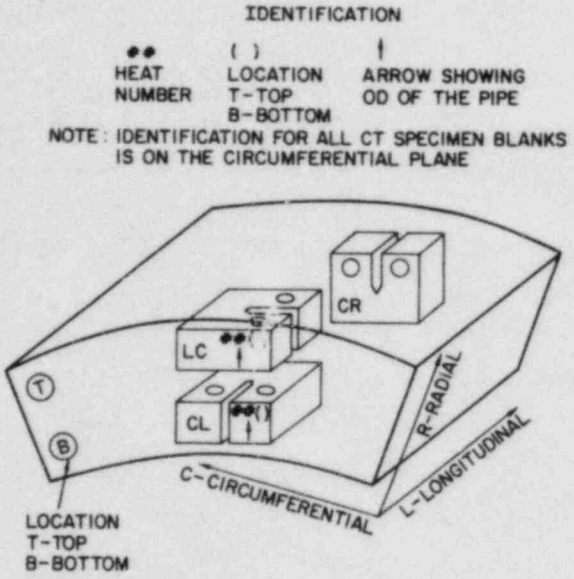

Fig. 4.1. Orientations of Compact Tension Specimens in Pipe Material.

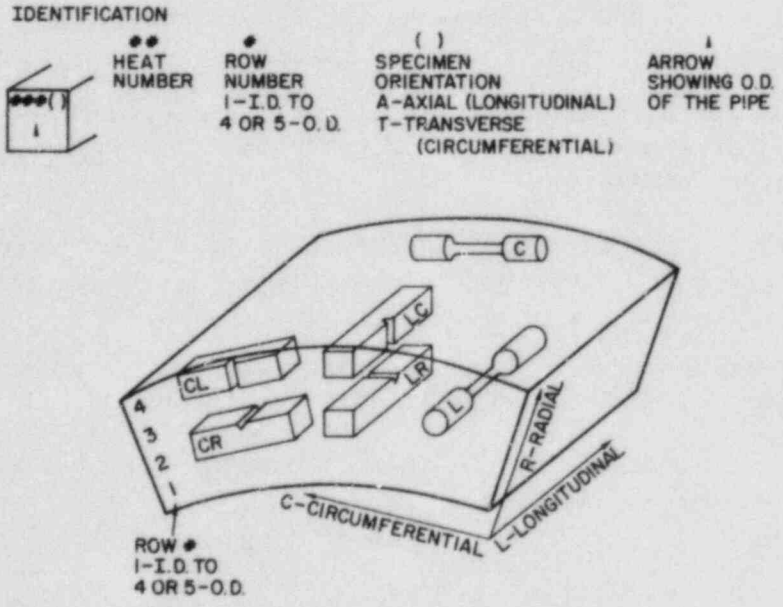

Fig. 4.2. Orientations of Charpy Impact and Tensile Specimens in Pipe Material.

TABLE 4.2. Time and Temperature for Aging of the Cast Material for Charpy Impact and J-Integral Tests

Time (h) \ Temp. (°C)	450	400	350	320	290
100	a	a			
300	a	a	a		
1,000	a	a	a	a	
3,000	a	a	a,b	a	a
10,000	a	a,b	a,b,c	a,b	a
30,000	a	a	a,b,c	a,b,c	a,b,c
>50,000		a	a	a,b	a,b

[a]Charpy-impact test at room temperature. Experimental heats: 3 specimens each condition; reactor components: 3 axial (L-C) and 2 transverse (C-L) specimens each condition.

[b]Instrument Charpy-impact test at room temperature. Experimental heats and reactor components: 2 specimens (L-C) each condition.

J-Integral test at room temperature. Reactor components: 2 L-C and 1 C-L specimens each condition.

[c]Charpy-impact test at 7 temperatures (DBTT). Reactor components: 14 L-C specimens each condition.

J-integral test at 290°C. Reactor components: 2 L-C specimens each condition.

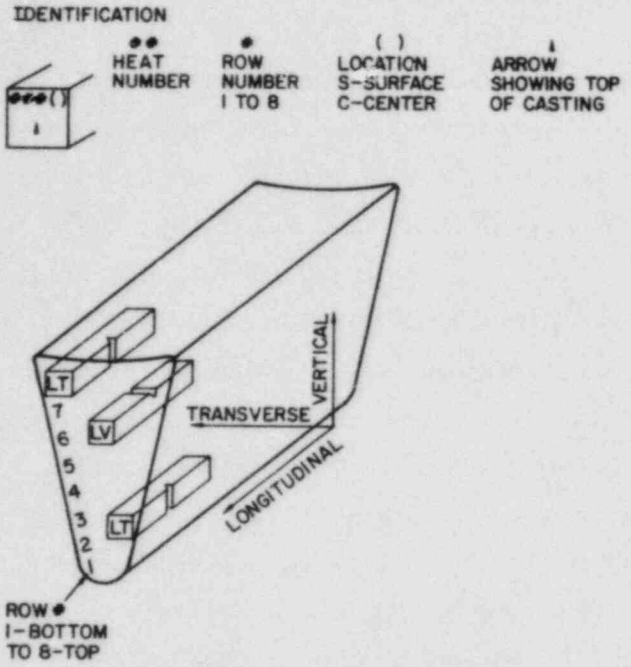

Fig. 4.3. Orientations of Charpy Impact Specimens in Cast Keel Blocks.

components will be L-C as well as C-L.* A few specimens will also be tested in the C-R orientation.

The various cast materials are being characterized to determine the chemical composition, ferrite content, hardness, and grain structure. A ferrite scope (Auto Test FE, Probe Type FSP-1) was procured to measure the ferrite content of the different castings. The instrument will be calibrated using secondary weld-metal standards obtained from the British Welding Institute. The ferrite contents of the weld-metal standards range from ferrite number 2.3 to 28.1.

*L = longitudinal direction of the cast pipe, C = circumferential direction, and R = radial direction. The first letter designates the direction normal to the crack plane and the second letter the expected direction of crack propagation.

B. Microstructural Evaluation

The initial experimental effort is focused on microstructural studies of aged cast stainless steels. Material from three heats of aged cast stainless steel, grades CF-8 and -8M, were obtained from George Fisher, Ltd. of Switzerland. The specimens from CF-8 steel (Heats 278 and 280) were aged for 3000, 10,000, and 70,000 h at 300, 350, and 400°C, while the specimens from CF-8M steel (Heat 286) were aged for 1000 and 10,000 h at 400°C. Two single-phase ferritic alloys, 26Cr-1Mo and 29Cr-4Mo-2Ni, and a cast stainless steel (Heat B) were used to develop the technique for preparing transmission electron microscope (TEM) foils from the bulk material. The ferritic alloys were supplied by Allegheny Ludlum Steel Corp., and have been used in a study of the "475°C embrittlement" phenomenon at temperatures between 371 and 593°C.[6] Specimens from the two ferritic alloys and cast stainless steel (Heat B) were aged for 100 and 1000 h at 400 and 475°C for TEM inspection.

Details of the specimen preparation technique and microstructural observation of the specimens aged for 1000 h at 400 and 475°C were reported earlier.[7] Aging of the two single-phase ferritic alloys produced the mottled bright-field images generally associated with α' precipitates. In addition, platelet precipitates were observed in the 29Cr-4Mo-2Ni alloy. These results for the ferritic alloys are essentially identical to those reported in an earlier study.[6] The diffraction pattern and the contrast images of the platelets suggest that they are not α'. Aging for 1000 h at 400°C produced no obvious microstructural change in the 26Cr-1Mo alloy. Platelet precipitates were observed in the 29Cr-4Mo-2Ni alloy.

The effort during the current reporting period was focused on TEM examination of aged cast duplex stainless steel. Aging of the cast CF-8 steel, Heat B, for 1000 h at 475°C produced two different types of precipitates in the ferrite grains: the mottled structure of the α' phase and another precipitate found only on dislocations. Neither of these precipitates were present in the unaged specimens. The mottled-contrast images seen in duplex stainless steel and a Fe-46Cr alloy have been shown (by Mossbauer spectroscopy[8] and precipitation extraction techniques,[9] respectively) to be due to α'. The precipitates formed on dislocations were typically 15- to

40-nm cubes with {100} matrix planes as faces. These precipitates were not α' and exhibited a distinct diffraction pattern consistent with a FCC structure similar to $M_{23}C_6$ patterns, but with a slightly larger lattice parameter. The precipitates also had a cube-on-cube orientation relative to the BCC ferrite matrix, which would be unusual for the $M_{23}C_6$ phase. Preliminary energy-dispersive x-ray analyses indicate an enrichment of Ni and Si in these precipitates.

TEM examination of the aged cast duplex stainless steel specimens obtained from George Fisher, Ltd. did not reveal the mottled images of α' precipitates. The CF-8 stainless steel, Heat 280 (containing 40% ferrite), aged for 66,650 h at 400°C, underwent profuse precipitation in the ferrite grains, both at and away from dislocations, as shown in the images in Fig. 4.4. These precipitates were similar to the $M_{23}C_6$-like precipitates observed in Heat B which was aged for 1000 h at 475°C. Precipitates that formed on the dislocations were about 15 nm in diameter and those away from dislocations were about 5 nm in size. The diffraction pattern indicates a FCC unit cell with a cube-on-cube orientation to the ferrite matrix. The precipitate unit cell is a factor of about 3.95 larger than that of the ferrite matrix. These precipitates were not present after aging for 10,000 h at 400°C. Another type of precipitate was observed on the dislocations, as shown in Fig. 4.5. The precipitate, however, could not be identified. The precipitate reflections were too weak owing to a low volume fraction and were streaked as a result of small size.

Examination of Heat 278 (containing 15% ferrite) of CF-8 cast stainless steel aged for about 70,000 h at 400°C also revealed the $M_{23}C_6$-like precipitates; however, their distribution was somewhat different than that in Heat 280. In Heat 278, the precipitates on dislocations tended to be larger whereas those away from dislocations were smaller. Furthermore, it was clear from diffraction pattern intensities of the precipitates that Heat 278 had a lower volume fraction of precipitates than Heat 280. Heat 278 was found to embrittle more slowly than Heat 280 in tests performed by George Fisher, Ltd.[2] The different distribution of precipitate phases suggests that the greater ferrite content is not the only reason for rapid embrittlement of Heat 280. The $M_{23}C_6$-like precipitates were also observed in Heat 278 after aging

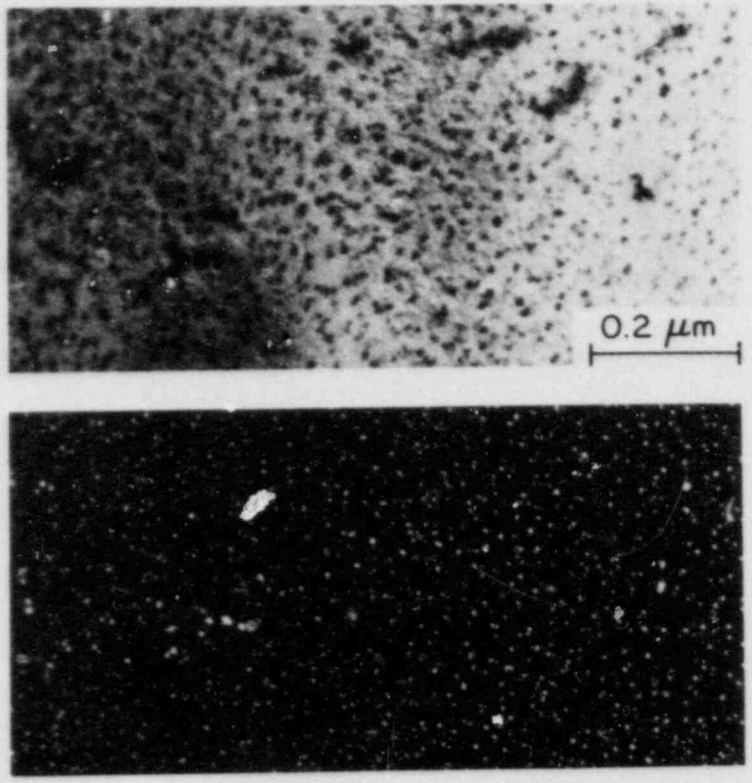

Fig. 4.4. Bright- and Dark-Field Images of Precipitates in the Ferrite Phase of CF-8 Stainless Steel (Heat 280) Aged for 66,650 h at 400°C.

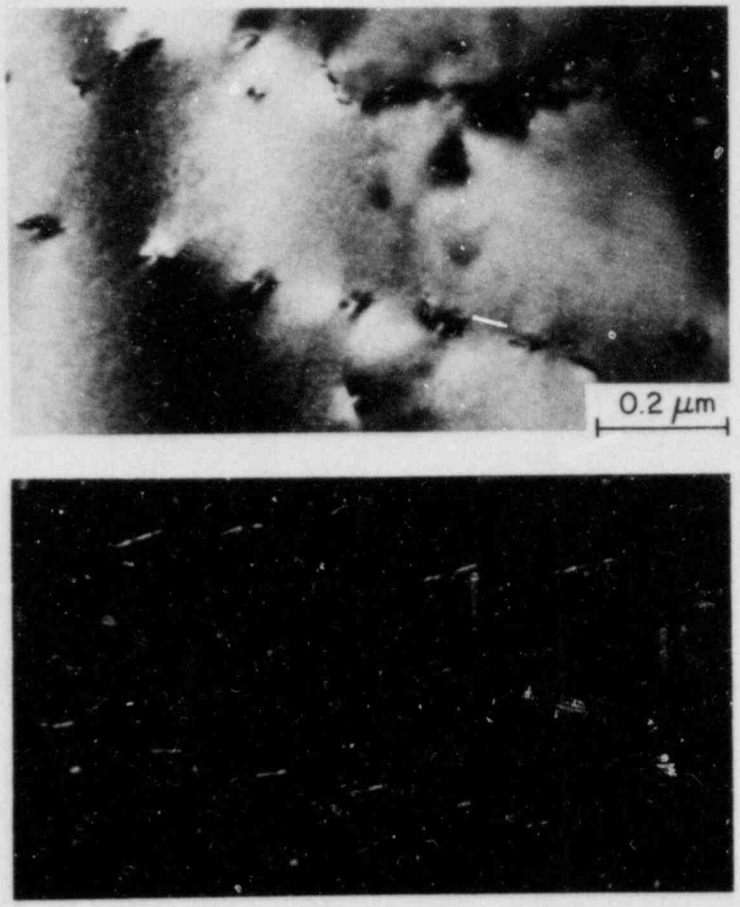

Fig. 4.5. Bright- and Dark-Field Images of Precipitates in CF-8 Stainless Steel (Heat 280) Aged for 10,000 h at 400°C.

for 70,000 h at 300°C, as shown in Fig. 4.6. This same heat treatment did not produce $M_{23}C_6$-like precipitates in Heat 280. These results indicate that small changes in alloy chemistry not only affect the ferrite content but also influence the precipitation behavior.

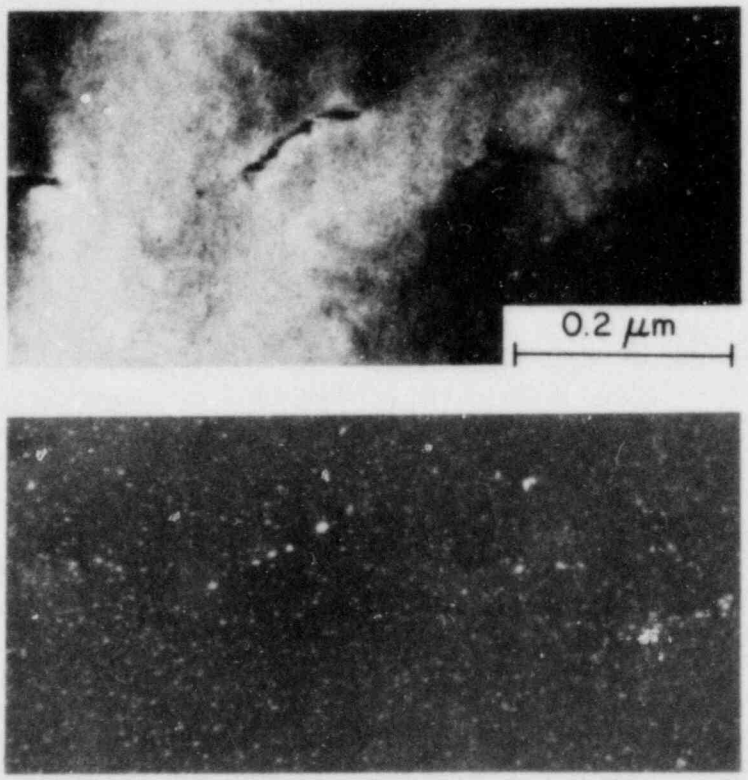

Fig. 4.6. Bright- and Dark-Field Images of Precipitates in CF-8 Stainless Steel (Heat 278) Aged for 70,000 h at 300°C.

C. References for Chapter IV

1. H. D. Solomon and T. M. Devine, "Influence of Microstructure on the Mechanical Properties and Localized Corrosion of a Duplex Stainless Steel," in Micon 78: Optimization of Processing, Properties, and Service Performance through Microstructural Control, ASTM STP 672, American Society for Testing and Materials, Philadelphia (1979), p. 430.

2. A. Trautwein and W. Gysel, "Influence of Long Time Aging of CF3 and CF8M Cast Steel at Temperatures Between 300 and 500°C on the Impact Toughness and the Structure Properties," in Stainless Steel Castings, ASTM STP 756, American Society for Testing and Materials, Philadelphia (1982), pp. 165-189.

3. G. Baudry and C. Pichard, "Evolution During Long Holding Times at 300 and 450°C of the Mechanical Properties of Austeno-Ferritic Steel Castings and Welded Joints Used in Pressurized Water Nuclear Reactors," Troisieme Congres National Sur La Technologie Des Appareils a Bression, Vol. 2, Materiaux, A.F.I.A.P. (1980), p. 673.

4. E. I. Landerman and W. H. Bamford, "Fracture Toughness and Fatigue Characteristics of Centrifugally Cast Type 316 Stainless Steel Pipe after Simulated Thermal Service Conditions, Ductility, and Toughness Considerations in Elevated Temperature Service," ASME MPC-8, American Society of Mechanical Engineers, New York (1978), p. 99.

5. G. Slama, P. Petrequin, and T. Mage, "Effect of Aging on Mechanical Properties of Austenitic Stainless Steel Castings and Welds," presented at SMIRT Post-Conference Seminar 6, Assuring Structural Integrity of Steel Reactor Pressure Boundary Components, Monterey, CA, Aug. 29 and 30, 1983.

6. T. J. Nichol, A. Datta, and G. Aggen, Embrittlement of Ferritic Stainless Steels, Metal. Trans. 11A, 573 (1980).

7. O. K. Chopra, G. Ayrault, and W. J. Shack, in Materials Science and Technology Division Light-Water-Reactor Safety Research Program: Quarterly Progress Report, January-March 1983, NUREG/CR-3689 Vol. I, ANL-83-85 Vol. I (April 1984), pp 136-152.

8. H. D. Solomon and L. M. Levinson, Mossbauer Effect Study of 475°C Embrittlement of Duplex and Ferritic Stainless Steels, Acta Metall. 26, 492 (1978).

9. M. J. Marcinkowski, R. M. Fisher, and A. Szirmae, Effect of 500°C Aging on the Deformation Behavior of an Iron-chromium Alloy, Trans. AIME 230, 676 (1964).

Distribution for NUREG/CR-3689 Vol. II (ANL-83-85 Vol. II)

Intern 1:

R. P. Anderson
R. Avery
G. Ayrault
E. S. Beckjord
M. Blander
F. A. Cafasso
O. K. Chopra
H. M. Chung
T. N. Claytor
L. W. Deitrich
C. E. Dickerman
D. R. Diercks
G. R. Fenske
F. Y. Fradin
B. R. T. Frost
E. E. Gruber
D. M. Gruen
G. L. Hofman
P. R. Huebotter
M. Ishii
W. D. Jackson
C. E. Johnson
T. F. Kassner (10)
K. L. Kliewer
J. M. Kramer
D. S. Kupperman
Y. Y. Liu
B. A. Loomis
P. A. Lottes
P. S. Maiya
V. A. Maroni
D. Moores
K. Natesan
L. A. Neimark
F. A. Nichols
P. R. Okamoto
F. S. Onesto
R. G. Palm
J. Y. Park
D. R. Pepalis
D. R. Perkins
R. B. Poeppel
J. J. Puro
K. J. Reimann
J. Rest (10)
G. S. Rosenberg
W. E. Ruther
W. J. Shack (3)
W. K. Soppet
E. M. Stefanski (2)
R. V. Strain
C. E. Till
H. C. Tsai
R. A. Valentin
A. Villalobos
R. W. Weeks
H. Wiedersich
F. L. Yaggee
R. S. Zeno
ANL Patent Dept.
ANL Contract File
ANL Libraries (3)
TIS Files (6)

External:

NRC, for distribution per R3 and R5 (450)
DOE-TIC (2)
Manager, Chicago Operations Office, DOE
R. Tom, DOE-CH
Materials Science and Technology Division Review Committee:
B. Alcock, U. Toronto
A. Arrott, Simon Fraser U.
R. C. Dynes, Bell Labs., Murray Hill
A. G. Evans, U. California, Berkeley
L. M. Falicov, U. California, Berkeley
H. K. Forsen, Bechtel Group, San Francisco
E. Kay, IBM San Jose Research Lab.
B. Maple, U. California, San Diego
C. L. McCabe, Cabot Corp., Kokomo, Ind.
P. G. Shewmon, Ohio State U.
J. K. Tien, Columbia U.
R. B. Adamson, General Electric Co., Vallecitos Nuclear Center, P. O. Box 460, Pleasanton, Calif. 94566
P. L. Andresen, General Electric Corporate Research and Development, Schenectady, N. Y. 12301
G. A. Arlotto, Office of Nuclear Regulatory Research, USNRC, Washington
D. Atteridge, Battelle Pacific Northwest Lab., P. O. Box 999, Richland, Wash. 99352
W. Berry, Battelle-Columbus Labs., 505 King Ave., Columbus, O. 43201
D. L. Burman, Westinghouse PWR Systems Div., P. O. Box 355, Pittsburgh, Pa. 15230
L. K. Chan, Office of Nuclear Regulatory Research, USNRC, Washington

C. Y. Cheng, Office of Nuclear Reactor Regulation, USNRC, Washington
R. A. Clark, Battelle Pacific Northwest Lab., P. O. Box 999, Richland, Wash. 99352
F. D. Coffman, Jr., Office of Nuclear Reactor Regulation, USNRC, Washington
W. J. Collins, Office of Inspection and Enforcement, USNRC, Washington
B. Cox, Chalk River Nuclear Labs., AECL, Chalk River, Ont., K0J 1J0, Canada
G. Cragnolino, Dept. of Metallurgical Engineering, Ohio State U., Columbus, O. 43210
D. Cubiciotti, Electric Power Research Inst., P. O. Box 10412, Palo Alto, Calif. 94304
J. C. Danko, Electric Power Research Inst., P. O. Box 10412, Palo Alto, Calif. 94304
B. J. Elliot, Office of Nuclear Reactor Regulation, USNRC, Washington
R. B. Foulds, Office of Nuclear Reactor Regulation, USNRC, Washington
M. Fox, Fox Enterprises, 7490 Stanford Place, Cupertino, Calif. 95014
Y. S. Garud, S. Levy, Inc., 1901 S. Bascom Ave., Campbell, Calif. 95008
S. M. Gehl, Electric Power Research Inst., P. O. Box 10412, Palo Alto, Calif. 94304
J. H. Gittus, Springfields Nuclear Power Development Labs., U. K. Atomic Energy Authority, Springfields, Salwick, Preston, PR4 ORR England
D. O. Harris, 750 Welch Rd., Palo Alto, Calif. 94304
W. S. Hazelton, Office of Nuclear Reactor Regulation, USNRC, Washington
R. R. Hobbins, EG&G/INEL, 1520 Sawtelle Dr., Idaho Falls, Idaho 83401
R. E. Johnson, Office of Nuclear Reactor Regulation, USNRC, Washington
W. V. Johnston, Office of Nuclear Reactor Regulation, USNRC, Washington
R. L. Jones, Electric Power Research Inst., P. O. Box 10412, Palo Alto, Calif. 94304
K. R. Jordan, Nuclear Fuel Div., Monroeville Nuclear Center, Westinghouse Electric Corp., Monroeville, Pa. 15146
J. N. Kass, General Electric Co., 175 Curtner Ave., San Jose, Calif. 95125
C. N. Kelber, Office of Nuclear Regulatory Research, USNRC, Washington
E. Kohn, Atomic Energy of Canada Ltd., Sheridan Park Research Community, Mississauga, Ont., Canada L5K 1B2
P. M. Lang, Office of Converter Reactor Deployment, USDOE, Washington, D. C. 20545
D. D. Lanning, Battelle Pacific Northwest Lab., P. O. Box 999, Richland, Wash. 99352
R. A. Lorenz, Oak Ridge National Lab., P. O. Box X, Oak Ridge, Tenn. 37830
P. MacDonald, EG&G/INEL, 1520 Sawtelle Dr., Idaho Falls, Idaho 83401
G. P. Marino, Office of Nuclear Regulatory Research, USNRC, Washington
C. E. McCracken, Office of Nuclear Reactor Regulation, USNRC, Washington
S. McDonald, Westinghouse Electric Corp. R&D Center, Beulah Rd., Pittsburgh, Pa. 15235
K. R. Merckx, Exxon Nuclear, Inc., 2955 George Washington Way, Richland, Wash. 99352
A. C. Millunzi, Office of Breeder Reactor Programs, USDOE, Washington, D. C. 20545
J. Muscara, Office of Nuclear Regulatory Research, USNRC, Washington
D. M. Norris, Electric Power Research Inst., P. O. Box 10412, Palo Alto, Calif. 94304
D. R. O'Boyle, Commonwealth Edison Co., P. O. Box 767, Chicago, Ill. 60690
R. N. Oehlberg, Electric Power Research Inst., P. O. Box 10412, Palo Alto, Calif. 94304

M. F. Osborne, Oak Ridge National Lab., P. O. Box X, Oak Ridge, Tenn. 37830
D. E. Owen, EG&G Idaho, P. O. Box 88, Middletown, Pa. 17057
T. P. Papazoglou, Lynchburg Research Center, Babcock & Wilcox Co., P. O. Box 1260, Lynchburg, Va. 24505
J. T. A. Roberts, Electric Power Research Inst., P. O. Box 10412, Palo Alto, Calif. 94304
E. J. Rowley, Commonwealth Edison Co., P. O. Box 767, Chicago, Ill. 60690
E. F. Rybicki, Dept. of Mechanical Engineering, Univ. of Tulsa, Tulsa, Okla. 74110
H. H. Scott, Office of Nuclear Regulatory Research, USNRC, Washington
C. Z. Serpan, Office of Nuclear Regulatory Research, USNRC, Washington
L. Shao, Office of Nuclear Regulatory Research, USNRC, Washington
R. D. Silver, Office of Nuclear Reactor Regulation, USNRC, Washington
P. Smerd, Combustion Engineering, Inc., P. O. Box 500, Windsor, Conn. 06095
A. A. Solomon, School of Nuclear Engineering, Purdue U., West Lafayette, Ind. 47907
D. M. Stevens, Lynchburg Research Center, Babcock & Wilcox Co., P. O. Box 239, Lynchburg, Va. 24505
J. Strosnider, Office of Nuclear Regulatory Research, USNRC, Washington
A. Taboada, Office of Nuclear Regulatory Research, USNRC, Washington
B. Turovlin, Office of Nuclear Regulatory Research, USNRC, Washington
R. Van Houten, Office of Nuclear Regulatory Research, USNRC, Washington
J. R. Weeks, Brookhaven National Lab., Upton, N. Y. 11973
K. R. Wichman, Office of Nuclear Reactor Regulation, USNRC, Washington

NRC FORM 335 (2-84) NRCM 1102, 3201, 3202

U.S. NUCLEAR REGULATORY COMMISSION

BIBLIOGRAPHIC DATA SHEET

SEE INSTRUCTIONS ON THE REVERSE

1. REPORT NUMBER (Assigned by TIDC, add Vol. No., if any)
NUREG/CR-3689 Vol. II
ANL-83-85 Vol. II

2. TITLE AND SUBTITLE
Materials Science and Technology Division Light-Water-Reactor Safety Research Program: Quarterly Progress Report, April—June 1983

3. LEAVE BLANK

4. DATE REPORT COMPLETED
MONTH | YEAR

5. AUTHOR(S)
W. J. Shack et al.

6. DATE REPORT ISSUED
MONTH: June | YEAR: 1984

7. PERFORMING ORGANIZATION NAME AND MAILING ADDRESS (Include Zip Code)
Argonne National Laboratory
9700 South Cass Avenue
Argonne, Illinois 60439

8. PROJECT/TASK/WORK UNIT NUMBER

9. FIN OR GRANT NUMBER
A2015, A2017, A2212, A2243

10. SPONSORING ORGANIZATION NAME AND MAILING ADDRESS (Include Zip Code)
Division of Engineering Technology
Office of Nuclear Regulatory Research
U. S. Nuclear Regulatory Commission
Washington, D. C. 20555

11a. TYPE OF REPORT
Technical; quarterly

b. PERIOD COVERED (Inclusive dates)
April—June 1983

12. SUPPLEMENTARY NOTES

13. ABSTRACT (200 words or less)

This progress report summarizes the Argonne National Laboratory work performed during April, May, and June 1983 on water reactor safety problems. The research and development areas covered are Environmentally Assisted Cracking in Light Water Reactors, Transient Fuel Response and Fission Product Release, Clad Properties for Code Verification, and Long-Term Embrittlement of Cast Duplex Stainless Steels in LWR Systems.

14. DOCUMENT ANALYSIS — a. KEYWORDS/DESCRIPTORS

embrittlement cast stainless steel
fission product modeling
fracture irradiated Zircaloy
nondestructive evaluation
pipe cracking
water chemistry

b. IDENTIFIERS/OPEN ENDED TERMS

15. AVAILABILITY STATEMENT
unlimited

16. SECURITY CLASSIFICATION
(This page) unclassified
(This report) unclassified

17. NUMBER OF PAGES

18. PRICE